

ABSTRACT

Title of Document:

CHARACTERIZATION OF FIRE INDUCED
FLOW TRANSPORT ALONG CEILINGS
USING SALT-WATER MODELING

Xiaobo Yao, Doctor of Philosophy, 2006

Directed By:

Assistant Professor André W. Marshall,
Department of Fire Protection Engineering

This research provides a detailed analysis of turbulent mixing and heat transfer in canonical fire plume configurations by using a quantitative salt-water modeling technique. The methodology of quantitative salt-water modeling builds on the analogy between salt-water flow and fire induced flow, which has been successfully used in the qualitative analysis of fires. Non-intrusive laser diagnostics, Planar Laser Induced Fluorescence (PLIF) and Laser Doppler Velocimetry (LDV), have been implemented to measure the dimensionless density difference and velocity in salt-water plumes. In the implementation of the PLIF technique, the salt-water concentration is measured through tracking a fluorescent dye tracer within the entire spatial domain of a planar section of the salt-water flow, which is diluted at the same rate as the salt water. The quantitative salt-water modeling technique has been validated by comparing it with real fire experiments and theoretical data. The scaling laws are also proved by varying the initial source strength or ceiling height in the impinging plume configuration. The detailed salt-water measurements provide

insight into of the wall interactions and laminarization effects in the impinging plume configuration. Additionally, highly resolved measurements provide mean profiles and turbulent statistics which will be useful for validating and developing sub-grid scale models in Computational Fluid Dynamics (CFD) codes. Furthermore, an engineering heat transfer model is developed to predict the convective ceiling heat transfer from impinging plumes using the quantitative salt-water modeling technique along with an adiabatic wall modeling concept. The successful application of the adiabatic wall heat transfer model illustrates a well controlled method for studying the heat transfer issues in more complex fire induced flow configurations by using the quantitative salt-water modeling technique.

CHARACTERIZATION OF FIRE INDUCED FLOW TRANSPORT ALONG
CEILINGS USING SALT-WATER MODELING

By

Xiaobo Yao

Dissertation submitted to the Faculty of the Graduate School of the
University of Maryland, College Park, in partial fulfillment
of the requirements for the degree of
Doctor of Philosophy
2006

Advisory Committee:

Assistant Professor André W. Marshall, Chair
Professor Deborah J. Goodings
Professor James G. Quintiere
Associate Professor Kenneth Kiger
Associate Professor Arnaud Trouvé
Assistant Professor Peter B. Sunderland

© Copyright by
Xiaobo Yao
2006

Acknowledgements

I first would like to thank Combustion Science and Engineering, Inc. in Columbia Maryland and National Fire Protection Associates (NFPA) for providing funding for this study. I would like to thank Dr. Andre W. Marshall for affording me this research opportunity. His motivation and advice allowed me to acquire a vast array of knowledge and improve the quality of this research. I would like to thank Dr. Rodney A. Bryant for providing the Laser Doppler Velocimetry system for this research. I also offer my sincere gratitude to Dr. Arnaud Trouvé and Mr. Tingguang Ma for their professional and personal guidance from the inception through the completion of this project. I would like to thank Mr. Sean P. Jankiewicz for his help on the implementation of this quantitative technique, too. Special thanks are due to the Fire Transport Research Group and all of the students from the Fire Engineering and Thermal Sciences Laboratory. They have provided me with a friendly and supportive working environment, as well as constructive feedback and suggestions.

I would like to extend a note of gratitude to the rest of my advisory committee, Dr. Deborah J. Goodings, Dr. James G. Quintiere, Dr. Kenneth Kiger and Dr. Peter B. Sunderland, The support from each member of my committee has truly been appreciated. Last but not least, I would like to thank my wife Juan Zhang for her unwaivering encouragement, support, and patience throughout this project.

Table of Contents

Acknowledgements.....	ii
Table of Contents.....	iii
List of Tables.....	v
List of Figures.....	vi
Chapter 1: Introduction.....	1
1.1 Motivation.....	1
1.2 Literature Review.....	3
1.2.1 Fire Plume and Ceiling Jet.....	5
1.2.2 Salt-Water Modeling.....	10
1.3 Research Objectives.....	12
Chapter 2: Approach.....	15
2.1 Fire/Salt-Water Modeling Analogy.....	15
2.1.1 Dimensionless Analysis.....	16
2.1.2 Dimensionless Parameter Strategy.....	19
2.2 Experimental Facility.....	20
2.2.1 Experiment Setup.....	21
2.2.2 Planar Laser Induced Fluorescence (PLIF) System.....	24
2.2.3 Laser Doppler Velocimetry (LDV) System.....	30
2.3 Experimental Methodology.....	33
2.3.1 Initial Conditions of Salt-Water Experiments.....	34
2.3.2 PLIF Salt-Water Measurements.....	37
2.3.3 LDV Salt-Water Measurements.....	44
2.4 Error Estimation.....	47
2.4.1 Index of Refraction Effects.....	47
2.4.2 Uncertainty of Salt Mass Fraction Measurements.....	51
2.4.3 Uncertainty of Velocity Measurement.....	55
Chapter 3: Results and Analysis.....	58
3.1 Validation of the Quantitative Salt-water Modeling Technique.....	58
3.1.1 PLIF Salt-Water Modeling Validation.....	60
3.1.2 LDV Salt-Water Modeling Validation.....	62
3.2 Impinging Plume Dynamics.....	65
3.2.1 Characterization of the Plume Region.....	66
3.2.2 Characterization of the Turning Region.....	73
3.2.3 Characterization of the Ceiling Jet Region.....	79
3.3 Turbulent Mixing Dynamics.....	89

Chapter 4: Adiabatic Wall Heat Transfer Model.....	94
4.1 Introduction.....	94
4.2 Effectiveness η	98
4.3 Convective Heat Transfer Coefficient h	100
4.3.1 Velocity Similarity Function in the Ceiling Jet.....	101
4.3.2 Friction Coefficient C_f	105
4.3.3 Convective Heat Transfer Coefficient, h	107
4.4 Adiabatic Wall Heat Transfer Model.....	110
Chapter 5: Conclusions.....	117
Appendix A: Source Based Dimensionless Analysis.....	121
Appendix B: Laser Sheet Intensity Correction.....	130
Appendix C: LES Mixing Model.....	132

List of Tables

Table 2.1 Initial momentum flux and source specific buoyancy flux.....	35
------------------------------------------------------------------------	----

List of Figures

Figure 1.1: Schematic of plume and ceiling jet flow for an unconfined ceiling.....	4
Figure 2.1: Quantitative salt-water modeling technique.....	15
Figure 2.2: Quantitative salt-water modeling facility with PLIF/LDV diagnostics ..	21
Figure 2.3: Optical schematic of backscattering LDV Probe	31
Figure 2.4: Comparison of plume width, b_{pl} , and the acceptable incident light path length, b_{ab} , $(C_{dye})_{inj} = 0.2 \text{ mg/l}$	39
Figure 2.5: Recommended initial injected dye concentration	41
Figure 2.6: Interface effects on the beam crossing position	49
Figure 2.7: Uncertainty of laser sheet	51
Figure 3.1 Visualization of the dimensionless density difference θ of an unconfined salt-water plume for Case 1	59
Figure 3.2 Dimensionless density difference distribution along plume centerline....	61
Figure 3.3 Dimensionless velocity distribution along plume centerline.....	64
Figure 3.4: The centerline dimensionless mean characteristic and related fluctuation of the unconfined salt-water plume Case 1	68
Figure 3.5: Visualization of the dimensionless density difference of an unconfined salt-water plume in far field.....	70
Figure 3.6: Probability Density Function $p_i(\theta^*)$ at axial positions.....	72
Figure 3.7: Centerline mean density difference of impinging plume, $\bar{\theta}_c$	74
Figure 3.8: Quantitative visualization of the dimensionless density difference in salt-water flow, θ^* for Case 4	76
Figure 3.9: Probability Density Function $p_i(\theta^*)$ at turning region for Case 4.....	78
Figure 3.10: Schematic of the ceiling jet and its characteristic parameters.....	80
Figure 3.11: Turbulent structures and ceiling jet progression for Case 4.....	81

Figure 3.12: Probability Density Function $p_i(\theta^*)$ at $(x_1/H = 0.3)$ in the ceiling jet region for Case 4.....	83
Figure 3.13: Peak values of source independent characteristics along the ceiling	85
Figure 3.14: Ceiling jet characteristics along the ceiling.....	86
Figure 3.15: Mean profiles of dimensionless density difference and velocity at various locations along the ceiling jet	88
Figure 3.16: The instantaneous mixture fraction Z for Case 1	92
Figure 3.17: Temporal Pdfs for Case 1	93
Figure 4.1: Temperature characteristics in impinging plume flow configuration	95
Figure 4.2: Adiabatic wall heat transfer model.....	97
Figure 4.3: Distribution of effectiveness η along ceiling	99
Figure 4.4: Velocity similarity profile in the ceiling jet layer	102
Figure 4.5: Scaling laws of distribution of source independent velocity and maximum velocity position.....	103
Figure 4.6: Similarity function of $f(\chi)$ in boundary layer	104
Figure 4.7: Heat transfer coefficient along ceiling	107
Figure 4.8: Heat transfer rate along ceiling radial position between model prediction and You's experiments	112
Figure 4.9: Heat transfer rate along ceiling radial position between model prediction and Veldman's Test 1, $Q = 1.17$ kW, $H_c = 0.813$ m.....	113
Figure 4.10: Comparison of different transfer model with You's experiment.....	115

Nomenclature

a_i	constant coefficient
b	plume width where $U/U_{max} = 1/e$
b_{pl}	plume width where $\theta/\theta_{max} = 0.01$
b_{ab}	acceptable incident light path length where $I_e = 0.95I_0$
Y_{salt}	salt mass fraction
ρ_0	ambient fluid density
z_0	virtual origin
H_0	ceiling height above fire source
H	ceiling height from virtual origin, where $H^+ = H - z_0$
T_0	ambient fluid temperature
ΔT	temperature difference, where $\Delta T = T - T_0$
ΔT_{max}	maximum temperature difference, where $\Delta T_{max} = T_{max} - T_0$
\dot{Q}	heat release rate, $\dot{Q} = \dot{Q}_c$ without special indication in this study
\dot{Q}_c	convective heat release rate
\dot{m}_{salt}	salt release rate
D^*	characterized length scale, $D^* = \left(\frac{\beta_{sw} \dot{m}}{\rho_0 g^{1/2}} \right)^{2/5}$
u_i	plume mean velocity
u_i'	fluctuation of plume velocity
U	characteristics velocity, $U = (gH)^{1/2} (Q^*)^{1/3}$
l_U	ceiling layer velocity thickness

l_T	ceiling layer thermal thickness
L_M	Morton Length scale (m), $L_M = M^{3/4} / B^{1/2}$
u_i^*	dimensionless velocity, $= u_i (gH)^{-1/2} (Q^*)^{-1/3}$ or $= u_i (gH)^{-1/2} (m_{sw}^*)^{-1/3}$
\dot{q}'''	volumetric energy release rate
\dot{q}^*	dimensionless volumetric energy release rate, $\dot{q}^* = \dot{q}''' H^3 / \dot{Q}$
\dot{w}'''	volumetric salt mass release rate
\dot{w}^*	dimensionless volumetric salt mass release rate, $\dot{w}^* = \dot{w}''' H^3 / \dot{m}_{salt}$
Q^*	dimensionless source strength for fire, $Q^* = \beta_T \dot{Q} / \rho_0 c_p g^{1/2} x_3^{5/2}$
m_{sw}^*	dimensionless source strength for salt water, $m_{sw}^* = \beta_{sw} \dot{m}_{salt} / \rho_0 g^{1/2} x_3^{5/2}$
I_e	intensity of the excited beam
I_0	incident light intensity
C_{dye}	mass concentration of dye
C_{salt}	mass concentration of salt
B	buoyancy flux, $M = 2\pi \int_0^{D/2} U^2 r dr$
M	momentum flux, $B = 2\pi \int_0^{D/2} U g \frac{\rho_{source} - \rho_0}{\rho_{source}} r dr$
Re	Reynolds number
Re_H	characteristic Reynolds number, $Re_H = UH / \nu$
Ri	Richardson number, $= g\Delta\rho\delta_U / \rho_0 U^2$
Pr	Prandtl number
Sc	Schimidt number

Gr Grashof number, = $g\beta_T \dot{Q}H^2 / \rho_0 c_p v^3$ for fire; = $g\beta_{sw} \dot{m}_{salt} H^2 / \rho_0 c_p v^3$ for salt water

Greek

δ ceiling jet maximum characteristic position

α entrainment constant

ε extinction coefficient

β volumetric expansion coefficient, = $1/T_0$ for fire; = 0.76 for salt water

θ dimensionless density difference, = $\beta_T (T - T_0)$ for fire; = $\beta_{sw} Y_{salt}$ for salt water

Subscript

c centerline

sw salt water

T fire

inj injector position

Chapter 1: Introduction

Fire protection engineers have been working decades to avoid life losses and reduce property damages in various fire scenarios. Most fire scenarios occur in enclosures, such as apartments, hotels, warehouses, and storage rooms. Plumes formed from these fires impinge on ceilings creating ceiling jets beneath ceilings within enclosures. The interaction of the fire plume with the ceiling plays a major role in critical physical processes of engineering relevance including smoke dispersion, important in toxicity and detection, and heat loading, important in fire-structure interaction and flame spread.

1.1 Motivation

Plume and ceiling jet flow studies are important for improving fire detection system designs and practices, including the designs of activation devices for sprinklers and various types of smoke and fire detectors. The characteristics of the impinging plumes, such as heat transfer, velocity, and smoke concentrations near the ceiling are also of fundamental interest to fire protection researchers for predicting fire behavior. Due to the limitation in available diagnostics and the intractable fire environment, previous researchers have been unable to fully explore turbulent transport near the ceiling. Beyler [1] has provided comparisons between various correlations of buoyant plumes, and ceiling jet parameters in his overview paper. The poor agreement in the empirical correlations of maximum ceiling temperatures and heat transfer rate indicated the need for further study of the ceiling jet characteristics.

Alternatively, fundamental turbulent and heat transfer models based on flow details have been implemented into CFD models. These models are largely un-validated for fire induced flows. Careful measurements are required for validating and developing appropriate CFD wall models near the ceiling in order to simulate the turbulent impinging plume behaviors.

Fire protection engineers and designers often rely on model studies to predict the fire behavior of a physical system of interest due to the hazardous conditions and inherently destructive nature of fire. There are two objectives in developing a model for fire applications. First, it can provide insight to the fundamental physical processes of governing fire dynamics. Second, it can provide an alternative to carry out a large number of expensive full scale tests to discover the effect of various parameters. Analytical fire modeling includes examples ranging from simple zone models to complex Computational Fluid Dynamics (CFD) codes like NIST's Fire Dynamics Simulator (FDS). Also, scaled down reacting experiments of small fires or certain large fires are often studied. These tools can be applied to predict the evolution of temperature and smoke conditions in an enclosure at a fraction of the cost and time associated with full scale fire testing.

Salt-water modeling is an excellent physical model to study fire induced flows. In this technique, salt water is carefully introduced into a fresh-water environment as a means to create the buoyant characteristics associated with flows induced by a fire plume. Salt-water modeling physically reproduces the dispersion dynamics related to a fire while allowing experiments to be conducted with little cost and at a readily accessible laboratory scale. Salt-water modeling has been

successfully used to visualize the smoke dispersion structures in various flow configurations using a tracer dye. With laser diagnostics, the qualitative salt-water modeling technique can be refined to provide more detailed and valuable quantitative information of the plume mixing dynamics.

1.2 Literature Review

The unconfined fire plume and the impinging fire plume are two classical flow configurations in fire scenarios. The transport in these fire scenarios is governed by buoyancy. These flows can be modeled by creating buoyant forces using a variety of sources. For instance, a heat source could be used (like in a smoke stack plume) or one fluid could be introduced into another fluid of different density (as in salt water outfall). Once the fluid is set into motion, the velocity field and the thermal field are strongly coupled for typical source strengths of interest. The initial state of laminar motion typically transitions quickly to turbulence and the flow starts to spread radially by entraining ambient fluid into the main flow. The laboratory plume is an idealization of large scale fire induced flows and it allows us to study basic behavior in turbulent buoyant flows. It can be shown that regardless of the kind of source, all plumes are dynamically similar in the buoyancy dominant region as long as the density differences between the flow and the ambient surroundings are small compared to some reference density in the flow [2].

A fire plume is loosely described as vertical rising column of gases resulting from a flame. The term plume is generally used to describe the non-combusting region – which might dominate the flow away from the combustion source especially

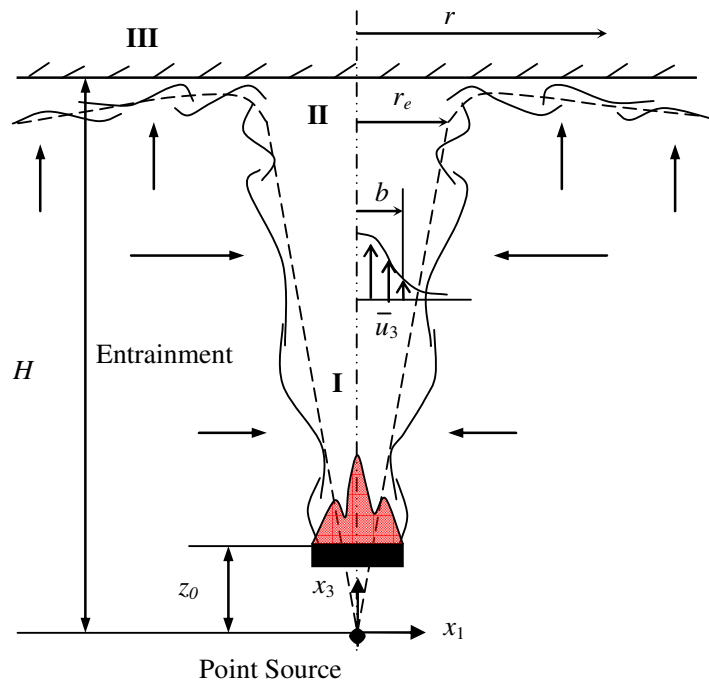


Figure 1.1: Schematic of plume and ceiling jet flow for an unconfined ceiling
 I: Plume Region; II: Turning Region; III: Ceiling Jet Region

for small fires, for example, a small, floor-level fire in a compartment generating a buoyant plume of hot gas which flows upward to the ceiling. Impingement of the fire plume on the ceiling results in a radially expanding flow of a thin layer of gas just below the ceiling. This near ceiling flow, as shown in Fig. 1.1, determines heat transport to the ceiling and heat and mass transport to detection devices near the ceiling. According to the flow characteristics, the impinging plume configuration can be divided into three regions: plume region, turning region and ceiling jet region. Unless the fire source is extremely weak, the buoyant fire-plume is turbulent for most of the floor to ceiling distance. The ceiling jet generated by the turbulent plume is also turbulent, although far from the plume centerline, turbulence may be suppressed by the gravitational stability of the hot gas near the ceiling.

Turbulent ceiling jets with a density differing from that of ambient fluid have not been studied extensively. However, once the flow originating from the plume turns and forms a ceiling layer, it can be considered a wall jet. Wall jet theory has provided the basis for describing the ceiling layer resulting from the impinging plume. Salt-water modeling provides an easy way to simulate the complicated turbulent behavior in real fire scenarios based on the hydraulic analog. It has been successfully used in previous fire studies [3-7]. Laser diagnostic techniques, such as Planar Laser Induced Fluorescence (PLIF) and Laser Doppler Velocimetry (LDV), are applied in the salt-water modeling study to achieve quantitative measurements. Previous investigator's work will be presented in this section.

1.2.1 Fire Plume and Ceiling Jet

The unconfined point-source plume configuration has been used by previous researchers to establish plume theory. This theory provides solutions for the temperature profile, velocity profile and entrainment for thermal plumes at various elevations above the source [8]. Based on point source theory, the behavior of the fire plume is independent of the details of the heat source including the fuel source and source geometry. The turbulent flow above a point source of heat is analyzed in terms of the total mass, momentum and energy integrated across the plume cross section assuming that the entrainment velocity is proportional to the centerline plume velocity. Assuming the average temperature and velocity across the plume have Gaussian profiles, Zukoski et al. [9] provided a theoretical solution for the plume

momentum and energy equations by using an integral method. The solutions based on a Gaussian profile assumption are

$$\frac{\bar{\theta}}{\theta_c} = \exp\left(-\frac{\beta^2 x_1^2}{b^2}\right), \quad (1.1)$$

$$\frac{\bar{u}_3}{(\bar{u}_3)_c} = \exp\left(-\frac{x_1^2}{b^2}\right), \quad (1.2)$$

$$\frac{b}{x_3^+} = \frac{6}{5}\alpha, \quad (1.3)$$

$$\bar{\theta}_c = C_T Q^{*2/3}, \quad (1.4)$$

$$\frac{(\bar{u}_3)_c}{\sqrt{g x_3^+}} = C_V Q^{*1/3}, \quad (1.5)$$

where

$$C_T = (5/6)[5/(9\pi^2)]^{1/3} \beta^{1/2} (1+\beta)^{2/3} \alpha^{-4/3},$$

$$C_V = [25/(24\pi)]^{1/3} (\beta^{-1} + 1)^{1/3} \alpha^{-2/3},$$

$x_3^+ = x_3 - z_0$ is the elevation above the point source of buoyancy, z_0 is the virtual origin; b is the radius position where $\bar{u}_3 / (\bar{u}_3)_c = 1/e$, Q^* is the dimensionless source $Q^* = \beta_T \dot{Q} / (\rho_o c_p g^{1/2} (x_3^+)^{5/2})$, $\beta_T = 1/T_0$, C_T and C_V are constants related to the entrainment constant, α , and the ratio of the velocity half-width to the temperature half-width, β .

This theoretical solution has been validated by many experiments [10-13]. However, the constant of proportionality determined from these experiments vary widely having, $0.085 \leq 6\alpha/5 \leq 0.124$ and $0.86 \leq \beta \leq 1.4$. The discrepancies of the constants can be attributed to the difficulty of positioning the measuring probes

accurately with respect to the centerline, and to different intrinsic errors associated with the anemometers used. In these studies, salt-water modeling measurements were compared to following correlations recommended by Zukoski [14] with $\alpha = 0.11$ and $\beta = 0.956$,

$$\frac{b}{x_3^+} = 0.131 \quad (1.6)$$

$$\bar{\theta}_c = 9.115Q^{*2/3} \quad (1.7)$$

$$\frac{(\bar{u}_3)_c}{\sqrt{gx_3^+}} = 3.87Q^{*1/3} \quad (1.8)$$

Once the plume impinges on a ceiling, it turns to form a radially expanding ceiling jet. The flow behavior becomes more complicated compared with the fire plume. Due to the viscous interactions with ceiling, there is a competition between turbulent mixing and stable stratification along the ceiling. A number of theoretical and experimental fire studies have been performed in the impinging plume configuration. Most notably, Alpert [12] performed an analytical and experimental study developing the theory and associated scaling laws for fire induced ceiling jets. His analysis successfully predicted the maximum temperature distributions in the ceiling jets and is widely used in hazard analysis. Based on his analysis, he provided relationships for dimensionless ceiling layer thickness, velocity, and temperature, which compares favorably with measurements. In fact, his analysis revealed that these flow quantities are relatively insensitive to geometric scale. Alpert suggested that credible small-scale fire experiments could be conducted at ceiling heights down to 0.6 m.

Motevalli and Marks [15] conducted small-scale experiments of ceiling jet heat transfer, which generally compared favorably with other ceiling jet data and analysis for $x_1/H < 2$. The velocity and temperature measurements were obtained for unconfined ceiling jets under ceiling transient and steady-state conditions. Small fires of 0.5 kW to 2.0 kW were produced with a premixed methane-air burner. These measurements represented one of the most detailed studies of unconfined ceiling jets and were in general agreement with large scale data. Noticeable discrepancies were encountered when comparing measured momentum and thermal thickness between investigations. These discrepancies were attributed to coarse measurements and simplifying assumptions by other investigators concerning the equivalency of the momentum and thermal thicknesses in other analysis. However, no convective heat transfer rate to the ceiling was studied in his investigation.

Convective heat transfer from the ceiling jet layer to the ceiling surface has been studied by Veldman et al. [16]. They conducted experiments to investigate the axisymmetric heat transfer from small scale fires (1.17 kW and 1.53 kW) under the impinging plume condition. An empirical correlation involving the source strength, Q , and ceiling height, H , was found to correlate measurements of the adiabatic wall temperature and its radial variation in the range from $0 \leq x_1/H \leq 0.7$. A similar correlation for estimating the ceiling heat transfer coefficient was confirmed by the experimental results. However, their study was limited by the absence of any velocity measurements in both plume and ceiling jet configurations. You and Faeth [17] also conducted a study on heat transfer from an impinging fire plume to a horizontal ceiling. Their measurements were compared with predictions of both

differential and integral models where $x_1/H < 1.7$. The integral model provided a reasonable prediction of flow properties and ceiling heat fluxes. Their results also indicated the estimation of flow characteristics was greatly influenced by entrainment. Ceiling friction only had a secondary effect on the flow structure predictions.

Cooper [18-20] developed a heat transfer analysis by using an adiabatic ceiling surface temperature, T_{ad} , as the reference temperature in Newton's law of cooling. The adiabatic surface temperature, T_{ad} , depends on the fire configuration, but is independent of the ceiling surface temperature. This adiabatic surface temperature describes the gas temperature decay along the ceiling due to entrainment. Cooper provided correlations for T_{ad} distributions along the ceiling by analyzing previous researcher's experimental data [16, 21]. Correlations of the heat transfer coefficient, h , in the turning region and the ceiling jet region of the plume are also provided. Convective heat transfer from the ceiling jet to the ceiling surface has been estimated using correlations of T_{ad} and h in the range of $0 \leq x_1/H \leq 2.2$. Goldstein et al. [22], also investigated the convective heat transfer of a heated circular air jet impinging on a flat surface using T_{ad} as a reference temperature. The concept of effectiveness has been adopted to express the adiabatic surface temperature in dimensionless form. The heat transfer coefficient was also found to be independent of the relative magnitude of the jet temperature and the ambient temperature, if the adiabatic wall temperature is used as a reference temperature in the definition of the heat transfer coefficient. In the current research, the concept of effectiveness is

applied with modification to the analysis of the convective heat transfer rate from the ceiling jet to the ceiling.

These experimental and mathematical modelling studies have provided the necessary understanding to predict some of the general transport behavior in fires based on empirical correlations. The results of these investigations have advanced the understanding of fire phenomena and improved the design of fire protection systems. However, detailed measurements in well controlled experiments are required for model development. In particular, characterizations of the velocity field in fire plume configurations are notably absent.

1.2.2 Salt-Water Modeling

Salt-water modeling has been successfully used in past as a qualitative tool to explore smoke dispersion in complex geometries. In salt-water modeling, a full-scale fire induced flow is simulated by creating turbulent buoyancy driven flow in a small-scale geometrically similar configuration. Sangaras and Faeth [23] used salt-water modeling for a fundamental investigation. They analyzed the temporal development of round turbulent non-buoyant starting jets and buoyant starting plumes theoretically and experimentally by observing the motion of the dye tracer. The flow properties were measured as a function of time for various source diameters in a wide range of Re number based on the source diameter from 1,450 – 11,700 and jet/ambient density ratio from 1.00 to 1.12. The saline solution was premixed with a dye tracer in order to provide good flow visualization. The visualization for the dispersion dynamics and front movement within transparent enclosures were recorded by a CCD camera. This

method may be appropriate for estimating front arrival times; however, the concentration within the flow field could not be measured.

Steckler et al. [4] visualized the smoke dispersions in a scale multi-compartment warship using a salt-water plume with dye tracer. They established the fire/salt-water analogy through quantitative scale analysis and salt-water flow visualization experiments. In their study, they demonstrated that with appropriate scaling the governing equations for dimensionless temperature and dimensionless salt-water concentration have identical form with the exception of Re , Sc , and Pr discrepancies encountered in the diffusive term coefficients. They asserted that for sufficiently turbulent salt-water and fire induced flows, diffusive discrepancies could be neglected owing to the small value of the diffusive term coefficients, thus establishing the analogy. However, it should be noted that very near the wall the diffusive terms and the corresponding discrepancies may not be negligible.

Kelly [5] using similar dye visualization techniques, a salinity probe, and scaling arguments, found semi-quantitative agreement when comparing dimensionless event times between salt-water experiments and computational fluid dynamics (CFD) analysis of fires in geometrically similar multi-room compartments. Clement and Fleischman [6] also compared salt-water experiments in a two-room enclosure with CFD analysis using the Fire Dynamics Simulator (FDS). Their salt-water experiments were conducted using Planar Laser Induced Fluorescence (PLIF) to obtain detailed salt concentration data. The PLIF technique allows measurement of the salt-water concentration through tracking a fluorescent dye tracer, which is diluted at the same rate as the salt water [24]. The salt-water concentration was used to

determine the density field, which compared favorably with FDS predictions of density distributions in the plume and in the far field adjacent to the source room.

More recently, Jankiewicz [3] combined salt-water modeling and PLIF to explore the applicability of these techniques to the prediction of detector response times. He found excellent agreement between dimensionless front arrival times in the salt-water model and the full-scale fire experiments. He also found some limited agreement between the dimensionless temperatures measured in the fire tests and dimensionless concentrations measured in the salt-water models. More impressive quantitative agreement between PLIF salt-water measurements and fire plume measurements have been demonstrated by Yao et al. [7, 25, 26] in the unconfined plume and impinging plume configurations. Yao et al. compared his scaled salt-water measurements with McCaffrey's fire plume centerline temperature measurements and point source plume theory [13]. The favorable agreement between PLIF salt-water measurements, fire plume measurements, and point source plume theory established the applicability of the PLIF salt-water measurement and scaling techniques to unconfined fire plumes. Yao et al. also obtained highly resolved measurements for sub-grid scale CFD model validation in that study. The impinging plume and resulting ceiling jet were also critically examined. Salt-water measurements in this flow configuration were compared with fire measurements and ceiling jet theory.

1.3 Research Objectives

The purpose of this research is to develop an experimental technique and an analytical framework for characterizing fire induced flows using salt-water modeling.

A quantitative technique has been established to evaluate turbulent characteristics of the fire induced flows by using salt-water modeling and advanced laser diagnostics in scaled model configurations. The salt-water modeling technique provides flow details which are not easily obtained in real fires. Generally, the harsh fire environment makes it difficult to acquire detailed flow measurements.

The salt-water modeling technique is applied to two canonical fire induced flow configurations, the unconfined plume and the unconfined impinging plume, to characterize turbulent transport dynamics. The salt-water quantitative measurements are compared with theoretical analysis and full scale fire experiments. Velocity and scalar transport in this configuration are measured by advanced laser diagnostic techniques, namely Laser Doppler Velocimetry (LDV) and Planar Laser Induced Fluorescence (PLIF). The salt-water modeling measurements are also able to provide flow details near the ceiling for validating and developing CFD wall models.

Another objective for this study is to develop an engineering heat transfer model for the impinging plume. This heat transfer model was developed using salt-water measurements and scaling laws, committed with Newton's law of cooling and the adiabatic wall temperature concept. This model can predict the distribution of the convective ceiling heat flux simply from the fire size and ceiling height. Furthermore, development of a technique which uses salt-water modeling along with the adiabatic wall concept may allow for engineering heat transfer model development in geometries far more complex than the impinging plume.

The specific objectives of this research are to:

- Develop a quantitative technique and an analytical methodology for evaluating fire induced flow using salt-water modeling.
- Characterize the turbulent transport in canonical fire plume configurations for insight into the transport dynamics of fire induced flows.
- Provide high fidelity flow measurements with salt-water experiments for the development and validation of CFD models used in fire induced flows.
- Develop and refine an engineering model for ceiling jet heat transfer based on the adiabatic wall temperature concept.

Chapter 2: Approach

The quantitative salt-water modeling technique can be viewed as a tool to characterize different aspects of fire induced flow, e.g. dispersion, turbulent mixing and heat transfer. Figure 2.1 shows a schematic of various elements of the quantitative salt-water modeling. The quantitative salt-water modeling technique requires buoyant scale analysis, advanced laser diagnostics and buoyancy driven flow experiments. The fundamental scaling theory and the fire/salt-water modeling analogy are introduced in this chapter. A more detailed discussion of the physical and analytical requirements for implementation of this quantitative technique is also included.

2.1 Fire/Salt-Water Modeling Analogy

The fire/salt-water modeling analogy is established on the similarity of dimensionless governing equations between fire induced flow and salt-water flow. Quintiere [27] examined the principle for scaling fire phenomena using dimensionless groups derived from the governing differential equations. Various strategies for

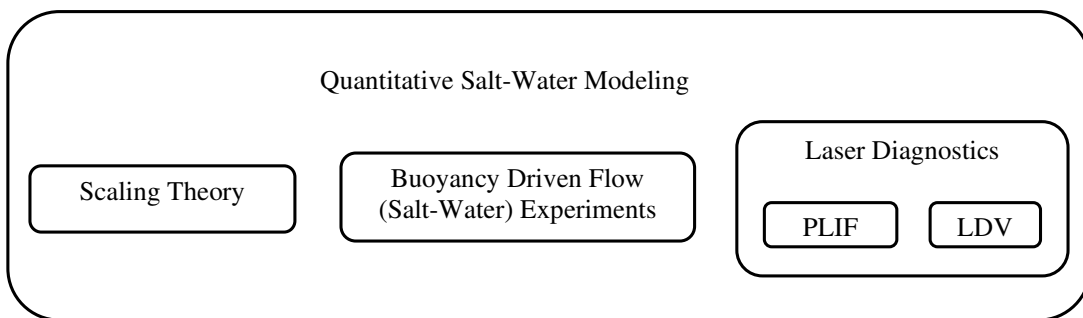


Figure 2.1: Quantitative salt-water modeling technique

scaling in fire were also discussed. The same method has been introduced in this study to establish the analog modeling between salt-water flow and fire induced flow, where salt water is injected into the fresh water system to simulate a buoyant heat source analogous to a fire. In this study, momentum and mass species equations of the water system correspond to the momentum and energy (and species) equations of the fire system.

2.1.1 Dimensionless Analysis

With appropriate dimensionless parameters, the dimensionless governing equations of fire induced flow and salt-water flow are expressed as follows (detailed scale analysis can be found in Appendix A).

Governing equations in fire induced flow:

Momentum:

$$\frac{\partial u_j^*}{\partial t^*} + u_i^* \frac{\partial u_j^*}{\partial x_i^*} = -\frac{\partial p^*}{\partial x_i^*} + \frac{1}{(Gr_{source}^{fire})^{1/3}} \frac{\partial^2 u_j^*}{\partial x_i^* \partial x_i^*} + \theta_T^* \cdot f_j^*, \quad (2.1)$$

Energy:

$$\frac{\partial \theta_T^*}{\partial t^*} + u_i^* \frac{\partial \theta_T^*}{\partial x_i^*} = \frac{1}{(Gr_{source}^{fire})^{1/3} Pr} \frac{\partial^2 \theta_T^*}{\partial x_i^* \partial x_i^*} + \dot{q}^*, \quad (2.2)$$

where the independent variables are dimensionless time, $t^* = t_{fire} (g/L_f)^{1/2} (Q^*)^{1/3}$,

and dimensionless position, $x_i^* = x_i / L_f$. A dimensionless source strength parameter

$Q^* = \beta_T Q (\rho_0 c_p g^{1/2} L^{5/2})^{-1}$ where $\beta_T = 1/T_0$ has been used for scaling. The

dependent variables are dimensionless velocity, $u_j^* = u_j (gL_f)^{-1/2} (Q^*)^{-1/3}$,

dimensionless density difference, $\theta_T^* = \beta_T(T - T_0)(Q^*)^{-2/3}$, dimensionless pressure, $p^* = p(Q^*)^{-2/3}(\rho_0 g L_f)^{-1}$, and volumetric energy release rate $\dot{q}^* = \dot{q}''' L_f^3 \dot{Q}^{-1}$. It should be noted that for a point source, \dot{q}^* can be described by the Dirac delta function, $\dot{q}^* = \delta^3[x_i^* - (x_i^*)_{source}]$, the body force is given by $f_j^* = (0, 0, -1)$. Finally, a source based dimensionless Grashof number, $Gr_{source}^{fire} = g\beta_T \dot{Q} L_f^2 / \rho_0 c_p v^3$, and Prandtl number, $Pr = \nu/\alpha$, also appear explicitly in the diffusion terms as governing parameters.

Governing equations in salt-water plume:

Momentum:

$$\frac{\partial u_j^*}{\partial t^*} + u_i^* \frac{\partial u_j^*}{\partial x_i^*} = -\frac{\partial p^*}{\partial x_i^*} + \frac{1}{(Gr_{source}^{sw})^{1/3}} \frac{\partial^2 u_j^*}{\partial x_i^* \partial x_i^*} + \theta_{sw}^* \cdot f_j^*, \quad (2.3)$$

Salt Mass Species:

$$\frac{\partial \theta_{sw}^*}{\partial t^*} + u_i^* \frac{\partial \theta_{sw}^*}{\partial x_i^*} = \frac{1}{(Gr_{source}^{sw})^{1/3} Sc} \frac{\partial^2 \theta_{sw}^*}{\partial x_i^* \partial x_i^*} + \dot{w}_{sw}^*, \quad (2.4)$$

where the independent variables are dimensionless time, $t^* = t_{sw} (g/L_{sw})^{1/2} (m_{sw}^*)^{1/3}$, and dimensionless position, $x_i^* = x_i / L_{sw}$. A dimensionless source strength parameter $m_{sw}^* = \beta_{sw} \dot{m}_{salt} (\rho_0 g^{1/2} L_{sw}^{5/2})^{-1}$ where $\beta_{sw} = 0.76$ has been used for scaling. The dependent variables based on the source scale are dimensionless velocity, $u_j^* = u_j (g L_{sw})^{-1/2} (m_{sw}^*)^{-1/3}$, dimensionless density difference, $\theta_{sw}^* = \beta_{sw} Y_{salt} (m_{sw}^*)^{-2/3}$, dimensionless pressure, $p^* = p (m_{sw}^*)^{-2/3} (\rho_0 g L_{sw})^{-1}$, and dimensionless volumetric

energy release rate $\dot{w}_{sw}^* = \dot{w}_{salt} L_{sw}^3 \dot{m}_{salt}^{-1}$. Similar to the fire, it should be also noted that for a point source, $w_{sw}^* = \delta^3 [x_i^* - (x_i^*)_{source}]$, the body force is given by $f_j^* = (0, 0, -1)$. Finally, a source based dimensionless Grashof number, $Gr_{source}^{sw} = g\beta_{sw}\dot{m}_{salt}L_{sw}^2/\rho_0v^3$, and Schmidt number, $Sc = v/D$, also appear explicitly in the diffusion terms as governing parameters.

The familiar dimensionless source strength, Q^* , used in the fire induced flow should be compared to the analogous dimensionless source strength for the salt-water flow, m_{sw}^* , with the source strength being determined by the mass flux of salt being introduced into the flow. In previous scaling analysis, β_{sw} for the salt-water modeling is simply considered as one [27]. In this study, β_{sw} is refined as a constant equal to 0.76 based on the relationship between salt mass fraction and salt water density [28]. For the fire, β_T is the well-known thermal volumetric expansion coefficient equal to $1/T_0$ approximated from the ideal gas state equation for a flow with small density changes. The non-dimensionlization is performed in terms of the Grashof number instead of Reynolds number because the Gr can be easily expressed in terms of heat or mass source that drives the flow. The source based Gr can be related to the Re if the velocity scale is given by the plume characteristic velocity, $U = (Q^*)^{1/3}(gL)^{1/2}$ (refer to Appendix A). With this definition, it can be shown that $Re = Gr^{1/3}$.

Equations (2.1) and (2.3) clearly show the same dimensionless forms of the momentum equations in both fire induced flow and salt-water flow configurations. The comparison between Eq. (2.2) and Eq. (2.4) also indicate the dimensionless

transport equations for energy in the fire induced flow and salt mass species in the salt-water model have similar form with appropriate scaling. Furthermore, the definition of the dimensionless density difference θ_T^* and θ_{sw}^* are also analogous using a source based non-dimensionalization approach. Similar behaviour is expected for the dimensionless density difference θ_T^* and θ_{sw}^* once the boundary conditions of fire induced flow and salt-water flow are matched. For unconfined flows, such as the free plume, details regarding the boundary condition don't need to be considered. However, if ceilings or walls are present in the flow domain of interest, the boundary condition in the salt-water configuration requires some interpretation. The impermeable boundary condition resulting in zero mass fraction gradients at the wall in the salt-water configuration is analogous to the adiabatic boundary condition in the fire configuration.

2.1.2 Dimensionless Parameter Strategy

As discussed in previous studies [27, 29, 30], the scaling techniques are not able to match all of the governing dimensionless groups in all cases causing inconsistent flow characteristics between the scale model flow and real flow. Discrepancies in the Gr , Pr , and Sc between the fire and salt-water configurations may cause the flows to behave differently. Nevertheless, if the Gr number is sufficiently large to create a turbulent flow in both configurations, the molecular diffusion will be relatively small compared to the turbulent mixing. Differences in molecular properties and their associated dimensionless parameters can be neglected. However, near the bounding surface, the gradients of velocity or temperature become

steep and the diffusive terms may not be negligible. The differences in the Gr , Pr and Sc between the fire and salt-water model configuration may become important near the bounding surface. In this study, the importance of these parameters in the boundary layer is evaluated by comparing the salt-water measurements in the impinging ceiling jet configuration with real fire experiments. Good agreement between salt-water modeling measurements and the fire data indicates the effects caused by the differences between these parameters are negligible in fully turbulent flow (refer to §3.2.3).

2.2 Experimental Facility

The salt-water modeling study is conducted in the Fire Engineering and Thermal Science Laboratory (FETS) at the University of Maryland, College Park. The experimental facility used in this study has been applied in previous salt-water modeling studies by Steckler [4] and Jankiewicz [3]. As presented in Fig. 2.2, the experimental apparatus consists of four parts, which include a gravity head delivery system, an injection system, a laser and optics system and an image acquisition system. The gravity head delivery system is used to supply salt-water to the injection system at a fixed flow rate. Salt-water is released into a large fresh water tank from the injector. A laser sheet is created to illuminate a plane across the flow field in the PLIF measurements. The fluorescent images are recorded by an image acquisition system for post processing. In the velocity measurements, the diode laser is placed at position I to measure the centerline vertical velocity of the salt-water plume and at position II to measure the horizontal velocity in the ceiling jet. Such arrangement is

made to keep the shortest light path through the salt-water flow in the experiment. Following sections will describe each system of the experimental facility in detail.

2.2.1 Experiment Setup

A gravity feed delivery system is used to maintain a constant flow during the experiments. As shown in Fig. 2.2, the delivery system consists of an upper container, in which the gravity head is maintained constant, and a lower container that serves as an overflow compartment. A series of PVC pipes connecting the two containers allow the solution to be circulated within the delivery system. An inline

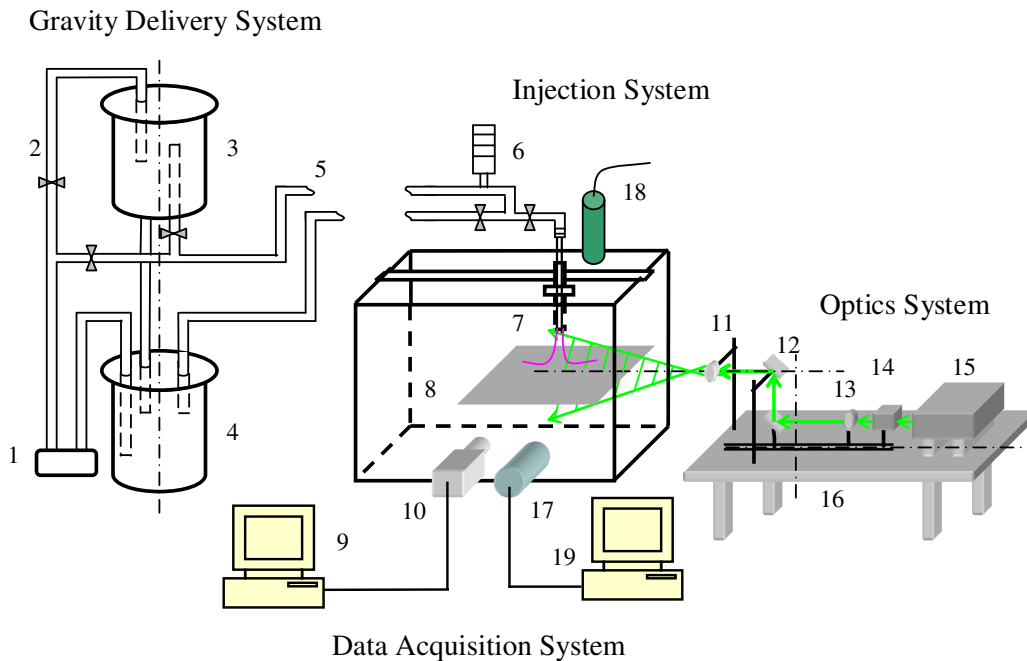


Figure 2.2: Quantitative salt-water modeling facility with PLIF/LDV diagnostics; impinging plume configuration shown. (1) circulating pump; (2) control valve; (3) top tank; (4) bottom tank; (5) PVC pipe; (6) flow meter; (7) injector; (8) fresh water tank; (9) PLIF data acquisition computer; (10) COHU CCD camera/Canon Camera; (11) expanding cylindrical lenses; (12) flat mirror; (13) collimating lens; (14) spatial filter; (15) Argon Ion Laser; (16) laser table; (17) Diode Laser Probe (position I); (18) Diode laser Probe (position II); (19) LDV Data acquisition computer

pump is used to constantly deliver salt water from the bottom container to the top container. Once the salt-water level in the top container is higher than the top of the return pipe, the excess salt water returns to the bottom container. In this way, a constant gravity head is maintained during the experiment to isolate the fluctuations from the pump. The cylindrical containers used in the gravity delivery system are covered by black plastic to reduce decomposition of the Rhodamine dye associated with ambient light exposure.

Control valves are installed along the flow routine regulating the direction of the flow from the gravity feeding system. The mixed saline solution from the gravity feed tank goes through a flow meter before it is injected to the fresh water tank. A Gilmont glass flow meter (Model GF-6541-1230) is used to adjust and monitor the volumetric flow rate. The reading of the flow meter is on a (0-100) scale with a $\pm 5\%$ uncertainty. A calibration program named Gilmont Flow Rate Analysis is applied to convert the scale readings to actual flow rates. The impact of this effect on experimental uncertainty is discussed in detail in §2.4.1. A three-way valve is placed downstream of the flow meter directing saline solution to the injector or back to the bottom container for recirculation.

A large capacity tank (1.7 m \times 0.9 m \times 1.2 m) is filled with fresh water to provide an ambient environment for the salt-water plume experiments. The saline solution coming from the flow meter is injected into the fresh water through a stainless steel tube. The internal diameter of the tube is 5.6 mm. The injector is connected to a two dimensional traverse allowing controlled vertical and horizontal positioning. The injector location is adjusted within the laser sheet plane (x_1 - x_3) to

explore the flow dynamics in different flow regions. The precision of the movement along the x_1 and x_3 direction is ± 0.1 mm.

The ceiling plate used in this study is an acrylic plastic plate (610 mm \times 610 mm \times 12.7 mm). The plastic plate is painted black to reduce the laser light reflections caused by the plate for the PLIF measurements. On the other hand, a transparent acrylic plate is used in the ceiling jet velocity measurements allowing the LDV laser beam to pass through it. As a result, the light scatter effects on the LDV signal caused by the ceiling plate are minimized. A ceiling supporting frame constructed with Bosch aluminum framing was placed in the fresh water tank to support the ceiling plate during the impinging plume experiments. The ceiling plate rests on a set of threaded rods and nuts. The level of the ceiling plate is regulated by adjusting the nuts. Since it takes considerable efforts to setup the ceiling plate, it will remain fixed through the experiments. The injector position is adjusted between measurements to achieve different ceiling heights.

In the large fresh water tank, there is unavoidable large vortex motion affecting the axisymmetric shape of the salt-water plume. A transparent enclosure is used to isolate the salt-water plume from these ambient flow effects and force the flow to be symmetric. The transparent enclosure is made of 4 pieces of acrylic plastic plate (610 mm \times 610 mm \times 6.4 mm each) providing a relatively large space for the salt-water plume experiments. For the impinging plume experiments, the transparent closure is elevated 51 mm above the ceiling plate in order to avoid distorting the unconfined ceiling jet behavior.

2.2.2 Planar Laser Induced Fluorescence (PLIF) System

Planar Laser Induced Fluorescence (PLIF) is used in this study to measure the salt mass concentration in salt-water plumes. Assuming the dye tracer and salt dilute at the same rate, the salt mass concentration is directly proportional to the dye concentration. This non-intrusive technique provides researchers with a simple and convenient flow-marking scheme for measuring passive scalar quantities such as concentration [31-33]. Light from the incident light sheet is absorbed by the dye tracer present in the flow and re-emitted in all directions in a wavelength range characteristic of the specific dye tracer used. The intensity of the fluoresced light is proportional to the local dye concentration and the incident laser light intensity. Using a camera at a right angle to the laser sheet, two dimensional images of the fluoresced light distribution are obtained when the laser sheet passes through the flow. After careful calibration, the fluorescent light intensity distribution is converted to a dye concentration distribution. Detailed components of the PLIF system are provided in this section.

Laser System

The light source is generated with an air cooled Argon-Ion Laser (175-F01 Sepctra-Physics Laser, Inc.) for the PLIF measurements. The laser has maximum total power of 500 mW and delivers light at wavelengths of 458 nm, 488 nm, and 514.5 nm, with 514.5 nm wavelength being the primary line. The laser and the entire optics system are fixed to a table (as shown in Fig. 2.2).

Optics System

Since the fluorescent intensity of the dye is directly related to the laser light intensity, it requires a light sheet with a well-defined intensity profile in the PLIF measurements. However, the Argon-Ion laser produces an imperfect Gaussian light intensity profile caused by imperfections in the laser optics. A spatial filter is used in the optical system to remove imperfections in the beam intensity profile and produce a “clean” Gaussian light sheet. The spatial filter is composed of a laser singlet and a high intensity pinhole, both of which are aligned using a micro-traverse system. The imperfect laser beam is focused down to a point exactly at the pinhole aperture by the laser singlet. The spatial noise of the laser beam is removed after it passes through the pinhole. After the spatial filter, the laser beam is collimated by a collimating lens. Then it is redirected by a series of optical mirrors. Finally, the collimated beam is passed through a cylindrical lens with 8.0 mm focal length that refocuses the light into a light sheet with 0.5 mm thickness and useable width greater than 150 mm.

Because of the Gaussian light intensity distribution, the vertical location of the light sheet is of great significance. Preliminary tests have to be conducted to locate the optimal light sheet dimensions and position for each measurement. This action is very important to ensure the laser sheet is introduced in such a manner that the area of most significance is adequately illuminated, while at the same time providing adequate illumination through out the entire spatial domain. Once the laser sheet has been set at the optimum condition, it will remain fixed throughout the measurement.

Dye Tracer

Rhodamine 6G (99.9% purity, Lycros Chemicals Inc.) is selected as the fluorescent dye in the current study because its peak absorption wavelength is at 530 nm, close to the dominant line of the Argon Ion laser. The peak emission of Rhodamine 6G occurs at a longer wavelength, near 560 nm. A high pass interference filter with a cut off wavelength of 550 nm was placed in front of the camera to prevent imaging of any reflected laser light. The interference filter effectively isolates the orange light produced by the dye fluorescence, which can be related directly to the salt-water concentration.

Data Acquisition System

In the PLIF measurements, an 8-bit COHU 4910 series high performance monochrome CCD camera was used in all unconfined plume experiments providing a resolution of 750 (H) \times 480 (V) pixels. A 75 mm lens with $f/1.2$ provides a spatial resolution of 160 μm (H) \times 320 μm (V) when imaging large portions of the flow. In order to resolve the turbulent details of the flow, a 200 mm lens with $f/2.8$ is used providing a spatial resolution of 40 μm (H) \times 80 μm (V), which is smaller than the Kolmogorov length scale of the salt-water flow in the far field (e.g. $\lambda_\tau = 100 \mu\text{m}$ at $x_3^+/D = 20$). An EPIX image acquisition board is used to digitize the images collected with the CCD camera. The data acquisition program, XCAP, is used to initialize the capture and storage process of the digitized images. The average recording rate is only 3 Hz due to the limitations of camera response time and data transfer rate from the camera to the computer. The instant images are first recorded

as a binary video file. A macro written within XCAP program is used to separate the binary file and convert it into a series of tiff images for post processing. Typically 500 images are collected in each video file for processing and analysis.

A Canon EOS D30 digital camera substitutes the COHU 4910 in later PLIF impinging plume experiments to reduce the Modulation Transfer Function (MTF) effects near the ceiling surface. The MTF describes the ability of a lens or system to transfer object contrast to the image. It is used as a quantitative measure of image quality and the feasibility of the overall imaging system. At the ceiling surface, there is a sharp gradient of the light intensity. The grey level jumps from almost zero (at ceiling surface) to a relatively high number (about 200 in the ceiling jet) within a distance of approximately 2 pixels. However, the digital camera can not capture this large spatial light intensity gradient and requires several pixels to transition from black to white making it impossible to characterize behavior near the ceiling. The spatial response is improved by using the Canon D30 SLR camera and a Canon 50 mm (f/1.4) lens. In the current study, valid data was obtained at a position from the ceiling of about $0.005H$ corresponding to 15 pixels from the ceiling. The first valid pixel is measured from the grey level profile from the ceiling plate to the ambient fluid with a uniform dye concentration. Another benefit of using the Canon D30 SLR camera is that it can provide 12-bit images with high resolution. The drawback of increasing the image depth and resolution is the image acquisition rate is very slow. Thus the images captured by the Canon camera still use 8-bit format in order to record enough images in a short period. The image resolution is increased to $1440(H) \times 960(V)$ with a spatial resolution of $90 \mu\text{m} \times 90 \mu\text{m}$ when imaging large portions of

the flow. A bright 50 mm lens with f/1.4 is used to increase the signal strength during the measurements. The average image acquisition rate decreases to 1 Hz which takes longer time to collect enough sample images. All images captured by the digital camera are stored in a Compact Flash memory card first and then transferred to the computer for post processing. Considering the long recording time, only 300 instantaneous images are recorded for each condition. It should be noted that the image capture by the Canon camera is a color image. This color image is converted to a black/white image using the general relationship between RGB luminance and grey scale (i.e. $GL = 0.3\text{Red} + 0.59\text{Green} + 0.11\text{Blue}$). This conversion method provided excellent agreement with plume theory.

Measurement Theory

The salt mass fraction can be derived from the PLIF images by carefully considering the relationship between the light intensity, dye concentration and salt mass concentration. The fundamental equation defining the relationship between the fluorescent intensity and dye concentration is [34, 35]

$$I_e(b) = I_0 \exp(-\varepsilon \int_0^b C(x_1) dx_1), \quad (2.5)$$

where $I_e(b)$ is the intensity of the excited beam at the point b along the beam path distance, I_0 is the incident light intensity, ε is the ‘extinction coefficient’ of the dye, $C(z)$ is the dye concentration at x_1 and b is the absorption path length. Guilbault [34] stated that, a linear response of fluorescence with respect to concentration can be obtained only when less than 5% of the exciting light is absorbed. If there is no light absorption along the beam path, a linear relationship can be established between the

mass concentration of the dye, C_{dye} , and normalized light intensity (in terms of grey level), GL , as

$$GL = a_0 \cdot C_{dye}, \quad (2.6)$$

where a_0 is a calibration coefficient. The method of achieving a_0 is provided in Appendix B. Assuming the dye tracer is completely dissolved and the dye and the salt dilute at the same rate, the mass concentration of dye is directly proportional to the mass concentration of salt as

$$C_{dye} = a_1 \cdot C_{salt}, \quad (2.7)$$

where a_1 is determined by the initial dye and salt mass concentrations at the injection location. Based on the definition of salt mass fraction, the salt mass concentration can be expressed in terms of salt mass fraction as

$$C_{salt} = \frac{m_{salt}}{V_{sw}} \frac{\rho_{sw}}{\rho_{sw}} = Y_{salt} \cdot \rho_{sw}, \quad (2.8)$$

where ρ_{sw} is the density of salt water. Furthermore, an expression for the salt-water density as a function of the salt mass fraction can be determined empirically [28],

$$\rho_{sw} = (1.0 + \beta_{sw} \cdot Y_{salt}) \cdot \rho_0, \quad (2.9)$$

where $\beta_{sw} = 0.76$ and ρ_0 is the density of fresh water. Substitution of Eq. (2.8) and Eq. (2.9) to Eq. (2.7) results in

$$C_{dye} = a_1 \cdot Y_{salt} \cdot (1.0 + \beta_{sw} \cdot Y_{salt}) \cdot \rho_0. \quad (2.10)$$

Substituting Eq. (2.10) into Eq. (2.6) yields

$$GL = a_0 \cdot a_1 \cdot Y_{salt} \cdot (1.0 + \beta_{sw} \cdot Y_{salt}) \cdot \rho_0. \quad (2.11)$$

The mass fraction Y_{salt} is thus expressed as

$$Y_{salt} = \frac{-a_0 a_1 \rho_0 + \sqrt{(a_0 a_1 \rho_0)^2 + 4a_0 a_1 \beta_{sw} \rho_0 GL}}{2a_0 a_1 \beta_{sw} \rho_0}. \quad (2.12)$$

The negative solution of Eq. (2.12) is not physically realizable. Finally, the mass fraction field for Y_{salt} can be used to analyze the temperature distribution in fire based on the dimensionless analogy discussed in §2.1. Details regarding PLIF salt-water experiments are provided in §2.3.2.

2.2.3 Laser Doppler Velocimetry (LDV) System

Laser Doppler Velocimetry (LDV) is another laser diagnostic technique applied in this study. The LDV technique has been recognized as a well established non-intrusive technique for fluid velocity measurement. This approach is particularly effective for liquid flows since the necessary seeding particles can often be found as natural impurities that are known to follow the turbulent motions more faithfully than in air or gas flows under most circumstances. Apart from the limitation that the LDV technique does not provide the instantaneous spatial structure, it provides information on the mean velocity and its turbulent fluctuations with a high degree of accuracy over a large dynamic range. Detailed components of the LDV system are provided in this section.

Laser System

The laser system in the LDV measurements is much simpler compared to the PLIF measurements. The light source is generated with a SUREPOINT Diode Laser Probe (Model 6810, TSI, Inc.). The SUREPOINT Laser Probe is essentially a

complete backscattering LDV optical system in a compact easy to use form. This Laser Probe system contains an optical head and a power supply/control unit. It has been designed and built to permit point LDV measurements. The Laser has maximum total power of 30 mW and delivers light at 780 nm. The laser is mounted on a 2D traverse system allowing the laser to move easily along horizontal and vertical directions (x_1 - x_3 plane). The precision of the movement along the x_1 direction is ± 0.1 mm and that of the x_3 direction is ± 0.001 mm.

Optics System

A diagram of the probe optics in a backscattering LDV system is illustrated in Fig. 2.3 to explain the measurement theory. The solid-state laser diode is used to generate a near infrared laser beam. The highly divergent rays of light emitted from the laser are formed into parallel rays by the collimating lens. The collimated light

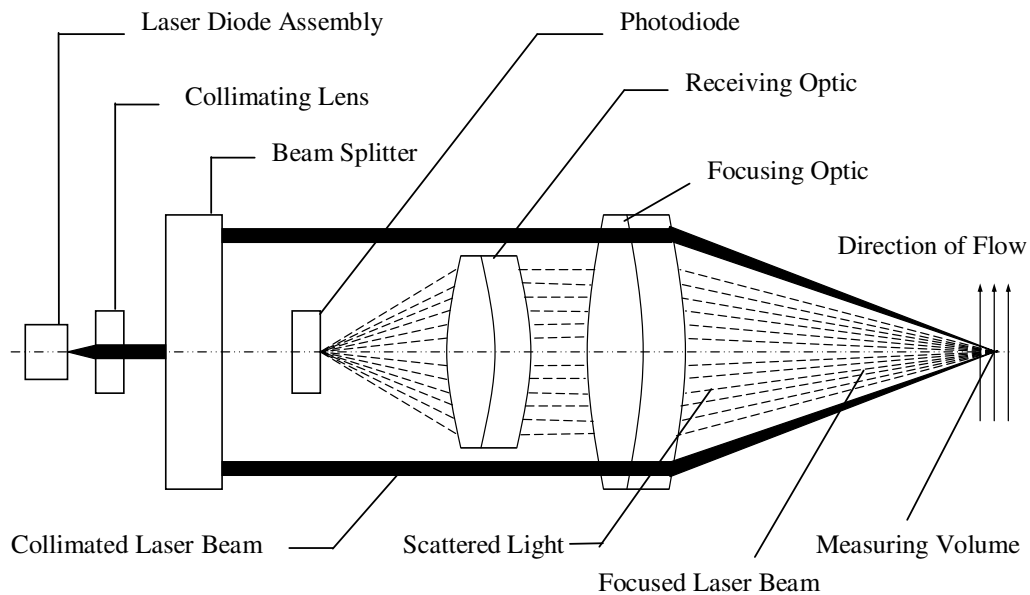


Figure 2.3: Optical schematic of backscattering LDV Probe

beam is then split into two separate beams using a beam splitter. These two light beams are then focused down into a spot by the front focusing lens. The area where the spot is formed is called the beam crossing (also referred to as the measurement volume). The size of the focused light spot is determined by the size of the laser beam and the focal length of the lens used. Light is scattered as particles pass through the beam crossing. The frequency of the scattered light provides the information of the particle velocity.

Data Acquisition System

The backscattering light is collected by the receiving optics and converting into an electrical signal with a photodiode. The signals are sent to the IFA 550 signal processor which connects the laser probe to the data acquisition system. A desktop computer is used to collect and analyze the data with the FIND program. FIND controls the processing of the IFA 550 signal processor and provides complete flow statistics for every measured point. It calculates and displays all basic flow statistics, including mean velocity, standard deviation, turbulence intensity, shear stress, and correlation coefficients. [36].

Measurement Theory

Due to the wave nature of the light, interference fringes will occur at the two beam crossing section represented by light and dark lines. The fringe space, s , is produced according to

$$s = \frac{\lambda}{2 \sin(\alpha/2)}, \quad (2.13)$$

where α is the angle of the two beams and λ is the beam wavelength [37]. In the current study, the distance between the two interfered beams is 50 mm. The major axis of the beam crossing is 222 μm and the minor axis of the beam crossing is 108 μm when a 350 mm focal length lens is used (the beam crossing angle is 3.97°). There are 19 fringes in the beam crossing with a 5.7 μm fringe spacing.

When a particle moving with velocity u normal to the fringe planes, it will experience a modulation of light intensity and scatter light into all directions. The scattered light is shifted due to the velocity of particles in what is known as a Doppler shift frequency, f_D , where

$$f_D = \frac{u}{s}. \quad (2.14)$$

Some of this scattered light is gathered through the front lens of the probe and is focused onto a photodetector by a receiving lens. The photodetector converts the frequency data to electrical impulses. The signals are sent to the IFA 550 signal processor which is connected to the data acquisition computer. Finally, the velocity of the particle is derived from the measured Doppler shift frequency of the particle using FIND program.

2.3 Experimental Methodology

In this study, the salt-water modeling technique is adapted to allow quantitative analysis of the flow dynamics in classical fire configurations using laser diagnostics. The experimental procedure follows a detailed methodology in order to achieve high fidelity and quantitative measurements. Special attention must be paid

to the initial flow condition, light absorption effects in the PLIF measurements and the ability of the seeding particles to follow the flow in LDV measurements. Detailed discussions of these issues are provided in this section.

2.3.1 Initial Conditions of Salt-Water Experiments

In order to properly model the fire behavior, the salt water must be carefully injected to create an appropriate buoyant source for the model. Flow conditions of the salt-water model are prescribed for the experiment to ensure that the flow is buoyancy dominated and turbulent. Appropriate specifications of these criteria are essential to ensure that the mixing dynamics are similar to those in a fire induced flow. The detailed initial conditions of each experimental case are listed in Table 2.1. Special characteristic scales such as specific momentum flux and specific buoyancy flux which control the initial flow condition will be discussed in this section.

Source Definition

The non-negligible initial momentum makes the salt-water flow behave like a jet near the injection source. This initial jet-like behavior differs from the immediate buoyancy dominated behavior near the source in an accidental fire. However, the initial momentum of the salt-water plume becomes unimportant at a distance not close to the source where buoyancy dominates the flow dynamics. In the current study, the appropriate source strength is selected to ensure the initial momentum of the salt-water jet is minimized and the flow reaches plume-like behavior quickly.

Table 2.1 Initial experimental conditions in salt water modeling measurements

	Case 1	Case 2	Case 3	Case 4	Case 5	
Experimental Configurations and Measurements						
Flow Configuration	Unconfined Plume	Unconfined Plume	Unconfined Plume	Impinging Plume	Impinging Plume	
Ceiling Height, H_c (mm)	N/A	N/A	N/A	206	235	
Injector Diameter, D (mm)	5.6	5.6	5.6	5.6	5.6	
Measurements	PLIF/LDV	PLIF	LDV	PLIF/LDV	LDV	
Initial Flow Conditions of Salt-Water Plume						
Volume Flow Rate \dot{V} (ml/min)	110	165	110	110	110	
Salt Mass Fraction, Y_{salt}	0.13	0.13	0.10	0.13	0.10	
Injection Velocity, U_{inj} (mm/s)	74	112	74	74	74	
Characteristic Scales						
Virtual Origin (mm) ⁽¹⁾	$(z_0)_\theta$	-11.8	-18.5	N/A	10.2	N/A
	$(z_0)_U$	53.6	N/A	77.5	53.6	77.5
m_{sw}^* ($\times 10^{-6}$)	N/A	N/A	N/A	3.74	2.0 ⁽²⁾	
Characteristic Length Scale, D^* (mm)	1.33	1.55	1.18	1.33	1.18	
Re_D	434	651	434	434	434	
Characteristic Velocity U (mm/s)	N/A	N/A	N/A	21.5	18.7	
Re_H	N/A	N/A	N/A	4389	4379 ⁽²⁾	
$Gr_H \times 10^{10}$	N/A	N/A	N/A	8.45	8.39 ⁽²⁾	
Momentum Flux, M ($\times 10^{-7} \text{ m}^4/\text{s}^2$)	1.82	4.09	1.82	1.82	1.82	
Buoyancy Flux, B ($\times 10^{-6} \text{ m}^4/\text{s}^3$)	1.62	2.43	1.27	1.62	1.27	
Morton Length Scale L_M (mm)	6.9	10.4	7.8	6.9	7.8	

⁽¹⁾ $(z_0)_\theta$ is the source based virtual origin, $(z_0)_U$ is the velocity based virtual origin.

⁽²⁾ value is calculated based on the $(z_0)_\theta$ of case 4

Morton [8] defined a length scale based on the relative proportions of the source specific momentum flux M and buoyancy flux, B ,

$$L_M = M^{3/4} / B^{1/2} \quad (2.15)$$

The momentum flux, M , and the buoyancy flux, B , are defined as (assuming Poiseuille flow)

$$M = 2\pi \int_0^{D/2} U^2 r dr = \frac{\pi}{3} U_{inj}^2 D^2, \quad (2.16)$$

$$B = 2\pi \int_0^{D/2} U g \frac{\rho_{source} - \rho_0}{\rho_{source}} r dr = \frac{\pi}{4} \frac{\rho_{source} - \rho_0}{\rho_{source}} g U_{inj} D^2, \quad (2.17)$$

where ρ_0 is the ambient fresh water density, ρ_{source} is the salt water density at the injection location, D is the injector diameter, U_{inj} is the mean inlet flow velocity. Morton demonstrated and others have verified that plume-like behaviour was achieved at a streamwise location of $5 \times L_M$ [8, 9, 38, 39]. The initial flow condition (i.e. U_{inj} and Y_{sw}) are adjusted to provide values for M and B that will result in relatively small Morton length scales enabling the flow to become buoyancy dominated after a short distance from the point of injection. In this study, the magnitude of the Morton length scale is of the order of the injector diameter D (refer to Table 2.1). Thus the salt-water flow can be considered as buoyancy dominated after approximately $5D$ downstream from the injection point. This prediction is consistent with PLIF measurements. However this guidance is not applicable to the velocity field of plume which has a much longer transient regime. This is because the $5 \times L_M$ criterion was only based on the scalar measurements.

Virtual Origin

The virtual origin has proven to be very useful and effective in correcting for the effects of initial injection momentum and finite injector geometry. The virtual origin is used to define a relative coordinate system, $x_3^+ = x_3 - z_0$, where a virtual source is located at $x_3^+ = 0$. The down stream buoyancy dominated plume will be considered as propagating from a point source at $x_3^+ = 0$. The value of the virtual origin is determined from the experimental data using the approach established by Heskested [10]. In this study, the virtual origin z_0 in the salt mass fraction measurements is in the range of $-18.5 \text{ mm} \leq z_0 \leq 10.2 \text{ mm}$, while the virtual origin z_0 based on the velocity measurement is in the range of $53.6 \text{ mm} \leq z_0 \leq 77.5 \text{ mm}$. The virtual origin is used to correlate data in terms of point source theory. It depends on when the flow becomes buoyancy dominated and when the flow transitions to a turbulent state. Even with the same initial condition, the transition region from laminar flow to turbulent flow can still vary resulting in different virtual origins (e.g. Case 1 and Case 4). Thus the virtual origin has to be estimated from each case.

2.3.2 PLIF Salt-Water Measurements

The PLIF technique can provide very accurate measurements. In order to realize this accuracy, significant attention must be given to the salt-water/dye solution preparation, injected dye concentration, camera settings and other experiment issues. A variety of experimental conditions must be coordinated for optimal image quality.

Salt-Water/Dye Solution Preparation

Water treatment is necessary for fresh water and salt water solution in the PLIF measurements. Any particles suspended in the water will affect the laser sheet during the measurements. In order to remove these particles, fresh water is filtered through a high capacity 50-micron filter before it is introduced into the large tank. Salt water is filtered through a carbon based 5 micron filter using a submersible pump (such particle filtration procedure is avoided in the LDV measurements since these particles enhance the seeding density increasing the measured signal). Fresh water and salt water are left to dwell for a relative long time (more than 4 hours) to ensure they have the same ambient temperature. This action will reduce the extra buoyancy force caused by the temperature difference between salt water and fresh water. In current studies, the temperature difference between salt water and fresh water is less than 1 °C. The temperature difference effects on the density difference between the two fluids are negligible. A specified amount of premixed dye solution of 0.1 g/l is added to the saline solution to achieve the desired dye/salt concentration ratio. It has been observed by previous researchers that residual chlorine reacts with Rhodamine 6G [3]. The reaction causes a significant decay in the dye concentration with time. Chlorine is removed by adding a small amount of de-chlorinating agent to the solution.

Optimum Injected Dye Concentration

High dye concentration is always preferred in the PLIF measurements in order to increase the signal to noise ratio. However, high dye concentration may cause light absorption problems invalidating the linear relationship between the emitted light

intensity and the dye concentration. Thus the first step in implementing the PLIF technique is to select the correct injected dye concentration. Analysis has been conducted in this study to determine an optimal dye concentration at injection. This dye concentration should provide an intense fluorescent signal and avoid light absorption effects at the same time in the region of interest.

Figure 2.4 provides a comparison between the plume width, b_{pl} , and the acceptable incident light path length, b_{ab} , along plume streamwise locations. The injected dye concentration is assumed to be 0.2 mg/l. It should be noted that for this application to capture the entire plume, the plume width b_{pl} is defined as the location where $\bar{\theta} / \bar{\theta}_c = 0.01$. Also, the b_{pl} is multiplied by a safety factor of 1.1 to provide a conservative estimate. The acceptable incident light path length, b_{ab} , is the location where the excitation intensity is reduced to the minimum allowable value (i.e. $I_e = 0.95I_0$) derived from integration of Eq. (2.5) along the plume spanwise direction. Thus for $b_{pl} > b_{ab}$ (i.e. $I_e < 0.95I_0$), the linear relationship between light intensity and dye concentration does not hold anymore and PLIF measurements can not be used

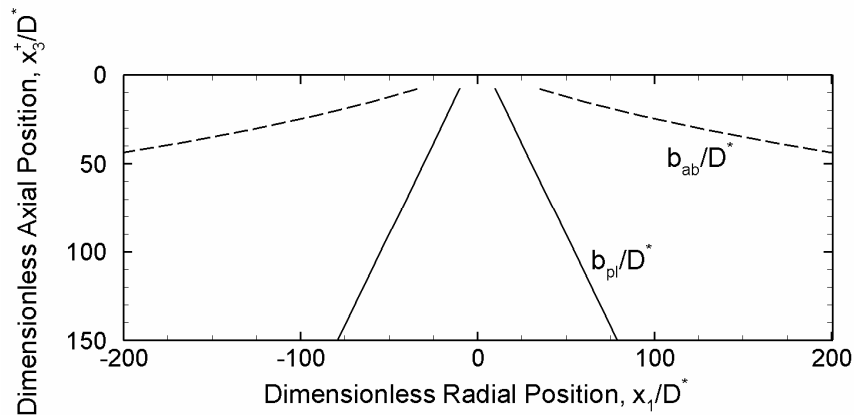


Figure 2.4: Comparison of plume width, b_{pl} , and the acceptable incident light path length, b_{ab} , ($C_{dye})_{inj} = 0.2$ mg/l

beyond this limit. As shown in Fig. 2.4, the plume width b_{pl} is always smaller than the b_{ab} with initial dye concentration of 0.2 mg/l. Thus a linear relationship between the fluoresced light intensity and the dye concentration would be expected for this injection dye concentration at all locations. This comparison also reveals that for a given injected dye concentration, the acceptable incident light path length becomes even larger than the plume width at locations downstream of the source. Therefore, if there is no significant light absorption in the upstream region, the light absorption will be even less significant at the downstream regions.

When the PLIF measurement focuses on a specific region of the plume, the injected dye concentration can be optimized to provide the best signal in the location of interest. The optimal injected dye concentration should be determined so that no light absorption is present in the measurement region. However, light absorption in the upstream is tolerated. The relationship between the injected dye concentration and associated light absorption across the plume width at specific downstream location is provided in Fig. 2.5. In this figure, the ratio of excited light intensity to the incident light intensity, I_e/I_0 , defined by Eq. (2.5) is plotted versus the injected dye concentration, $(C_{dye})_{inj}$, at selected plume downstream locations (i.e. $x_3^+/D^* = 15, 25, 50, 75$). At each location, there is a linear relationship between I_e/I_0 and $(C_{dye})_{inj}$. Based on previous analysis on light absorption, the critical line $I_e/I_0 = 0.95$ is provided along with other possible light absorption criteria, $I_e/I_0 = 0.93$ and $I_e/I_0 = 0.97$. In this study, $I_e/I_0 = 0.95$ is the selected maximum tolerance for light absorption. The maximum injected dye concentration can be determined when the allowable light absorption criterion is reached at the most upstream location in the

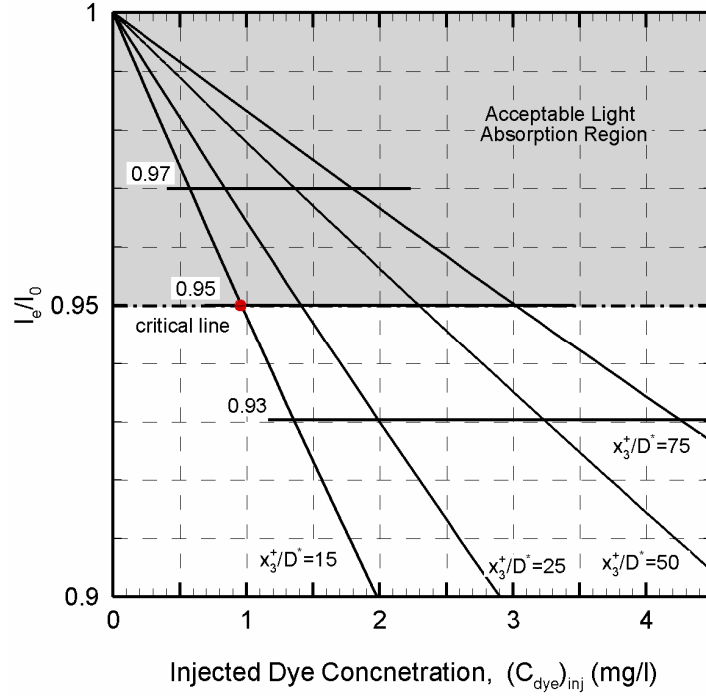


Figure 2.5: Recommended initial injected dye concentration

field of interest. For instance, at $x_3^+/D^* = 15$, the maximum dye concentration is given by the critical line intersection, $(C_{dye})_{inj_critical} \approx 0.95$ mg/l. The injected dye concentration should not exceed this critical dye concentration in the experiments, $(C_{dye})_{inj} \leq (C_{dye})_{inj_critical}$. In the current study, the injected dye concentrations used for various downstream location experiments are determined based on this guideline within the range from 0.2 mg/l to 1.5 mg/l.

Image Recording

Prior to each PLIF measurement, several reference images are taken to record the experimental geometry information. A standard scale is placed vertically in the path of the laser sheet. The camera is focused on the scale in the laser sheet plane.

An image is then recorded with the scale to represent the physical scale of the camera field of view. Another reference image is taken to record the relative position of injector and ceiling surface when used in the camera field of view. Assuming the center of injector exit is the origin of the x_1 - x_3 plane, the actual spatial location of each image is determined from these calibration images. The injector position, ceiling wall position and physical scale serve as input variables in the post processing programs.

Even when there is no fluorescent light in the flow section, the digital camera can still capture background noise. A series of background images are recorded for future background noise correction preceding each test. Prior to taking the instantaneous images, a high flow rate of saline solution is sent through the delivery tube to remove any air bubbles present in the injector or in the lines. The flow rate is then adjusted to that required for testing. Images are acquired once the flow reaches steady state (this takes about 3 minutes). 500 instantaneous images are randomly recorded for each measurement condition at an average rate of 3 Hz. In the later experiments using the Canon camera, only 300 instantaneous images are randomly recorded at an average rate of 1 Hz. These images serve as statistical samples to evaluate the flow dynamics. It should be noted that the Argon-Ion laser sheet light intensity is not uniform. The intensity distribution in the sheet follows an expanding Gaussian profile. The influence of the non-uniform excitation intensity distribution of the fluoresced light captured in the images is taken into account during the processing required for determining the salt-water concentration. After each

experiment, a series of calibration images are recorded in a small tank filled with a known dye concentration to correct for the non-uniform laser light intensity.

Post Processing

Several programs have been written in Interactive Data Language (IDL) to analyze the PLIF images. The foundation of these programs is based on converting an 8-bit tiff image into quantitative data. Each row and column of the image is scanned and the grayscale for each pixel within the image is converted into a numerical array. For the first stage of post processing a program reads in the raw background images and combines them into a single average background image. It is saved for further background noise correction. Taking the average of several hundred images allows the digital noise to be removed, leaving only the noise associated with the laser sheet itself. A similar program is used to create an average calibration image. The average background image is subtracted from the average calibration image in the program. The calibration image allows the laser sheet profile to be quantified spatially thus providing a means to normalize the experimental images.

The “average image” program uses several steps to average one or more instantaneous images. The program first converts each single image (1/60s, 480 × 752) into two numerical arrays (1/60s, 240 × 752) since the images obtained from the COHU camera are interlaced (This process is avoided for the image obtained from the Canon camera). All instantaneous images are added together and an average image is created. Then the average background image is subtracted from the average instantaneous image. After that, a multiplication factor coming from the calibration

image is applied to the average instant image to correct for the Gaussian light intensity distribution. Finally, the corrected gray level values are converted into the salt mass fraction according to their relationship shown in Eq. (2.12). The final salt mass fraction information is written in a data file which allows it to be opened in a separate data visualization program. TecPlot is used in this study. The data file consists of the spatial coordinates of each pixel, the gray level value and the salt mass fraction.

2.3.3 LDV Salt-Water Measurements

It is clear that the LDV measurements are highly dependent on signals from particles suspended in the flow, rather than on signals from the fluid itself. Depending on the optical configuration and the overall conditions, tracer particles must fulfill different requirements. Particles should be able to follow the flow with a negligible lag. Additionally, these particles should have good light scattering abilities to provide sufficiently strong signal during the measurements.

Seeding Particle Selection

The choice of optimal diameter for seeding particles is a compromise between dynamic tracer response and light scattering ability. An adequate tracer response of the particles in the fluid requires small particles while high signal to noise ratio of the scattered light signal necessitates large particles. The tracking capability of the seeding particles is of greater concern in this selection. The characteristic velocity response time of the particle, τ_p , is defined as [40]

$$\tau_v = \frac{(\rho_p - \rho_f)d_p^2}{18\mu_f} \quad (2.18)$$

where ρ_p is the density of the particle, ρ_f is the density of the conveying fluid, μ_f is the viscosity of the conveying fluid, d_p is the diameter of the particle. Another important characteristic is the terminal velocity of a particle which may add an offset velocity during measurements. The terminal velocity of the particle is expressed in term of response time as [37, 40]

$$(U_p - U_f) = g\tau_v \quad (2.19)$$

where U_p is the terminal velocity of the particle, U_f is the velocity of the conveying fluid. Silver Coated Hollow Glass Spheres (S-GHS) are selected as seeding particles in this study. The mean diameter of the S-HGS (SH400S20, Conduct-O-File) is 13 μm with density of 1.6 g/cm^3 . The thin silver coating further increases the reflectivity. The size distribution of these particles is between 6 and 33 μm . The velocity response time of these particle ranges from 1.3 μs to 37.9 μs , respectively, which is much smaller than the Kolmogorov time scale (about 6.5 ms at $x_3^+/D = 20$). The corresponding terminal velocity of the particle ranges from 1.2×10^{-5} to 3.7×10^{-4} m/s, respectively, which is two orders less than the mean flow velocity. Thus the particle is considered to follow the salt water well during the velocity measurements.

Measurement Procedure

In the LDV measurements, it is very important to ensure that beam crossing is focused at the expected measuring point (e.g. plume centerline). Preliminary measurements are conducted to measure the streamwise velocity distribution of

plume along both the x_1 and x_2 directions. The mean maximum velocity location is considered as the plume centerline position. The same procedure is repeated at different elevations of the plume configuration during the LDV measurements to ensure that laser beam is focused at the plume centerline.

As discussed before, a radially expanding ceiling jet is created in the impinging plume experiments. The long path of light in the ceiling jet can cause laser beam steering once the plume impinges on the ceiling, which prevents beam crossing for the LDV measurement in position I. In order to avoid the long path of light when measuring the ceiling jet velocity, the laser probe is displaced at the top of the water tank (i.e. Laser position II as shown in Fig. 2.2). During the ceiling jet velocity measurements, the ceiling plate uses a transparent acrylic plastic plate in order to reduce the scattering light effects from the ceiling surface. Once the laser beam is focused on the ceiling surface, only the noise will be measured. The ceiling position is considered to be at the first location where the noise is measured. Then the elevation of the laser probe is adjusted to measure the velocity distribution across the ceiling layer. Near the ceiling surface, the distance between two measuring points is 0.26 mm. Outside the boundary layer, the spatial interval is 0.67 mm.

When the laser probe of the LDV system is settled at position II (refer to Fig. 2.2), the difference of refractive index between air and fresh water will cause the distance that the laser probe moved in air, l_0 , different to the distance that the beam crossing moved in water, l_w . These two distances should be corrected by the index of refraction of water, n_w , (i.e. $l_w = n_w l_0$). Since the variation of fresh water surface will affect the beam crossing position, it is very important to maintain a steady fresh water

surface during the velocity measurement. In this study, the injector is located more than 10 cm underneath the fresh water surface. Thus the water surface is isolated from the fluctuation of the injection of salt water. Additionally, the fresh water in the test tank is drained out at the same rate as the injection of salt water to keep a steady water level.

2.4 Error Estimation

2.4.1 Index of Refraction Effects

In the application of laser diagnostics (PLIF and LDV), it is necessary to evaluate the index of refraction difference in the fresh water and salt water responsible for laser beams steering. In the current study, a salt-water solution with high salt concentration ($Y_{salt} = 0.13$) is injected into quiescent fresh water. The index of refraction of the salt solution is 1.356 at $Y_{salt} = 0.13$ [41] which is significantly larger than the index of refraction of fresh water (about 1.333). As described by previous researchers [42, 43], the index of refraction of salt water and fresh water can be matched using an appropriate combination of solutes. For example, the index of refraction of fresh water can be increased by adding ethanol or sugar into the fresh water. However, the large amount of solutes needed and the associated safety issues (e.g. evaporation of the ethanol) make these approaches impractical in the present experiment.

Nevertheless, the index of refraction effects are not as significant at downstream plume locations. As discussed previously, the salt mass concentration in

the plume decays rapidly with the distance from the injection following the (-5/3) power law. For instance, the salt mass fraction at injection (0.13) is reduced to less than 0.02 at $x_3^+/D = 10$. As a result the index of refraction in the plume is less than 1.336 beyond $x_3^+/D = 10$, which is only slightly higher than the index of refraction of fresh water (i.e. 1.333) by 0.225% [41]. In the current study, most measurements are focused on plume downstream locations further than $10D$ where the difference of the refractive index between salt water and fresh water are very small. Even with this small index of refraction, the effects on the beam crossing and laser sheet can not be neglected. Detailed discussion of the probe position shifting caused by the gradient of the index of refraction between fresh water and salt water are provided in the following sections.

Uncertainty of Beam Crossing Position in LDV Measurements

According to the law of refraction, the incident laser beam direction will change when it crosses the interface between two media which have different index of refractions. The relationship between the beam angle and index refraction is expressed as,

$$n_1 \sin i_1 = n_2 \sin i_2, \quad (2.20)$$

where i_1 is the incident beam angle, n_1 is index of refraction of medium 1, (e.g. air or fresh water), i_2 is the transmitted beam angle and n_2 is index of refraction of medium 2 (e.g. fresh water or salt water). It should be noted if the shape of the interface between the two media changes, the beam crossing position will change, correspondingly. As shown in Fig. 2.6, the two beams crossed at the location, $x_3 = l_1$,

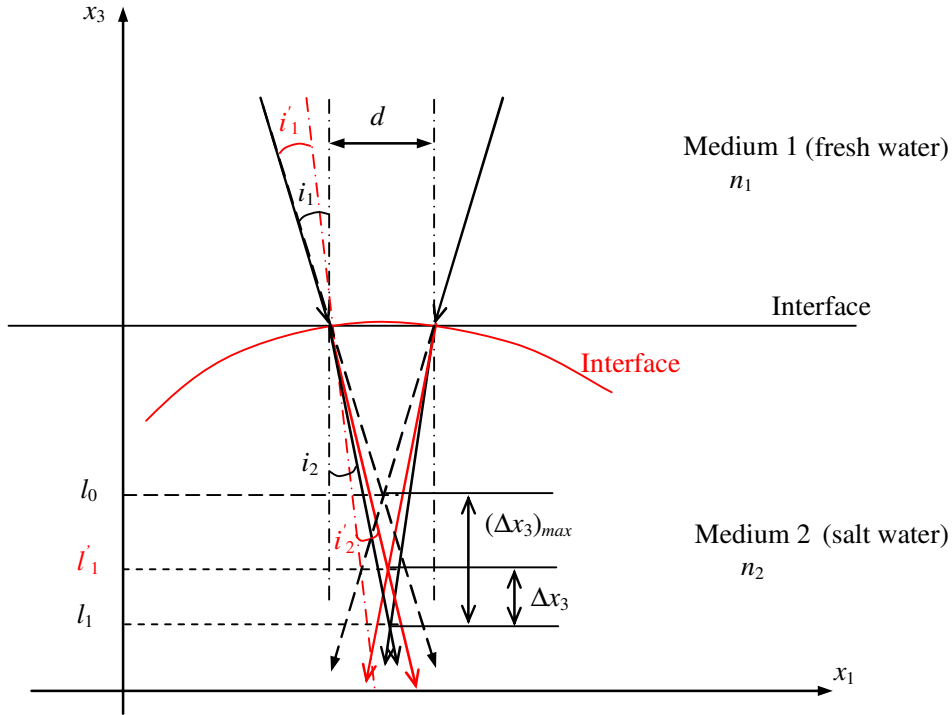


Figure 2.6: Interface effects on the beam crossing position

with an infinite radius of curvature between the fresh water and salt water. However, the interface may change to a small radius of curvature since the flow is turbulent in the current study. In this case, the incident beam angle changes from i_1 to i_1' resulting the transmitted beam angle changes from i_2 to i_2' according to the law of refraction. Since turbulence is three dimensional, the interface may steer each laser beam in an arbitrary direction and the beams may not cross at all. In the case that two laser beams do cross, the beam crossing position is shifted from location l_1 to l_1' by a distance Δx_3 in the x_3 direction. The positional uncertainties in the direction parallel to the interface (i.e. x_1 direction and x_2 direction) are relatively small compared to that in the normal direction (i.e. x_3 direction). The maximum variation of the beam crossing position along the x_3 direction occurs when there is no salt water along the

beam paths. Therefore, the beams go straight and cross at the location, $x_3 = l_0$. Considering the incoming beam angle, i_1 , in the fresh water is 2.98° , the transmitted beam angle, i_2 , in the salt water is 2.97° and the distance between two beam intersections, d , is about 2 mm, the maximum variation of the beam crossing position, $(\Delta x_3)_{max}$, can be estimated as

$$(\Delta x_3)_{max} = \frac{d}{2 \tan i_2} - \frac{d}{2 \tan i_1} \approx 43 \mu\text{m} \quad (2.21)$$

which is much smaller than the beam crossing size (about 200 μm). This uncertainty is also smaller than the Kolmogorov scale (about 100 μm). Thus effects of the uncertainty of the beam crossing position on the velocity measurements are negligible. However, the data acquisition rate dramatically decreases due to contamination of the signal from steered beams as opposed to complete normal crossing of beams.

Uncertainty of Laser Sheet Position in PLIF Measurement

Similarly, the laser sheet will bend when it crosses the salt water plume in the PLIF measurements. Figure 2.7 shows a top view of the salt water plume. The laser sheet with a thickness, δ , fluctuates in the region of δ' . This position variation provides a larger spatial sampling volume when doing the PLIF measurements. However, the salt mass fraction gradient inside the laser sheet is very small because the plume is axisymmetric and the laser sheet is always aligned to cross the plume centerline. Thus the uncertainty of the laser sheet will not significantly affect the mean value measured. The variation of the laser sheet position does bring errors in

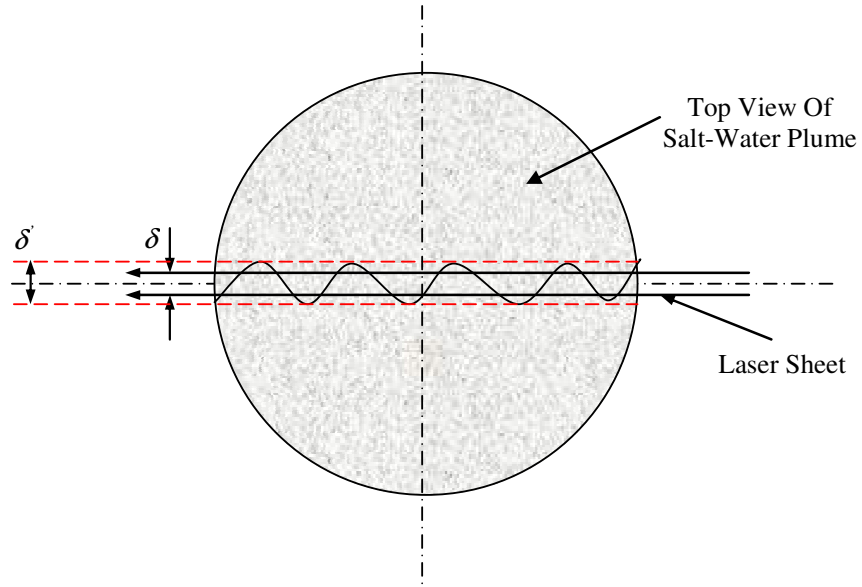


Figure 2.7: Uncertainty of laser sheet

the turbulent statistics analysis because the sampling volume is changed. However, compared with laser sheet thickness (about 500 μm), the uncertainty of the laser sheet shifting is expected to be relatively small. The error caused by the laser sheet shifting is negligible compared to other errors in the PLIF measurements (as discussed in §2.4.2.).

2.4.2 Uncertainty of Salt Mass Fraction Measurements

Although very careful experimental procedures have been followed to achieve precise quantitative measurements, there are still unavoidable uncertainties in the measurements. Equation (2.12) clearly shows the uncertainties of the image grey level GL , constant coefficient a_0 and constant coefficient a_1 will bring errors into the salt mass fraction measurements. In this section, the total error in the salt mass

fraction is estimated by quadratic analysis where the measurement quantity of interest is a function R of many variables such that [44]

$$R = R(w_1, w_2, w_3, \dots, w_n) \quad (2.22)$$

where w_i are basic measurement required to determine the measurement quantity of interest, R . Then the total uncertainty in R can be expressed as

$$\Delta R = \sqrt{\left(\frac{\partial R}{\partial w_1} \Delta w_1\right)^2 + \left(\frac{\partial R}{\partial w_2} \Delta w_2\right)^2 + \dots + \left(\frac{\partial R}{\partial w_n} \Delta w_n\right)^2} \quad (2.23)$$

where Δw_i is the respective uncertainties in the w_i values. The major sources of uncertainty for the salt mass fraction measurements are included below and an overall estimate of the uncertainty is also provided.

Uncertainty of the Image Grey Level, GL

In the PLIF measurement, the grey levels of the instantaneous image fluctuate over a certain range in the absence of concentration changes. This fluctuation is caused by two sources, the electrical noise of the camera system and the fluctuation of the laser power. Although these effects in the average image can be reduced by averaging out these random fluctuations over successive measurements, they can not be avoided in the instantaneous images presenting as a source of error for the PLIF measurements. In order to produce the maximum image depth in the PLIF measurements, the gain of the camera has to be adjusted to produce peak grey levels just below 255. But the noise in the instantaneous image will also increase with increasing gain. An optimal setup of the camera is required to reduce the background noise fluctuations and provide sufficient fluorescent signal. In the current study, the

fluctuation of noise in terms of grey level is controlled within ± 3 . This is about $\pm 5\%$ of characteristic grey level of the fluorescent signal (about 60). However, at the edge of the plume, the grey level may be smaller than 60, the uncertainty will be larger than the $\pm 5\%$.

Uncertainty of Constant Coefficient, a_0

According to the definition of a_0 in Appendix B, a_0 is the ratio of measured grey level in the calibration image, GL_{cal} , and the calibration dye mass concentration, $(C_{dye})_{cal}$. In order to reduce the error of a_0 , three sets of calibration images are recorded with various calibration dye concentration (i.e. $(C_{dye})_{cal} = 0.005$ mg/l, 0.010 mg/l and 0.015 mg/l) in this research. The constant a_0 is about 15000 coming from the linear curve fit from three calibration measurements with an error less than $\pm 2\%$.

Uncertainty of the Premixed Dye Mass Concentration, $(C_{dye})_{0.1}$

It is important to note that prepared laser dye solutions usually contain very minute amounts of dye. Thus the type of solvent used as well as its purity is of great importance. Impurities and additives may strongly affect the lifetime of the dye and may catalyze photochemical reactions. For this reason distilled water is used as the preliminary solvent. The pure dye is weighed using a precision digital scale with an accuracy of ± 0.0001 grams. An initial solution is made with a concentration of 0.1 g/l $\pm 0.02\%$. This high concentration dye solution is added to the saline solution in liquid state to achieve the desired dye/salt concentration ratio.

Uncertainty of Constant Coefficient, a_1

Another important source of error for the salt mass fraction measurement is the constant coefficient, a_1 , defined as the ratio of the initial dye mass concentration, $(C_{dye})_{inj}$, and the initial salt mass concentrations $(C_{salt})_{inj}$ at the injection location. The uncertainties of these two quantities are discussed in the following. Firstly, the injected dye concentration, $(C_{dye})_{inj}$, is determined by

$$(C_{dye})_{inj} = \frac{V_{0.1} (C_{dye})_{0.1}}{V_{sw}} \quad (2.24)$$

where $V_{0.1}$ is the volume of the premixed dye solution (0.1 g/l) added into the salt water, $(C_{dye})_{0.1}$ is the premixed dye concentration (0.1 g/l), V_{sw} is the volume of salt water solution prepared for each experiment (about 18 l). In the current study, the uncertainty of $V_{0.1}$, V_{sw} , $(C_{dye})_{0.1}$ are $\pm 0.5\%$, $\pm 0.5\%$ and $\pm 0.02\%$, respectively, yielding a quadratic uncertainty of 0.7% for $(C_{dye})_{inj}$. Secondly, the injected salt mass concentration, $(C_{salt})_{inj}$, is calculated by

$$(C_{salt})_{inj} = (Y_{salt})_{inj} \rho_{sw} = (Y_{salt})_{inj} (1 + \beta_{sw} (Y_{salt})_{inj}) \rho_0. \quad (2.25)$$

The initial salt mass fraction of the saline solution, $(Y_{salt})_{inj} = 0.13$, is measured by a saline scale. The accuracy of the measurement is ± 0.001 . Thus the quadratic uncertainty of $(C_{salt})_{inj}$ is 0.88% based on the 0.8% uncertainty of $(Y_{salt})_{inj}$ measurement. Finally, the quadratic uncertainty of a_1 is $\pm 1.1\%$.

Uncertainty of Measured Salt Mass Fraction, Y_{salt}

According to the quadratic error analysis in Eq. (2.23), the total uncertainty of Y_{salt} is determined as

$$\Delta Y_{salt} = \sqrt{\left(\frac{\partial Y_{salt}}{\partial GL} \Delta GL\right)^2 + \left(\frac{\partial Y_{salt}}{\partial a_0} \Delta a_0\right)^2 + \left(\frac{\partial Y_{salt}}{\partial a_1} \Delta a_1\right)^2}. \quad (2.26)$$

Substitution of each value into Eq. (2.26) yields

$$\Delta Y_{salt} = 9.7 \times 10^{-5}. \quad (2.27)$$

Considering the characteristic salt mass fraction, Y_{salt} , is about 0.002 in the current study, the characteristic error of Y_{salt} is about $\pm 5\%$.

Uncertainty of Source Independent Dimensionless Density Difference, θ^*

A Gilmont glass flow meter (Model GF-6541-1230) is used to adjust and monitor the volumetric flow rate in the current study. The uncertainty of the flow meter reading is less than $\pm 5\%$. Although the uncertainty of the flow rate does not affect the salt mass fraction measurement explicitly, it does cause about $\pm 5\%$ uncertainty on the dimensionless source strength, m^* . Also considering the $\pm 5\%$ uncertainty of Y_{sw} , the total uncertainty of the source independent mass fraction, θ^* , is about $\pm 7.1\%$.

2.4.3 Uncertainty of Velocity Measurement

Similar to the salt mass fraction measurements, there are also sources of errors in velocity measurements. Equation (2.14) clearly shows the main source of error is coming from the uncertainty of fringe spacing, s . Also, the variation of the fresh water level during the measurements causes extra uncertainty of the laser beam crossing position. Both of these errors are estimated in the following section.

Uncertainty of the Fringe Space, s

Equation (2.13) indicates the fringe space, s , is a function of the angle between the two beams, α , and the beam wavelength, λ . As the beams pass through the interface between air and fresh water and the interface between fresh water and salt water, the angle between two beams changes according to the law of the refraction as shown in Eq. (2.20). On the other hand, the beam wavelength, λ , also changes when the laser beam travel from one medium to the other as

$$n_1 \lambda_1 = n_2 \lambda_2 . \quad (2.28)$$

where λ_1 and λ_2 are the beam wavelength in medium 1 and medium 2, respectively.

Substitution of Eq. (2.22) and Eq. (2.28) into Eq. (2.13) results in

$$s_1 = s_2 . \quad (2.29)$$

which indicates the fringe space will not be affected by the index of refraction changes between mediums. Thus the index of refraction effects on the velocity measurement is negligible.

Uncertainty of Fresh Water Surface

As discussed in 2.3.3, great effort has been taken to keep a steady fresh water surface in the test tank during the ceiling jet velocity measurement. However, it is impractical to exactly match the amount of injected salt water and drained fresh water. Thus, the water surface changed slowly during the measurement. Normally, the fresh water surface changes less than 0.5 mm in 3 hours. In the current study, the longest data acquisition period is 6 minutes. The maximum uncertainty of the water surface in one measurement is about ± 0.017 mm resulting in about ± 0.022 mm

uncertainty of the beam crossing position (this number corrected by the index of refraction of fresh water). Thus, the measurement point near the ceiling surface has a maximum uncertain about $\pm 8.3\%$ according to the short spatial step between two measuring points (0.26 mm). The water surface effects on the velocity measurements in free mixing region of the ceiling jet are negligible because the large spatial step (about 5 mm). Also the small velocity gradient in mixing region will allow more accurate velocity measurements.

Chapter 3: Results and Analysis

3.1 Validation of the Quantitative Salt-water Modeling Technique

The objective of this research is to establish a quantitative salt-water modeling technique to characterize fire induced flow dynamics. The salt-water experiments are first conducted in a canonical unconfined plume geometry to ensure that this technique is implemented properly. The unconfined plume is selected as the validation configuration for the quantitative salt-water modeling technique because it is a classical fire scenario and has been well studied for decades. Previous researchers have presented theoretical solutions of the plume characteristics in this fire configuration and extensive experimental data in actual fires for comparison. These previous studies provide a large body of data to validate the salt-water modeling measurements and the associated scaling theory [12, 15-17].

Salt-water modeling studies [3-6] have already demonstrated their ability to capture the qualitative behavior of fire-induced flows, e.g. plume dispersion dynamics, smoke movement and smoke layer growth. Flow visualization images of salt-water plumes are valuable for understanding the dispersion dynamics and mixing patterns in real fire plumes. Examples of quantitative instantaneous images for Case 1 are provided in Fig. 3.1. The dimensionless density difference, θ , represents $\beta_{sw} Y_{salt}$ for the salt-water plume and $\beta_T \Delta T$ for the fire plume. The PLIF salt-water images in Fig. 3.1 are inverted for easy comparison with the real fire plumes. If there is no special indication, the PLIF salt-water images presented in this study are inverted (e.g. body force, $f_3 = g$).

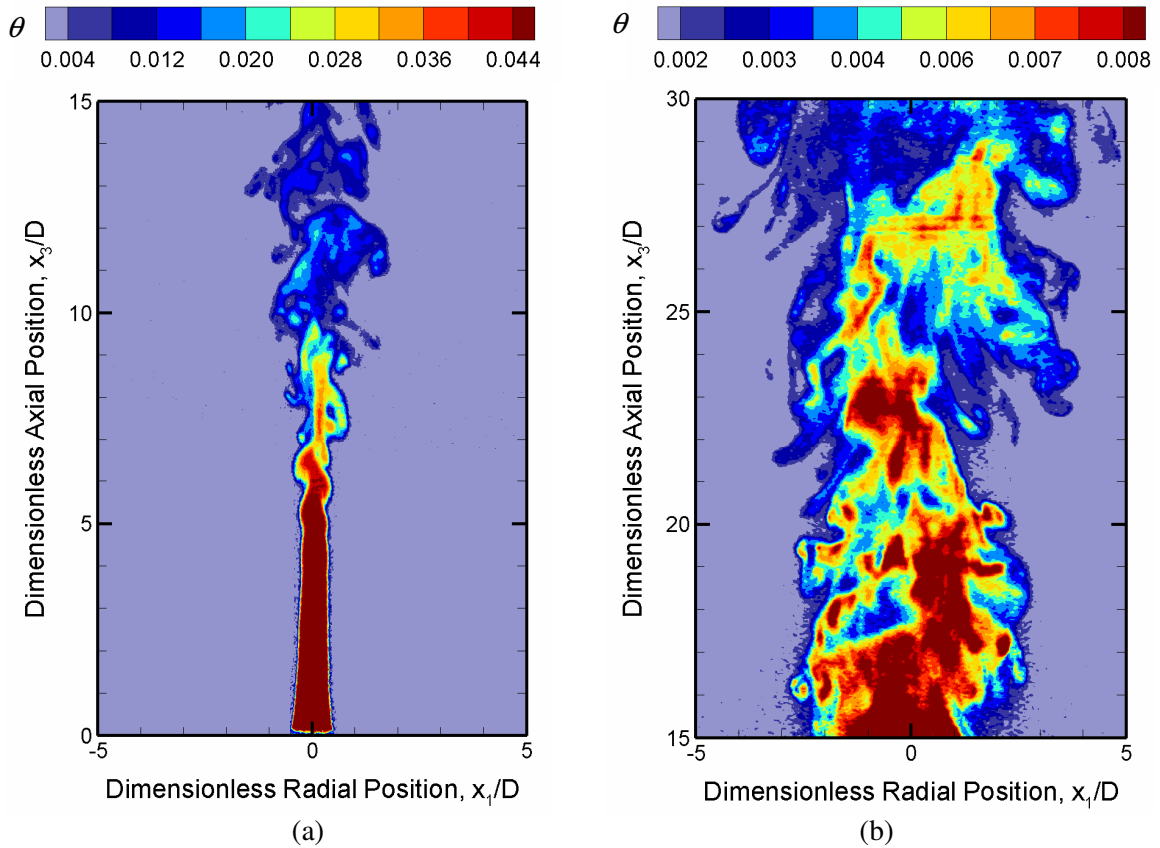


Figure 3.1 Visualization of the dimensionless density difference θ of an unconfined salt-water plume for Case 1; (a) near field; (b) far field

The plume dynamics where the plume transitions from laminar flow to turbulent flow are clearly observed in Fig. 3.1(a). Although these plumes are turbulent, the initial states of the plumes are laminar. For examples, the Reynolds number in Case 1 is only $Re_D = 434$. The buckling of the plume and associated vortex structure responsible for entrainment and dispersion is also apparent in the instantaneous images, which are consistent with expectations from a real fire [8]. The visualization of the instantaneous images also shows how fresh water is entrained into the plume and mixed with the salt water. The ambient fresh water penetrates into the salt-water plume by entrainment and dilutes the salt water concentration along the

flow path. The turbulent vortex structure is larger in the far field area than that in the region near the injector. The vortices continue to grow as the flow convects from the source. The fact that images in Fig. 3.1 also provide quantitative distribution information of θ should be emphasized. The quantitative measurements of θ from PLIF salt-water images are compared with actual fire data, theory and thermal plume data to validate the quantitative salt-water modeling technique.

3.1.1 PLIF Salt-Water Modeling Validation

Measurements in the unconfined salt-water plumes are first compared with point-source plume theory to validate the implementation of the PLIF salt-water modeling technique. Measurements are made at specific buoyancy fluxes of $B = 1.62 \times 10^{-6} \text{ m}^4/\text{s}^3$ and $B = 2.43 \times 10^{-6} \text{ m}^4/\text{s}^3$ corresponding to the unconfined plume Case 1 and Case 2, respectively. Since in the unconfined plume configuration, there is no well established character length scale. Thus specific buoyancy fluxes are used to describe the initial flow condition instead of the most popular parameter Q^* . These initial flow conditions provide a buoyancy dominated condition not far from the injector exit (e.g. $L_M \sim D$), yielding a substantial buoyant plume field for analysis. Experiments at two different buoyancy fluxes are conducted in this study in order to validate the scaling theory.

It is well known that the centerline mean dimensionless density difference $\bar{\theta}_c$ of the fire plume obeys the (-5/3) power law decay based on point source theory. Figure 3.2(a) shows an excellent agreement between centerline dimensionless density difference taken from the salt-water plume measurements, real fire data and point

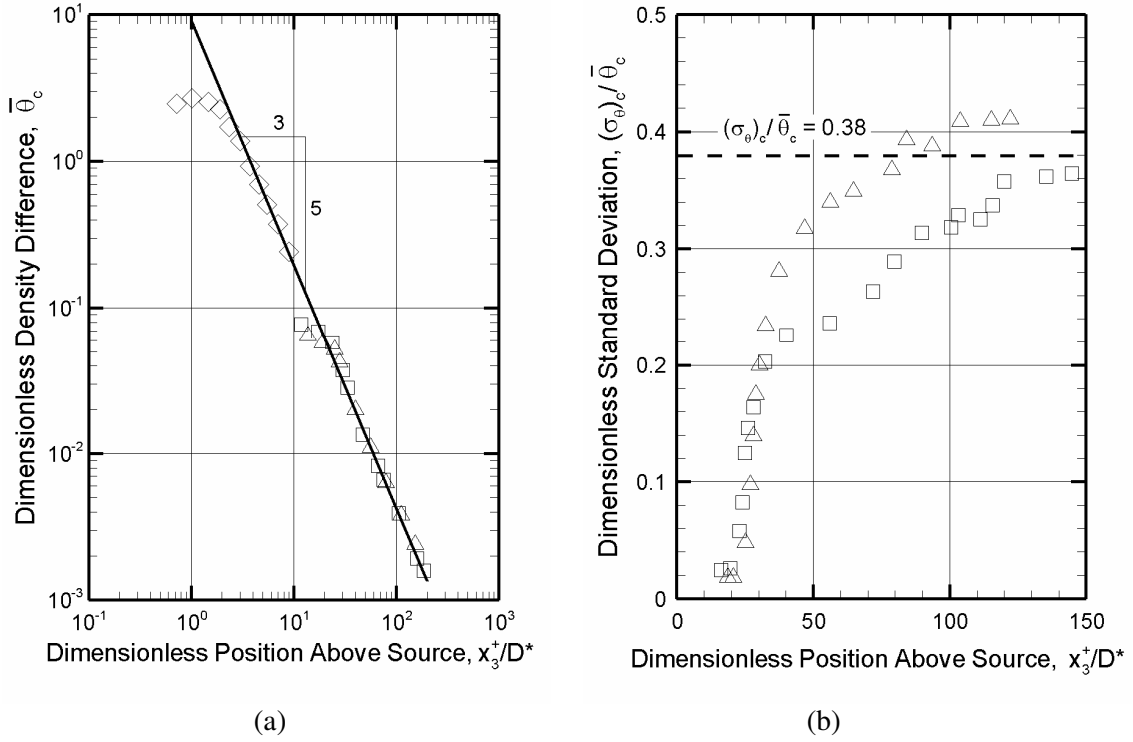


Figure 3.2 Dimensionless density difference distribution along plume centerline; (a) mean profile, $\bar{\theta}_c$ (b) dimensionless standard deviation, $(\sigma_\theta)_c/\bar{\theta}_c$; \diamond McCaffrey's plume [13]; salt water model \triangle Case 1; \square Case 2; — Theory [14]

source plume theory. The position above the source is normalized by a source based

length scale D^* , where $D_{sw}^* = \left(\frac{\beta_{sw}\dot{m}_{salt}}{\rho_0 g}\right)^{2/5}$ for salt water and $D_T^* = \left(\frac{\beta_T\dot{Q}}{\rho_0 c_p g}\right)^{2/5}$ for

fire. McCaffrey's plume measurements provided in Figure 3.2(a) also show the relative strength of the salt-water plume compared to fire plumes [13]. The

dimensionless density difference, $\theta_{sw} = \beta_{sw}Y_{salt}$, for salt water is much smaller than

$\theta_T = \beta_T\Delta T$ for fire, indicating the salt-water plumes are relatively weak compared to

fire plumes. The virtual origins of the salt-water plumes based on the scalar measurements are $z_0 = -11.8$ mm and $z_0 = -18.5$ mm for Case 1 and Case 2,

respectively. The virtual origin of McCaffrey's experiments is $z_0 = -89.7$ mm. The virtual origin, z_0 , is calculated by the method of Heskestad [10].

As discussed previously, the salt water mixture is first introduced into the fresh water as a near momentum driven jet. The initial momentum decreases along the flow path and the plume transitions to a buoyancy dominated turbulent flow. Figure 3.2(b) shows the fluctuations of the centerline dimensionless density difference, $(\sigma_\theta)_c / \bar{\theta}_c$, along the position above the source. The turbulent fluctuations increase with increasing elevation. Finally the flow attains a fully developed turbulent condition, where it reaches a standard deviation of about 41 % of the mean value at the centerline. This number agrees well with previous published researchers' results. Shabbir and George's [2] correlation predicts a fluctuation of about 38% at the fully developed turbulent condition. While Nakagome and Hirata [52] and Kotsovinos' [53] found this number to be 43% and 44%, respectively. The good agreement of turbulent fluctuation measurements between salt-water experiments and fire experiments also demonstrate the ability of using the salt-water modeling technique to study the turbulent characteristics in fire induced flows. Despite the weakness of the salt-water plumes relative to actual fire plumes, the decay of the dimensionless density difference obeys the familiar $(-5/3)$ power law obtained from turbulent point source plume theory.

3.1.2 LDV Salt-Water Modeling Validation

In this study, the centerline velocity profile in the unconfined salt-water plume is measured by using Laser Doppler Velocimetry (LDV). The centerline velocity is

also compared with point source theory to validate the quantitative LDV salt-water modeling technique. Measurements are made at specific buoyancy fluxes of $B = 1.62 \times 10^{-6} \text{ m}^4/\text{s}^3$ and $B = 1.27 \times 10^{-6} \text{ m}^4/\text{s}^3$ corresponding to Case 1 and Case 3, respectively. Similar to the PLIF measurements, two different buoyancy sources are applied in the LDV experiments to validate the scaling theory. The index of refraction differences between salt water and fresh water will result in bending of the laser beam making LDV measurement difficult. Turbulent fluctuations in concentration and associated index of refraction can cause uncontrolled beams steering preventing the beam crossing required for LDV measurements. This problem completely prevents measurements in the turbulent transition region in the near-field where concentration gradients are steep and in the impingement region where long laser beam path lengths are unavoidable.

Figure 3.3(a) shows excellent agreement between the data taken from the LDV measurements and point source plume theory. Similar to the PLIF salt-water measurements, McCaffrey's plume velocity measurements are also plotted here to emphasize the relative strength of salt-water plumes compared to fire plumes [8]. The dimensionless velocity in salt-water plume is much smaller than that in the real fire plumes, which also demonstrates that the salt water simulates a weak plume. The virtual origins of the salt-water plumes based on the centerline velocity measurements are $z_0 = 53.6 \text{ cm}$ for case 1 and $z_0 = 77.5 \text{ cm}$ for Case 3 correspondingly. The velocity based virtual origin of McCaffrey's experiments is $z_0 = 298 \text{ mm}$. Please note that the virtual origins based on velocity are different from previous values based on

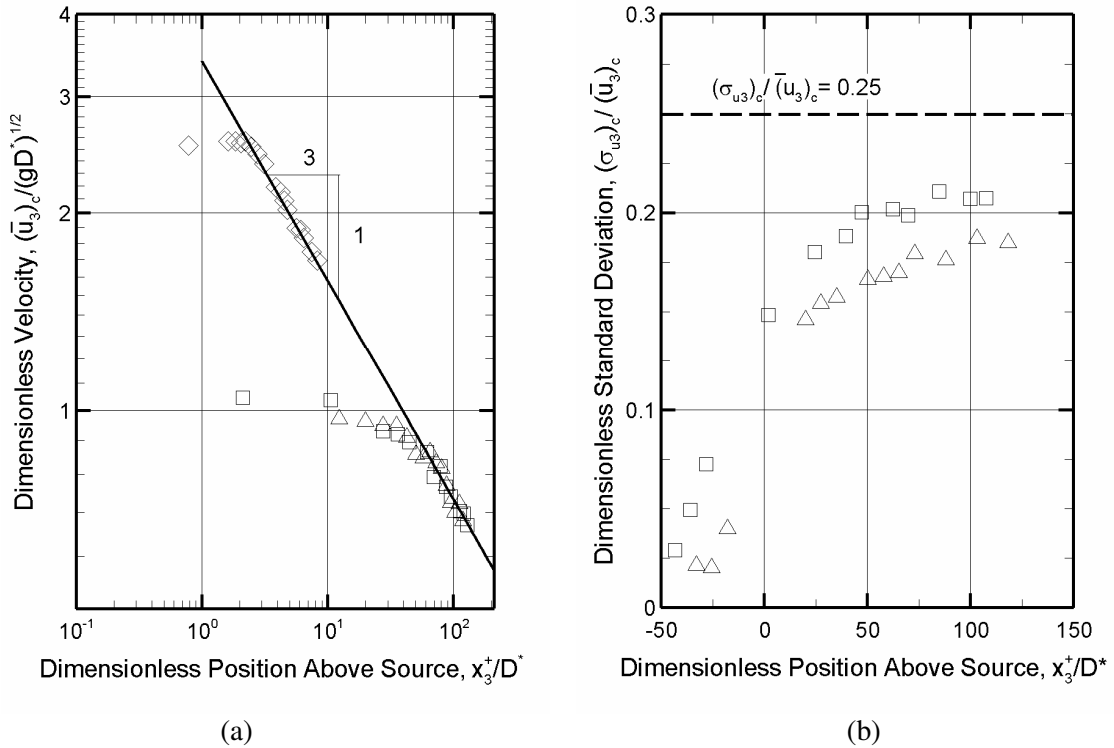


Figure 3.3 Dimensionless velocity distribution along plume centerline; (a) mean profile, $(\bar{u}_3)_c$ (b) dimensionless standard deviation, $(\sigma_{u_3})_c / (\bar{u}_3)_c$; \diamond McCaffrey's plume [13]; salt water model \triangle Case 1; \square Case 3; — Theory [14]

dimensionless density difference. The virtual origin is used to correlate data in terms of point source plume theory and will depend on the flow quantity measured.

Fig. 3.3(b) plots the dimensionless turbulent intensity of the vertical velocity, $(\sigma_{u_3})_c / (\bar{u}_3)_c$, along the plume centerline. The fluctuation intensity of $(\sigma_{u_3})_c / (\bar{u}_3)_c$ shows a similar trend to the one observed for the $(\sigma_\theta)_c / \bar{\theta}_c$ in PLIF measurements. It also shows the transition from laminar flow to turbulent flow. It also reaches fully developed turbulent condition when $x_3^+ / D^* > 100$, where $(\sigma_{u_3})_c / (\bar{u}_3)_c$ has a peak turbulent intensity of 21%. This number is close to Papanicolaou et al.'s [54] value 25%. It is smaller than Shabbir and George's [2] correlation prediction 32% and George's [55] measurement of 28%. The agreement of velocity measurements, fire

data and point source theory also proves the ability of using salt-water modeling to study fire induced flows.

3.2 Impinging Plume Dynamics

Characterizing the ceiling jet formed by a fire induced buoyant plume is critical because most fire detection and suppression devices are designed to operate within this flow. Although many investigators have studied fire induced ceiling jets, detailed measurements of velocity and temperature have not been obtained to date. This study seeks to provide a detailed and comprehensive characterization of the impinging plume using salt-water modeling.

Three regions have been identified in the impinging plume configuration: plume region, turning region and ceiling jet region (refer to Fig. 1.1). The flow behavior is quite different in these regions. The flow dynamics in the plume region of the impinging plume configuration is the same as that in the unconfined plume configuration. The point source theory predicts the flow behavior very well. However, the flow dynamics in the turning region are more complicated. Due to the interaction with the wall, the centerline characteristics of the plume deviate from point source theory. At the exit of the turning region, the vertical rising plume is changed to a radially expanding ceiling jet along the ceiling surface. Detailed characteristics in these three regions will be discussed in the following sections separately.

3.2.1 Characterization of the Plume Region

In the impinging plume configuration, the PLIF salt-water measurements are plotted in terms of the source independent dimensionless density difference θ^* , where $\theta_{sw}^* = \theta_{sw} (m_{salt}^*)^{-2/3}$ in the salt-water plume and $\theta_T^* = \theta_T (Q^*)^{-2/3}$ in fire induced flows as discussed in §2.1. The dimensionless source strength is defined based on the ceiling height above the virtual source, H , where $m_{salt}^* = \frac{\beta_{sw} \dot{m}_{salt}}{\rho_0 g^{1/2} H^{5/2}}$ for salt water modeling and $Q^* = \frac{\beta_T \dot{Q}}{\rho_0 c_p g^{1/2} H^{5/2}}$ for fire. One advantage of using θ^* in the analysis is that the measurements in salt-water flows can be directly compared with those in fire induced flows. Since θ^* is source independent, the salt-water experiment results can be used to explore the characteristics of fire plumes with any fire source strength. For the purpose of illustration, a concentration based salt-water measurement is converted to a temperature in the fire configuration. For example, a source independent parameter is measured as $\theta_{sw}^* = 18$ at $(x_1/H = 0, x_3/H = 0.8)$ in the salt-water flow field. In a real fire case, assuming a compartment ceiling height $H = 3$ m (virtual origin z_0 is considered as 0 here to make the analysis simple), ambient air temperature $T_0 = 298$ K, and ambient air density $\rho_0 = 1.26$ kg/m³, the fire plume temperature rise, ΔT , at the corresponding position with a fire source having $\dot{Q} = 10$ kW can be calculated from

$$\theta_T = \beta_T \Delta T = \theta_{sw}^* (Q^*)^{2/3} = \theta_{sw}^* \left(\frac{\beta_T \dot{Q}}{\rho_0 c_p g^{1/2} H^{5/2}} \right)^{2/3}. \quad (3.1)$$

The dimensionless density difference in the real fire is $\theta_r = 0.12$ corresponding to a temperature increase of 36 K at $(x_1/H = 0, x_3/H = 0.8)$. A similar approach can also be used for converting salt-water velocity measurement to corresponding values in the fire configuration.

The salt-water plume behaves like an unconfined plume before it reaches the ceiling. After some vertical distance, the plume characteristics in the plume region obey point source plume theory. The quantitative PLIF salt-water modeling measurements provide a detailed spatial distribution of the dimensionless density difference θ . This detailed information is very useful for understanding turbulent mixing patterns. The phenomena of flow transitions from laminar flow to turbulent flow, entrainment and turbulent structure development in the salt-water plume have been clearly captured in the instantaneous images provided in Fig. 3.1. The following discussion provides quantitative characterization of the phenomena in the plume region.

Figure 3.4 plots the mean density difference, $\bar{\theta}_c$, and the mean velocity, $(\bar{u}_3)_c$, distributions along the plume centerline for Case 1. The dimensionless fluctuations of each quantity (i.e. $\bar{\theta}_c$, $(\bar{u}_3)_c$) are also plotted to show the turbulent development of the flow. Although the impinging plume configuration has well defined length scale H , this length scale is not appropriate in the plume region (not close to the ceiling). In this region, the injection diameter D or the source based length scale D^* should be used. Figure 3.4(a) shows $\bar{\theta}_c$ decays very quickly near the injection location. At $10D$ downstream of the flow, the dimensionless density difference $\bar{\theta}_c$ is less than

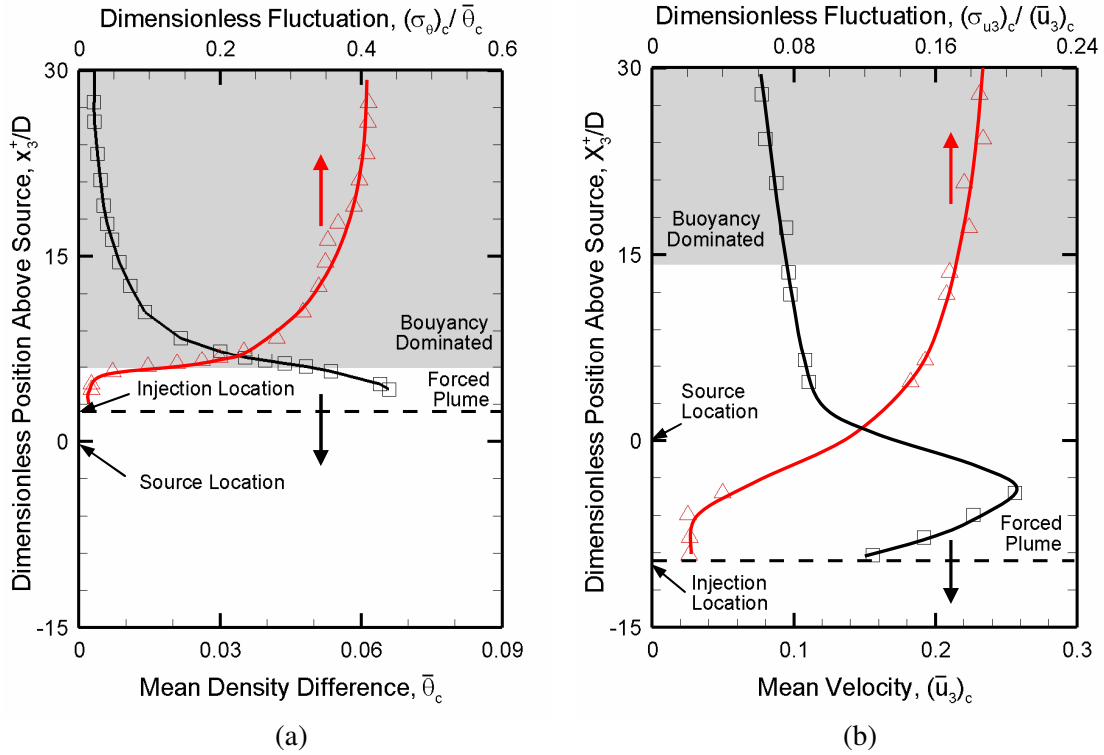


Figure 3.4: The centerline dimensionless mean characteristic and related fluctuation of the unconfined salt-water plume Case 1; (a) dimensionless density difference, $\bar{\theta}_c$ (b) velocity, $(\bar{u}_3)_c$; \square mean value; Δ dimensionless fluctuation

25% of the initial value. This fast decrease of $\bar{\theta}_c$ can be explained by the quickly increasing turbulent fluctuations, which enhances the mixing between salt water and ambient fresh water. Figure 3.4(b) shows the centerline mean velocity $(\bar{u}_3)_c$ first increases and then decreases after a certain distance. The acceleration of $(\bar{u}_3)_c$ is caused by the buoyancy force. It is also interesting to note that the diameter of the salt-water jet is shrinking according to mass conservation, which can be observed in the previously presented instantaneous image Fig. 3.1(a). After the flow acceleration region, the velocity of the salt-water jet decreases by entraining quiescent ambient fresh water into the flow. The virtual source position $x_3^+ = 0$ and the corresponding

buoyancy dominated region are also indicated in Fig. 3.4. The dimensionless density difference field shows buoyancy dominated characteristics near the injection location at $x_3^+/D = 6$, while the velocity field becomes buoyancy dominated at a much longer distance, $x_3^+/D = 14$. Since the Morton length scale is about $1D$ in Case 1 as shown in Table 4.1, the $5L_M$ guidance on the starting point of the buoyancy dominated region is not applicable to the velocity field. This limitation was not originally noted because velocity measurements were not available when the recommendation was established. Figure 3.4 also illustrates the difference in the virtual origin based on θ and u_3 measurements. The virtual source location is below the injection location for θ measurements, but above the injection location for u_3 measurements.

More information about impinging plume dynamics in the plume region can be obtained from evaluating the mean and standard deviation images in Case 1 provided in Fig. 3.5. It should be noted that the color map of the standard deviation image is 1/4 scale of that in the corresponding average image. The cross stream profiles of $\bar{\theta}^*$ and σ_{θ^*} are also plotted in Fig. 3.5 at locations of $x_3^+/D = 15, 20$ and 25 to further illustrate the flow dynamics. Two instant profiles for each position are plotted using red lines ($t = 100$ s) and white lines ($t = 200$ s). The plume width is also plotted in Fig. 3.5(a) using dashed lines. The plume width, b , is defined as the position of $\bar{\theta}^* / \bar{\theta}_c^* = e^{-1}$.

Figure 3.5(a) illustrates a symmetric spatial distribution of the mean dimensionless density difference $\bar{\theta}^*$. The mean radial profiles of $\bar{\theta}^*$ are quite Gaussian at $x_3^+/D = 15, 20$ and 25 ; however, instantaneous realizations appear as denticulate top-hats with associated large gradients at the edges. This observation is

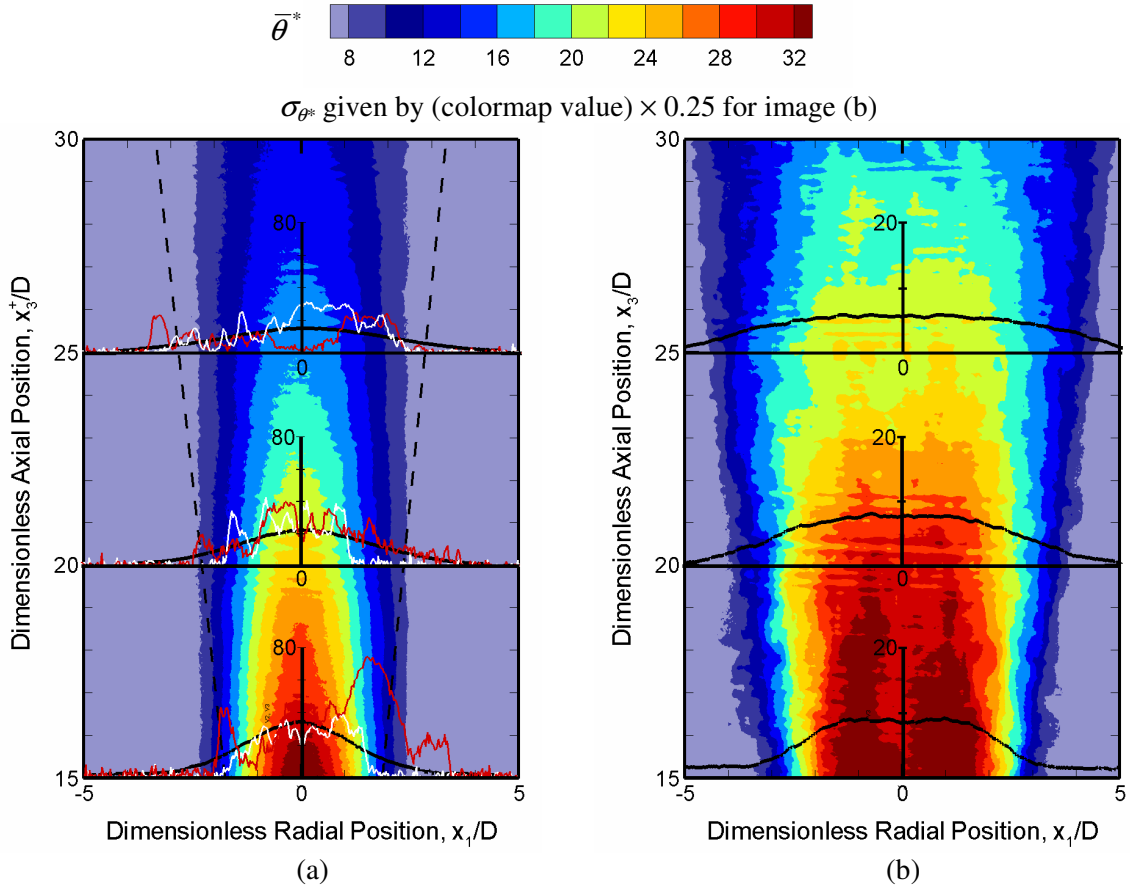


Figure 3.5: Visualization of the dimensionless density difference of an unconfined salt-water plume in far field; (a) mean value $\bar{\theta}^*$, ----- plume width, b ; ——— $\bar{\theta}^*$ profile (b) standard deviation σ_{θ^*} , ——— $\bar{\sigma}_{\theta^*}$ profile

consistent with Zukoski's postulate that the mean Gaussian profile is realized from turbulent top-hat behavior [9]. The instantaneous radial profiles clearly show although the mean value of θ^* is very small, the instant value can be much higher. Figure 3.5(a) also illustrates the plume width increases linearly along the distance from the plume source. Based on point source theory, there is a linear relationship between plume width, b , and entrainment constant, α , as shown in Eq. (1.3). The entrainment constant, α , measured from the salt-water experiments equals 0.099 (assuming $\beta = 0.956$ [14]) which agrees well with previous values of 0.10 suggested by Alpert [12] and 0.11 by Zukoski [14]. The radial profiles of the standard deviation

at three locations show off-axis peak values in figure 3.5(b). The peak standard deviation occurs in the mixing and entrainment region near the plume boundary at locations near the source. This mixing region grows and merges at the centerline at downstream locations. Although the standard deviation, σ_{θ^*} , decreases along the plume streamwise direction, the magnitude of the fluctuation intensity $\sigma_{\theta^*}/\bar{\theta}^*$ continues increasing with the turbulent development until fully developed conditions are achieved, as shown in Fig. 3.4(a).

More insight into the flow dynamics is observed by analyzing the time based probability density function of the source independent density difference, $p_t(\theta^*)$, which is defined as

$$p_t(\theta^*) = \lim_{\theta_1^* \rightarrow \theta_2^*} \frac{\text{prob}(\theta_1^* \leq \theta^*(t) < \theta_2^*)}{\theta_2^* - \theta_1^*} \quad (3.3)$$

Pdfs of θ^* at selected streamwise and spanwise locations are provided in Fig. 3.6. The streamwise positions are the same as those shown in Fig. 3.5 (i.e. $x_3^+/D = 15, 20$ and 25). At each elevation, the center of the plume ($x_1/b = 0$), and positions near the middle of the plume ($x_1/b = 0.5$) and edge of the plume ($x_1/b = 1$) are selected. The spatial area of the Pdfs is $135 \mu\text{m} \times 135 \mu\text{m}$ in the thickness of the laser sheet. This spatial area is larger than the Kolmogorov length scale at these locations (e.g. $\lambda_T \sim 100 \mu\text{m}$ at $x_3^+/D = 20$). Thus these measurements don't resolve the smallest scale of the turbulent mixing and the resulting Pdfs filter out some of the high frequently information. However, information can still be obtained from these Pdfs for understanding the flow mixing characteristics at these locations. A few general observations can be made from this set of Pdfs. The centerline Pdfs show the fresh-

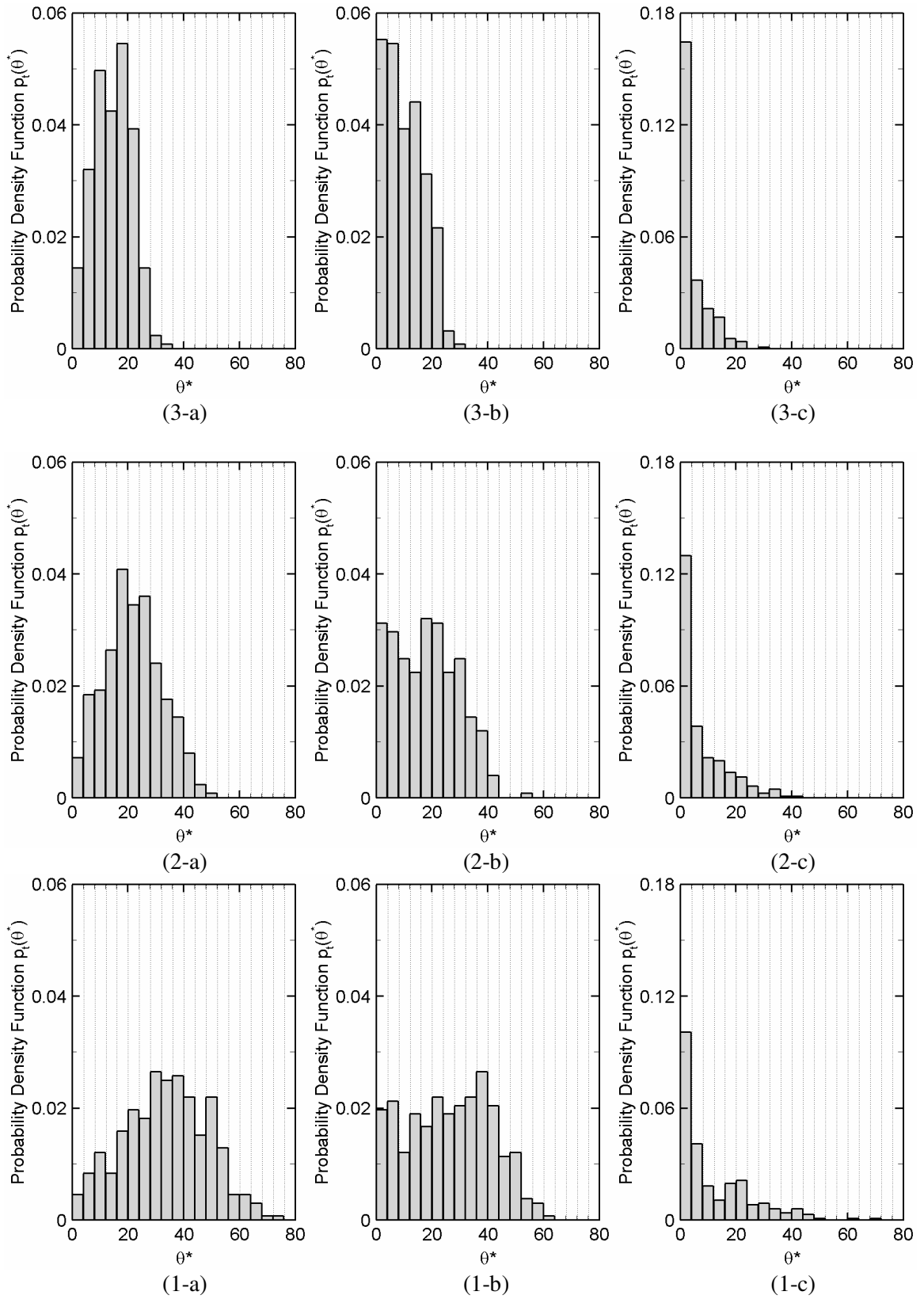


Figure 3.6: Probability Density Function $p_t(\theta^*)$ at axial positions (1-) $x_3^+/D = 15$; (2-) $x_3^+/D = 20$; (3-) $x_3^+/D = 25$; (a) plume center ($x_1/b = 0$); (b) plume middle ($x_1/b = 1/2$); (c) plume edge ($x_1/b = 1.0$)

water penetrations to the centerline at all of the elevations, providing quantitative data consistent with the significant unmixedness and large scale turbulence observed in the instantaneous images. This behavior is also reflected in the Pdfs near the plume edge, which, although infrequent, have occurrence of mass concentrations near peak centerline value. Double peak behavior is observed in the mid-plume region suggesting strong fluctuations and weak mixing between the salt-water plume and the entrained fresh water. This double peak behavior is best observed in Fig. 3.2(b).

3.2.2 Characterization of the Turning Region

In the turning region, the flow is affected by the presence of the ceiling. At the beginning of the turning region, the mean velocity of the flow is primarily perpendicular to the ceiling surface. Then it turns and follows the ceiling eventually creating a wall jet. The heat transfer rate is greatest at the stagnation point because the turbulence intensity of the impinging plume has a local maximum at the stagnation point [45, 46]. Then the Nusselt number monotonically decreases from its maximum at the stagnation point with the decrease of ceiling jet velocity and expansion of the ceiling jet layer. The flow dynamics in the turning region has a variety of engineering applications including enhanced heating or cooling. In this study, the flow dynamics and ceiling effects on the mixing process in the turning region are characterized via the quantitative images recorded in the PLIF salt-water measurements. Unfortunately, no velocity measurements were obtained due to beam steering problems in this region associated with index of refraction gradients and the unavoidable long laser beam path lengths.

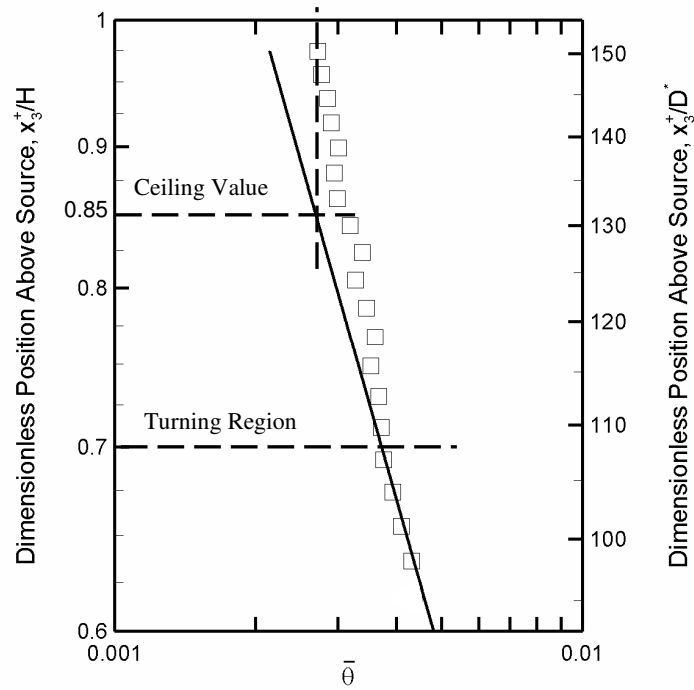


Figure 3.7: Centerline mean density difference of impinging plume, $\bar{\theta}_c$; \square impinging plume Case 4; — unconfined plume theory

Once the flow approaches the ceiling surface, the flow characteristics deviate from point source theory. A comparison of the centerline dimensionless density difference $\bar{\theta}_c$ between the point source theory and the salt-water impinging plume measurements is provided in Fig. 3.7. As expected, the deviation from point source theory (i.e. unconfined plume) is clearly observed as the ceiling is approached. The turning region is considered to start at the point where deviation occurs between the point source theory and the measurements. The turning region starting point has been previously established as $0.85H$ [12]. The salt-water measurements indicate the turning region starts at $0.70H$ which is earlier than previous predictions. The gradients of $\bar{\theta}_c$ in the turning region are very small because the flow is well mixed indicated by the near vertical profile of $\bar{\theta}_c$ from $0.7 \leq x_3^+/H \leq 1.0$. In the current

study, $(\bar{\theta}_c)_p$ at the stagnation point is close to the value at $0.85H$ in the unconfined plume configuration. Correspondingly, the source independent density difference, $(\bar{\theta}_c^*)_p$, is about 11.7. This criterion will be applied in the adiabatic wall heat transfer model in Chapter 4 to predict the stagnation point temperature.

The gross flow features of the impinging plume and resulting ceiling jet are easily observed in the average and standard deviation images of the source independent dimensionless density difference θ^* for Case 4, as shown in Fig. 3.8(a). The specific dimensionless source strength is $m_{sw}^* = 3.74 \times 10^{-6}$ with a characteristic Grashof number $Gr_H = 8.45 \times 10^{10}$ in this impinging plume configuration. Due to the limitation of the camera resolution and the edge effect at the ceiling surface, the nearest data position from the ceiling is about $0.005H$. The radial profiles of the mean dimensionless density difference at $x_3^+/H = 0.70$ and $x_1/H = 0.20$ are also plotted in Fig. 3.8(a). These two locations have important meanings to the plume turning region. The position at $x_3^+/H = 0.70$ is considered as the starting plane of plume turning region while the position at $x_1/H = 0.2$ is the exit of the plume turning region [12, 16]. The distribution of $\bar{\theta}^*$ along these starting and exit planes has a similar profile (Gaussian in plume and half Gaussian in the ceiling layer). The peak value of $\bar{\theta}^*$ in the ceiling layer occurs at the wall as that has been suggested by other investigators [16]. This phenomenon agrees well with the statement that the salt-water modeling experimental configuration is comparable to the adiabatic wall boundary condition in the real fire case. As shown in Fig. 3.8(a), the standard deviation, σ_{θ^*} , has an off-axis peak at the beginning of the turning region. This off-

axis peak σ_{θ^*} is diminished when the flow approaches the ceiling. Similarly, the peak of σ_{θ^*} occurs at the location about $0.02H$ away from the ceiling in the ceiling jet region. The quantitative salt-water measurements also indicate the turbulent intensity, $\sigma_{\theta^*}/\bar{\theta}^*$, along the plume centerline is almost constant in the plume turning region. At the exit of the turning region, $\sigma_{\theta^*}/\bar{\theta}^*$ in the boundary layer is very close to the value at the plume centerline in the turning region.

Furthermore the instantaneous impinging plume shown in Fig. 3.8(b) provides a substantially different view of the flow when compared with the corresponding mean image. The turbulent structure of the salt-water flow and its interaction with the ceiling is clearly evident in this instantaneous image. The presence of the boundary and its effect in dissipating large eddies should result in a well-mixed region. Since the turbulence is already fully developed before it impinges on the ceiling, the turbulence may persist in the ceiling jet even at a relatively low Grashof number, $Gr_H = 8.45 \times 10^{10}$ (or $Re_H = 4389$). In fact in certain regions, ambient fluid appears to penetrate all the way to the surface as shown in the instantaneous image (e.g. at the position of $x_1/H = -0.2$ along the ceiling).

Pdfs at three typical locations in the turning region have been presented in Fig. 3.9 to show the flow mixing characteristics qualitatively. These three locations are selected at near the stagnation point ($x_1/H = 0.02$, $x_3^+/H = 0.98$), the middle of the turning region ($x_1/H = 0.075$, $x_3^+/H = 0.95$) and the edge of the turning region ($x_1/H = 0.15$, $x_3^+/H = 0.90$). The spatial area of the Pdfs is $150 \mu\text{m} \times 150 \mu\text{m}$ in the thickness of the laser sheet which is similar to the area used in §3.2.1. Although these Pdfs are not able to resolve the smallest turbulent scale, they are still useful in revealing the

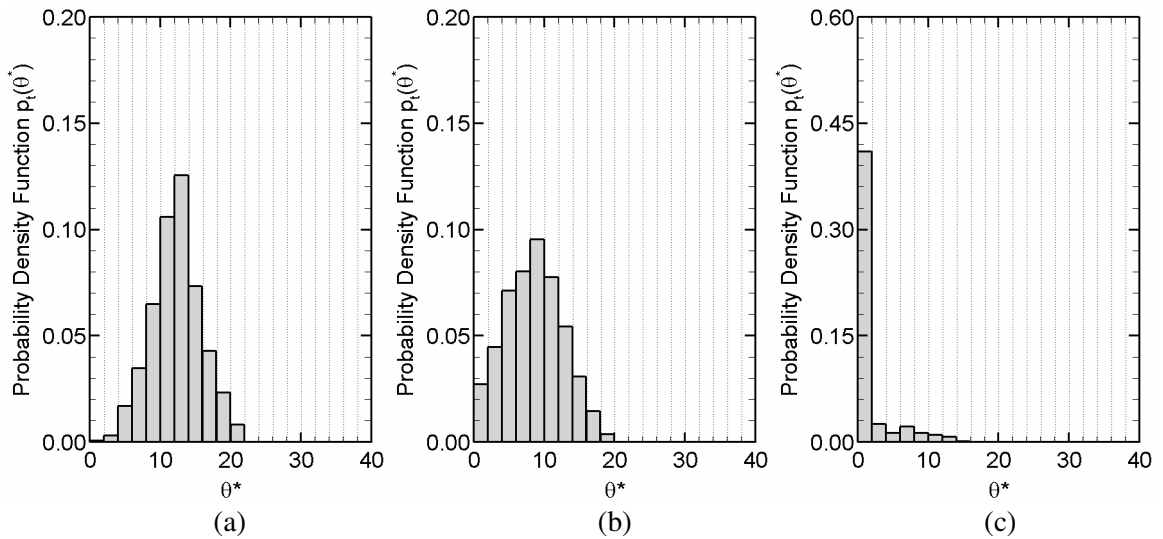


Figure 3.9: Probability Density Function $p_i(\theta^*)$ at turning region for Case 4 (a) near stagnation point ($x_1/H = 0.02, x_3^+/H = 0.98$); (b) middle location ($x_1/H = 0.075, x_3^+/H = 0.95$); (c) edge of the stagnation region ($x_1/H = 0.15, x_3^+/H = 0.90$)

turbulent mixing behavior at these locations. Intense mixing occurs in the turning region. In contrast to the plume region behavior described in Fig. 3.6, fresh water doesn't penetrate to the center location (stagnation point). In the middle of turning region, a single peak Gaussian shaped Pdf is also observed indicating intense mixing as the wall is approached. This should be contrasted with the double peaked Pdfs in the plume region. At the edge of the plume, relatively high concentration fluid intermittently also appears but not as high as that occurring on the centerline.

Quantitative analysis of the flow characteristics in the turning region using salt-water measurements also provides a criterion on the minimum ceiling height required for a valid scaling law in small scale salt-water experiments. As discussed before, the key factor in determining the validity of fire/salt-water analogy is whether the differences in Gr , Pr and Sc numbers between salt-water flows and fire induced flows can be neglected or not. It is well known that in a turbulent flow, the mixing

behavior is controlled by the turbulence and the molecular diffusion effect plays a secondary role in transport. Furthermore, the molecular diffusion effects in water plumes are even more trivial due to large Sc number (about 640 for water) which increases the fidelity of the fire/salt-water analogy. Thus the turning region starting point will provide guidance on the recommended ceiling heights used in small scale salt-water experiments: the ceiling should be high enough for the flow to reach fully developed turbulent condition before it enters the turning region. Bejan [47] predicted the turbulent transition starts when Grashof number, Gr , is larger than 2×10^{10} . Furthermore, current salt-water experiments indicate the flow reaches a fully developed turbulent state when the Gr is larger than 3.85×10^{10} at $x^+_3/D^* > 100$ (refer to Figs. 3.2(b) and Fig. 3.3(b)). Thus the critical ceiling height, H_{cr} , is determined based on the fully turbulent Grashof number, Gr_t , where $H_{cr} = (Gr_t \rho_0 v^3 / g \beta_{sw} \dot{m}_{salt})^{0.5}$ for salt-water flow and $H_{cr} = (Gr_t \rho_0 c_p v^3 / g \beta_T \dot{Q})^{0.5}$ for fire induced flow. Since the turning region starts at $0.70H$ as shown in Fig. 3.7, the ceiling height for the salt-water modelling should satisfy $0.70H/H_{cr} > 1$. In fire experiments, it is much easier for the flow to reach a fully turbulent state. An additional criterion, $H_f/H \ll 1$, is needed to define a relatively small fire for a valid small scale experiment.

3.2.3 Characterization of the Ceiling Jet Region

Once the plume exits the turning region, it behaves as a ceiling jet. Wall-jet studies of Glauert [56] and Poreh, et al. [57] have established the ceiling jet to be a boundary-layer type flow. The key parameters that define the behavior of the ceiling

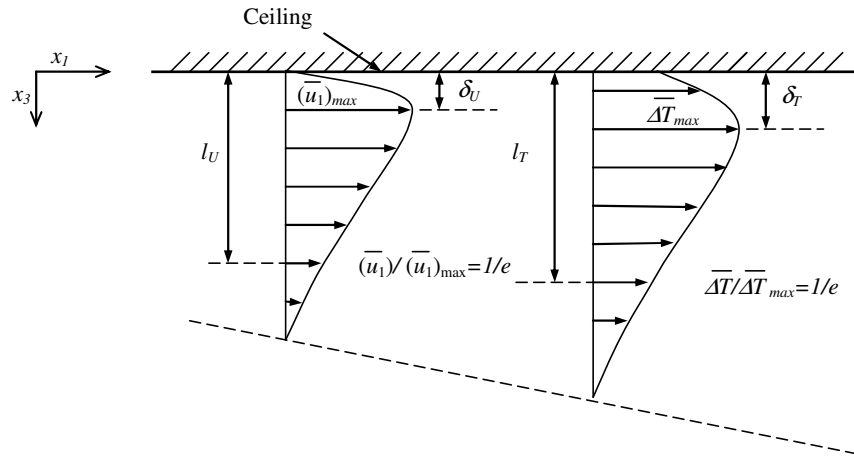


Figure 3.10: Schematic of the ceiling jet and its characteristic parameters

jet as a function of position under steady-state conditions can be identified according to Fig. 3.10. The ceiling jet momentum and thermal boundary layer thickness are denoted as δ_U and δ_T , respectively. These two quantities identify a region of the jet where flow velocity and temperature vary from the wall no-slip conditions to maximum values, $(\bar{u}_1)_{\max}$ and $\overline{\Delta T}_{\max}$. At distances beyond δ , the ceiling jet flow behaves like a free jet and its growth is defined by thermal and momentum thicknesses, l_T and l_U , respectively. The thermal thickness l_T is the position where $\overline{\Delta T} / \overline{\Delta T}_{\max} = 1/e$ and momentum thickness l_U is the position where $\bar{u}_1 / (\bar{u}_1)_{\max} = 1/e$.

Previous researchers have produced correlations for the ceiling jet maximum velocity and temperature. Alpert [12] assumed half Gaussian behavior for the velocity and temperature profiles and developed an integral model for the boundary layer thickness and other ceiling jet quantities. Alpert's integral model provides reasonable predictions on the temperature. However, the prediction of velocity from his model is inaccurate. This inaccuracy is caused by assuming the same thickness of

thermal and momentum boundary layers in his analysis. Motevalli [15] conducted temperature and velocity measurements inside the ceiling layer using thermocouple trees. His experimental results indicated that l_U and l_T are not equal. In a review paper, Beyler [1] compared a list of ceiling jet correlations. The comparisons demonstrate that the agreement between the empirical models of the maximum ceiling jet temperature and velocity is not always as good as desired. Furthermore, very limited ceiling jet velocity measurements have been obtained.

In this study, quantitative salt-water modeling explores the detailed characteristics of the ceiling jet created from the impinging plume. Observation of instantaneous images at different locations along the ceiling reveals a clear trend in the evolution of the turbulent structures that govern flow and thermal transport in the ceiling jet. Representative instantaneous images for Case 4 are provided at selected positions along the ceiling in Fig. 3.11. Upstream of the impingement region, fresh

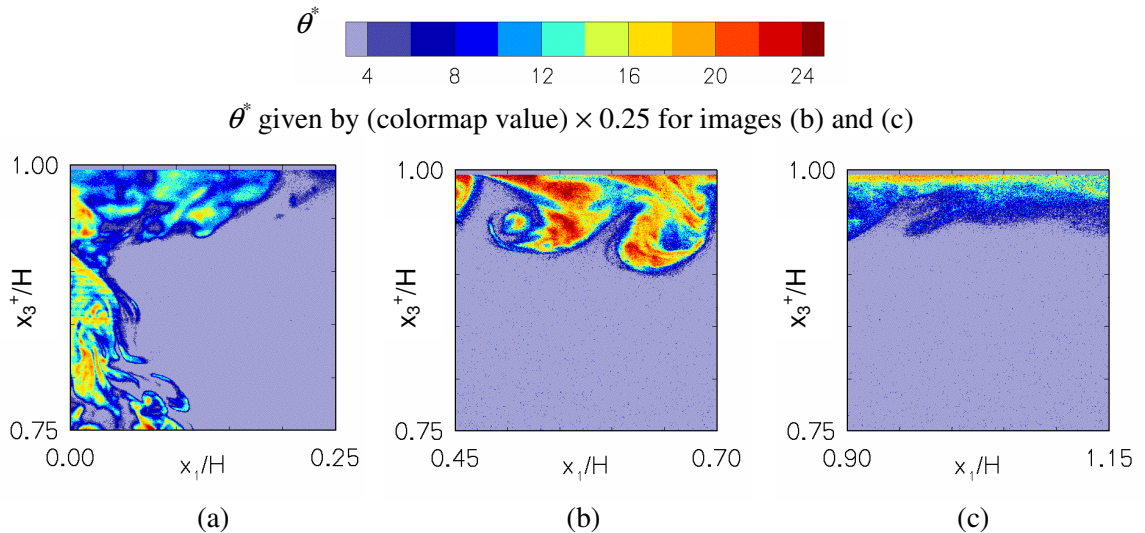


Figure 3.11: Turbulent structures and ceiling jet progression for Case 4; (a) impingement and turning region $0 < x_1/H < 0.25$; (b) ceiling jet region $0.45 < x_1/H < 0.7$; (c) ceiling jet region $0.9 < x_1/H < 1.15$.

water is entrained deep within the plume creating large-scale unmixed vortex structures characterized by sharp density interfaces. However, very near the ceiling, the sharp interfaces between the freshly entrained flow and the plume flow disappear even within the impingement region. The steep gradients introduced by the wall result in smaller length scales and associated smaller turbulent length scales, which act to remove these sharp interfaces.

The ceiling jet emerging from the turning region is turbulent, with a non-uniform small variation in density difference as shown in Fig. 3.11(a). Further along the ceiling in the vicinity of $x_1/H = 0.5$, the ceiling jet thickness grows with strong entrainment and turbulence. Figure 3.11(b) shows typical ceiling jet behavior downstream of the impingement region. Large scale turbulent motion is still observed along the ceiling jet occasionally penetrating to the wall (at $x_1/H = 0.47$) indicating that entrainment is important. Even further along the ceiling in the vicinity of $x_1/H = 1.0$, laminarization is observed showing the stable stratification with the largest density differences occurring near the boundary. Very little turbulence is observed in this region, as shown in Fig. 3.11(c). Occasional turbulent structures are observed on the surface of the layer, but never penetrate to the wall. It should be noted that the images in Figs. 3.11(b) and 3.11(c) have been ‘brightened’ by a factor of 4 to improve contrast. Colormap values must be multiplied by 0.25 to obtain actual θ^* in these regions.

The flow is laminarized further away from the turning region because the flow is continuously seeking stable stratification. The Richardson number, $Ri = g\Delta\rho l_U / \rho_0 U^2$, is used to describe this competition between the potential energy

associated with density differences (which inhibits mixing and entrainment) and the kinetic flow energy (which promotes mixing and entrainment). Entrainment will be reduced along the ceiling layer as the Ri increases inhibiting mixing since buoyancy acts to stably stratify the ceiling layer. This effect is clearly observed along the ceiling in figure 3.11(c). The entrainment is almost completely inhibited in this region. The stratification has been observed when Ri is larger than 0.54 in this study. This Ri is much smaller than the value suggested by Alpert (about 1.1) [13] who considered the downstream flow started to affect the upstream stream flow behavior once the Ri greater than 1.1. The location where flow laminarization occurs largely depends on the characteristic Re_H . Larger Re_H results in a longer distance for flow to laminarize. Since Re_H is small in the small scale salt-water modeling experiments, the flow can laminarize despite a small Ri number. More experiments with various ceiling height and source strength are required for establishing a quantitative criterion of flow laminarization.

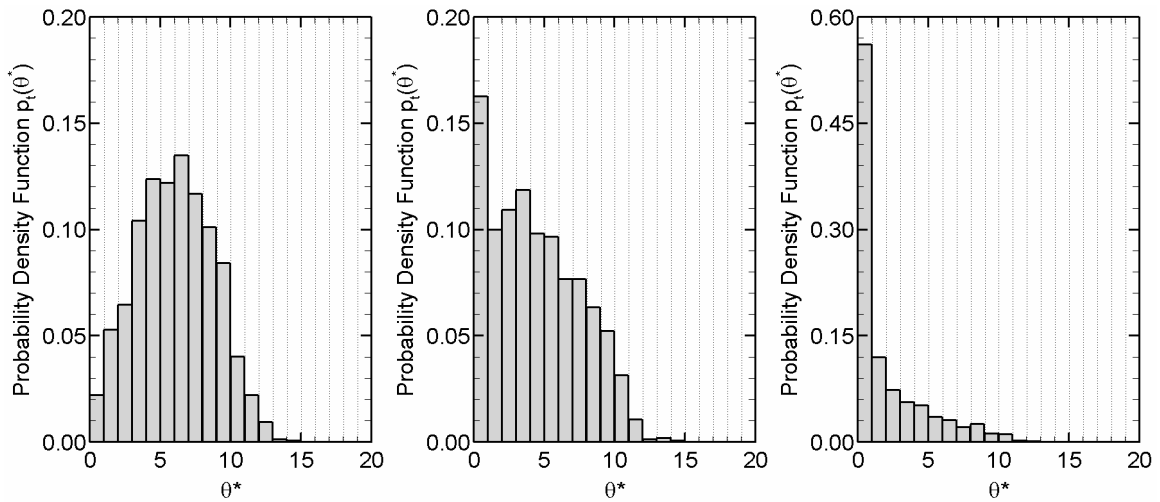


Figure 3.12: Probability Density Function $p_i(\theta^*)$ at $(x_1/H = 0.3)$ in the ceiling jet region for Case 4 (a) near ceiling location ($x_3/H = 0.99$); (b) middle location ($x_3/H = 0.95$); (c) edge location ($x_3/H = 0.95$)

Probability density functions at the radial location ($x_1/H = 0.3$) in the ceiling jet are presented in Fig. 3.12. The three locations represent the location near the ceiling surface ($x_3/H = 0.99$ or $x_3/l_T \sim 0$), the middle of the ceiling layer ($x_3/H = 0.975$ or $x_3/l_T \sim 0.5$) and the edge of the ceiling layer ($x_3/H = 0.95$ or $x_3/l_T \sim 1$). The spatial measurement values used to generate the Pdfs is the same as that are used in the turning region. Figure 3.12(a) shows the fresh water does infrequently penetrate to the ceiling surface which is consistent with the observation in Fig. 3.11(b). At the edge of the ceiling layer, high concentration fluid from the inner region is also observed. The wide uniform distribution in the middle of the layer indicates strong fluctuations and unmixedness at this location. In the middle of the ceiling jet region, the mixing is not as intense as that observed in the center of the turning region.

Besides the qualitative visualization of the flow mixing dynamics along the ceiling, the characteristics of the impinging jet can also be quantitatively characterized from the salt-water measurements. Additionally, these results are compared with other fire measurements and empirical models to verify the fidelity of the salt-water modeling measurements. The radial profile of the source independent characteristics $\bar{\theta}_{\max}^*$ and $(\bar{u}_1)_{\max}^*$ along the ceiling are provided in Fig. 3.13(a) and (b), respectively. The source independent velocity $(\bar{u}_1)^*$ is defined as $(\bar{u}_1)_{sw}^* = \bar{u}_1(\dot{m}_{sw}^*)^{-1/3}(gH)^{-1/2}$ for salt water and $(\bar{u}_1)_T^* = \bar{u}_1(\dot{Q}^*)^{-1/3}(gH)^{-1/2}$ for fire. Small-scale experiments conducted by Motevalli [15] and Veldman [16], correlations developed by Cooper, and analysis conducted by Alpert for large scale fires [12] are also plotted. The virtual origin used in Veldman's data is $z_0 = -110$ mm as discussed in §4.4. The mixing and the associated decay of $\bar{\theta}_{\max}^*$ and $(\bar{u}_1)_{\max}^*$ are clearly

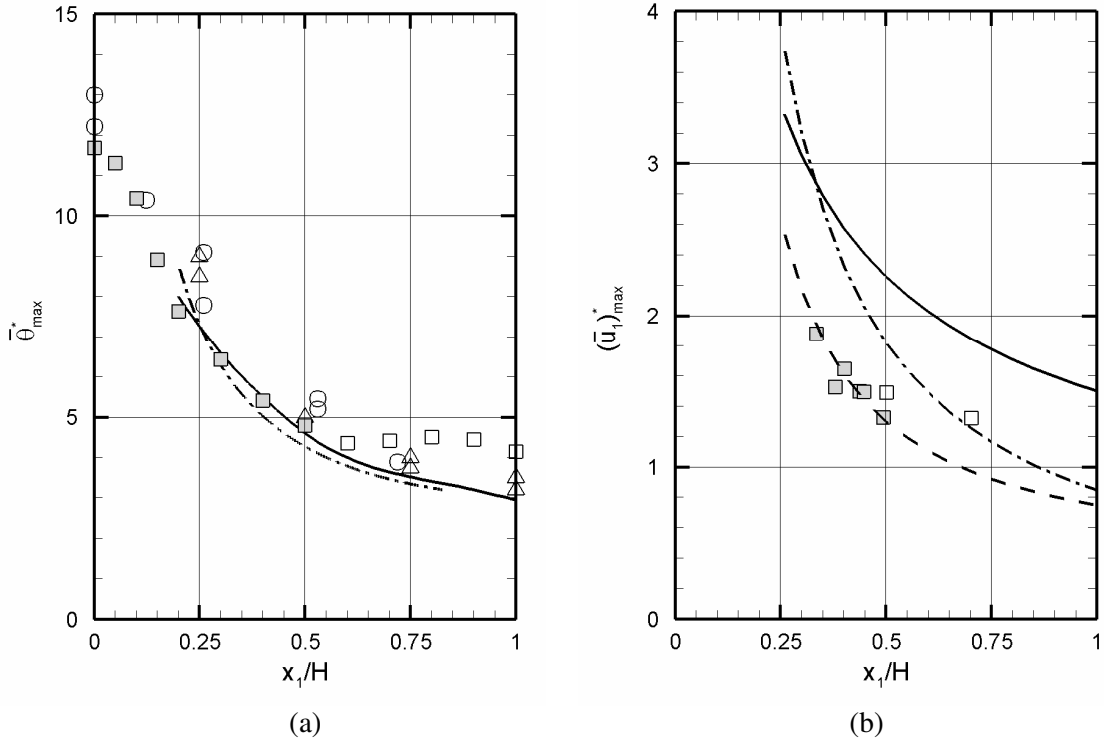


Fig 3.13: Peak values of source independent characteristics along the ceiling; (a) $\bar{\theta}_{max}^*$; (b) $(\bar{u}_1^*)_{max}$; \blacksquare salt water model; \square salt water model after laminarization; \triangle Motevalli [15]; \circ Veldman [16]; — Alpert theory [12]; - - - Cooper correlation [20]; . . . Motevalli correlation [15].

observed from the salt-water measurements. The quantitative agreement between similarly scaled salt-water and fire measurements is quite impressive in the distribution of $\bar{\theta}_{max}^*$ until a radial location about $x_1/H = 0.5$. Beyond this point, the flow starts to become laminarized in the salt-water model preventing continued mixing, which results in a slow decay of $\bar{\theta}_{max}^*$ and $(\bar{u}_1^*)_{max}$ along the wall. $\bar{\theta}_{max}^*$ and $(\bar{u}_1^*)_{max}$ decay in the ceiling layer because of turbulent mixing and entrainment. However, when the flow laminarizes, dilution of the ceiling layer flow ceases and $\bar{\theta}_{max}^*$ and $(\bar{u}_1^*)_{max}$ remains virtually constant along the ceiling. The velocity measurements of $(\bar{u}_1^*)_{max}$ agree very well with Motavevalli's correlation when $x_1/H <$

0.5. Motavalli [15] conducted detailed velocity measurements in the ceiling jet and his correlation is considered to be more reliable for predicting the velocity distributions in the ceiling jet. The large difference between salt-water measurements and Alpert's theory comes from the Gaussian shaped velocity profile assumption used in Alpert's analysis. Cooper's Model is based on less direct data and is developed from wall-jet theory of Poreh et al. [21]. The agreement between his model and salt-water modeling measurements is improved as x_1/H increases, but overestimates salt-water data by 30% to 50% in the region $x_1/H < 0.5$.

The thermal thickness of the ceiling layer, l_T , was determined from the PLIF salt-water measurements. This quantity provides an indication of the ceiling jet

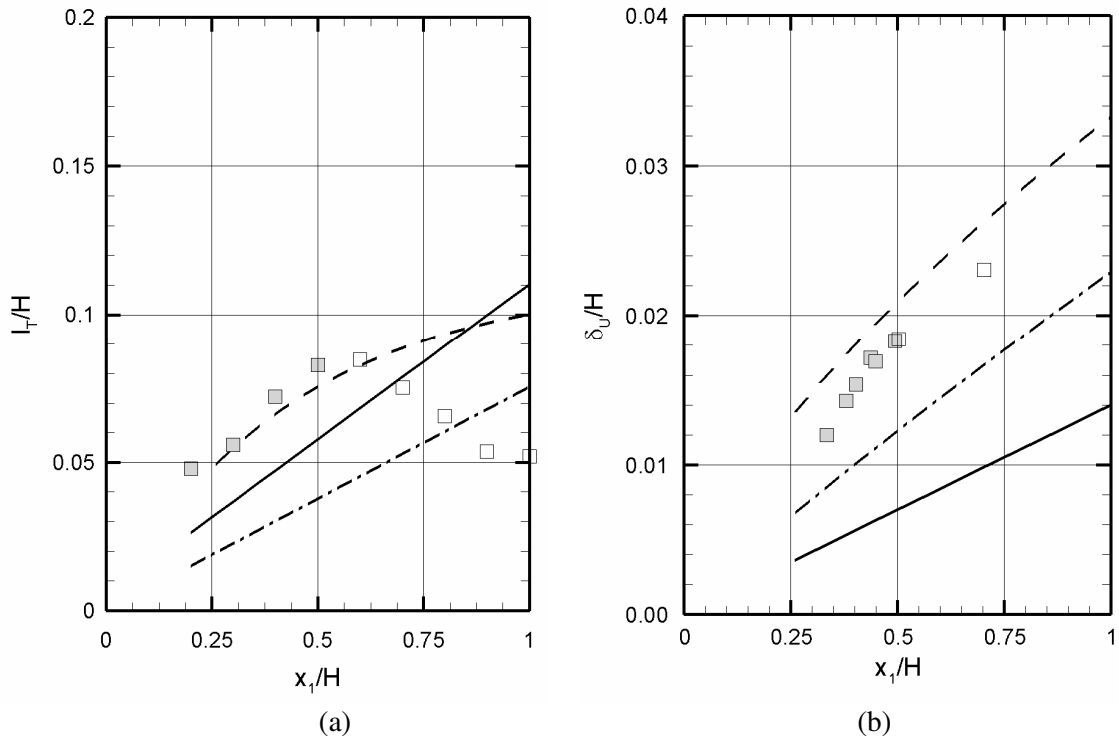


Fig 3.14: Ceiling jet characteristics along the ceiling; (a) dimensionless thermal thickness, l_T/H ; (b) dimensionless boundary layer thickness, δ_U/H ; \blacksquare salt water model; \square salt water model after laminarization; — Alpert theory [12]; - - - Cooper correlation [20]; - . - . Motavalli correlation [15].

thickness. The thermal thickness data presented in Fig. 3.14(a) compares favorably with Motevalli's correlation up to $x_1/H = 0.6$. Beyond this point, the flow begins to laminarize profoundly reducing entrainment resulting in layer thinning which is consistent with a radially expanding stratified layer. Alpert's theory and Cooper's correlations tend to underpredict the thermal thickness for $x_1/H < 0.6$. Similarly, Figure 3.14(b) plots the boundary layer thickness δ_U along the ceiling. The salt-water measurements show a reasonable magnitude and trend when compared to the fire experiments. The boundary layer thickness δ_U from salt-water measurements is much closer to Motevalli's data while larger than the predictions from Cooper's correlation and Alpert's theory. Figure 3.14(b) shows that the boundary layer growth is not significantly affected in the region beyond $x_1/H = 0.5$ although profound changes were observed in the trends of $\bar{\theta}_{\max}^*$, $(\bar{u}_1)_{\max}^*$ and l_T . As the flow transitions from turbulent to laminar conditions, the boundary layer grows less rapidly changing from $\delta_U \sim x_1^{4/5}$ to $\delta_U \sim x_1^{1/2}$ according to the theory. This slower growth rate is consistent with the measured trends. There is no momentum thickness, l_U , measurement in this study due to the limited velocity information at the edge of the ceiling layer. The flow velocity at the edge of the ceiling layer is very slow in this region resulting in a very low data acquisition rate. The low data rate made it impractical to obtain sufficient information for an l_U profile.

To further evaluate ceiling jet transport, normalized ceiling layer density difference profiles are compared at various x_1/H along the ceiling in Fig. 3.15(a). The distance from the ceiling is normalized by the thermal thickness l_T . The salt-water profile of $\bar{\theta}^* / \bar{\theta}_{\max}^*$ is described extremely well with a half-Gaussian profile, which is

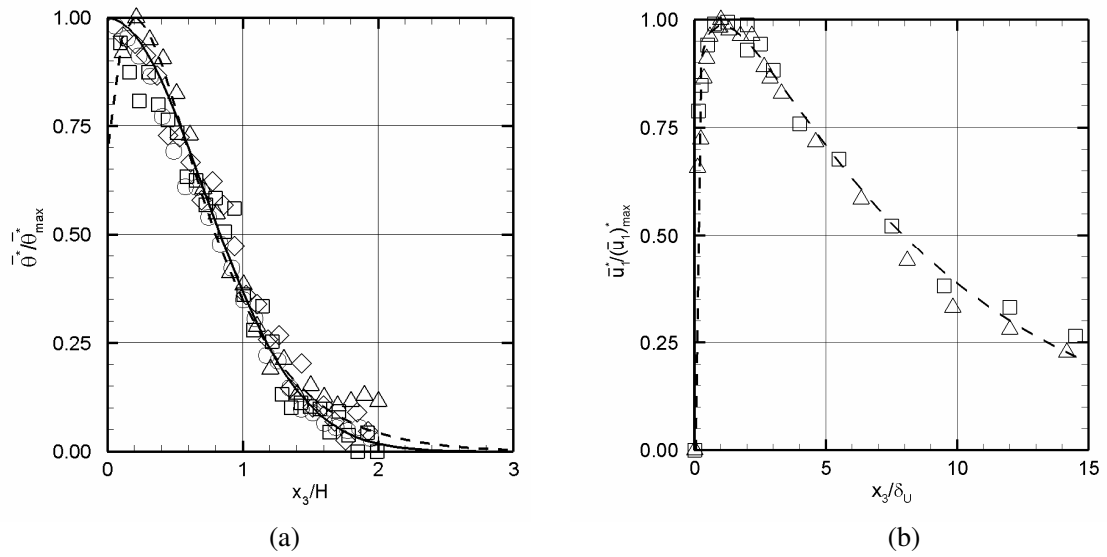


Fig. 3.15: Mean profiles of dimensionless density difference and velocity at various locations along the ceiling jet; (a) $\triangle x_1/H = 0.2$; $\diamond x_1/H = 0.4$; $\circ x_1/H = 0.6$; $\square x_1/H = 0.8$; ; (b) $\triangle x_1/H = 0.37$; $\square x_1/H = 0.41$; — Gaussian curve fit, $1/\exp(x_3/l_T)^2$; - - - Motevalli correlation [15].

consistent with Alpert's recommendation. The zero $\bar{\theta}^*$ gradient achieved close to the ceiling is consistent with the adiabatic wall analogy used in salt-water modeling. Motevalli's correlation compares favorably with this Gaussian behavior as well, except near the ceiling where the effect of heat losses becomes evident through steep wall gradients and off-ceiling peak temperatures. These heat losses persisted despite efforts by Motevalli to achieve an adiabatic wall in the fire configuration. The normalized ceiling layer velocity profiles at various x_1/H along the ceiling are plotted in Fig. 3.15(b). The distance from the ceiling is normalized by the boundary layer thickness δ_U . Figure 3.15(b) shows good agreement between salt-water model measurements and Motevalli's correlation.

3.3 Turbulent Mixing Dynamics

The ability of salt-water modeling to provide overall flow dynamics in canonical flow configurations has been demonstrated through comparisons between salt-water modeling and fire plume experiments. Alternatively, the salt-water measurements can be configured to resolve the sub-grid scale details of the flow. This provides an exciting opportunity for evaluating the turbulent mixing models used in CFD codes. One objective of this research is to show the potential for this technique to provide flow details for CFD model evaluation.

A brief description of LES mixing modeling is provided in Appendix C. In order to make easy comparison with LES simulations, the salt-water measurements are expressed in terms of the mixture fraction, Z , in this section. The mixture fraction Z is a dimensionless quantity describing the relative amount of the injected fluid at a prescribed location and time. The salt mass fraction based mixture fraction is defined as $Z_{sw} = Y_{salt}/(Y_{salt})_{source}$ in the salt-water experiments. The temperature based mixture fraction is defined as $Z_T = \Delta T/(\Delta T)_{source}$ in an LES thermal/fire plume simulation. This quantity is used explicitly in transport equations to describe mixing and combustion, as explained in Appendix C. In LES simulations, the mixture fraction Z is decomposed into a grid-resolved, Favre-filtered component \tilde{Z} and an unresolved, subgrid-scale fluctuation Z'' ,

$$Z(x, y, z, t) = \tilde{Z}(x, y, z, t) + Z''(x, y, z, t) \quad (3.4)$$

where \tilde{Z} is a function of time and it may be further decomposed into a time-averaged component $\langle \tilde{Z} \rangle$ and a grid-resolved fluctuation as

$$Z(x, y, z, t) = \underbrace{\langle \tilde{Z} \rangle(x, y, z)}_{\text{time-averaged value}} + \underbrace{(\tilde{Z}(x, y, z, t) - \langle \tilde{Z} \rangle(x, y, z))}_{\text{LES-resolved fluctuation}} + \underbrace{Z''(x, y, z, t)}_{\text{unresolved fluctuation}} \quad (3.5)$$

Presumed β -Pdf is in use to model the subgrid-scale mixing in LES. The β -Pdf distribution requires two statistical moments of mixture fraction within each filter volume (i.e. \tilde{Z} and σ_z). The mean mixture fraction \tilde{Z} is known from the resolved field but the variance σ_z must be modeled. The β -Pdf has been previously tested in the context of LES for flow having equilibrium chemistry without heat release [48, 49]. It has also been tested as part of a laminar flamelet model for a flow which does include the effects of heat release [50]. In both of these Direct Numerical Simulation (DNS) studies the β -Pdf distribution shows a good approximation to the subgrid-scale Pdf of mixture fraction. To the author's knowledge, no evaluation of the β -Pdf for buoyant flows has been conducted to date. The salt-water experiment provides spatially and temporally resolved information on turbulent mixing and is able to be used in the following study as a benchmark configuration to evaluate the (β -Pdf) model for the fire induced flow.

The method adopted to perform the comparison between salt-water measurements and LES simulations is explained below. Firstly, a small sampling volume in the experiment that matches the location and size of a given LES grid cell is selected. The salt-water experimental data is highly resolved and brings information on the instantaneous spatial variations of Z within the sampling volume that are not available in the LES solution. The spatial mean \tilde{Z} and standard deviation σ_z are extracted after some straightforward post-processing from the experimental

database. The resolved mixture fraction \tilde{Z} is also readily obtained from the LES solution, while σ_Z can be estimated using the closure model in Eq. (C.4). The comparison is then performed at the level of the spatial mean \tilde{Z} and the spatial standard deviation σ_Z . Additional data processing is performed to obtain the time probability density functions, $p_t(\tilde{Z})$ and $p_t(\sigma_Z)$.

The value of the salt-water modeling technique for sub-grid model development and model analysis becomes apparent upon analysis of the experimental results. For example, the minimum resolution used in the salt-water experiment is $40 \mu\text{m} \times 80 \mu\text{m}$ in the thickness of the laser sheet, which is smaller than the Kolmogorov length scale, λ_τ , in the plume down stream region (e.g. $\lambda_\tau = 100 \mu\text{m}$ at $x_3^+/D = 20$). Assuming a fictitious grid size of an LES model is $0.0596D \times 0.18D \times 0.596D$, a grid cell with its center located at $(x_1/D = 0.0298, x_3^+/D = 18.02)$ is selected as a sample to demonstrate the possibilities of the salt-water technique for LES model validation [7]. According to the camera resolution, 8×12 sub-grid cells in the salt-water measurements represent one grid cell in the LES simulation. It should be noted that the thickness of the laser sheet is about $500 \mu\text{m}$ in this study which is significantly larger than λ_τ . However, the average concentration gradient is known to be small across the laser sheet due to the axisymmetric plume configuration. The thickness of the laser sheet will result in some filtering which could not be avoided as it was not practical to further reduce the sheet thickness. Future CFD analysis could be useful to reveal the impact of the limited sheet resolution. It should also be noted that similar technique was used by Papantoniou et al.[51] along with careful scaling arguments to resolve the turbulent flow behavior down to the smallest flow scales.

The instantaneous spatial resolution achieved within the physical space defined by the cell is illustrated in Fig. 3.16(a). The spatial probability distribution of mixture fraction Z within the grid cell is provided in Fig. 3.16(b). The resolved mixture fraction \tilde{Z} is 0.0535 and the standard deviation σ_Z is 0.0186 at this instantaneous time. Substitution of \tilde{Z} , and σ_Z into Eq (C.4) leads to the corresponding instantaneous presumed β -Pdf profile. One spatial sub-grid scale result provides a very sparse Pdf for comparison with the β -Pdf model. A better test of the model could be achieved by interrogating the flow at all times and location to build a combined Pdf for a given \tilde{Z} and σ_Z for comparison with the model. This approach would test the β -Pdf model.

It is worth emphasizing that modelled and measured Pdfs can only be

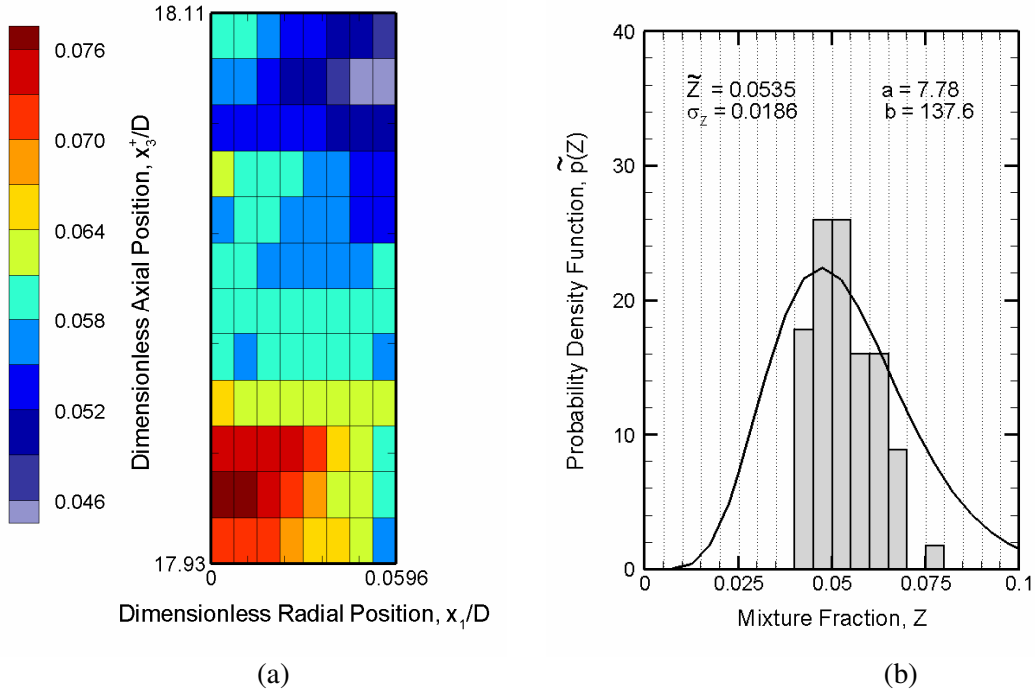


Fig. 3.16: Instantaneous mixture fraction Z for Case 1; (a) spatial distribution of Z (b) $\tilde{p}(Z)$ cell center at $(x_1/D = 0.0298, x_3^+/D = 18.02)$, cell size is $0.0596D \times 0.18D$.

described in a time-based statistical sense since instantaneous realizations of the flow differ in the experiment and the simulation. The temporal variation in spatial unmixedness within the grid cell region is quantified by the probability distribution of resolved mixture fraction, \tilde{Z} , and sub-grid scale standard deviation, σ_z , as shown in Fig. 3.17. Comparisons of the temporal Pdfs, $p_t(\tilde{Z})$ and $p_t(\sigma_z)$ between LES simulations and salt-water experiments will provide guidance on the quality of the subgrid-scale model used in the LES code. The temporally and spatially averaged $\langle \tilde{Z} \rangle$ at this location is 0.067 and the temporally and spatially average σ_z is 0.0112. More detailed comparison between salt-water modeling measurements and CFD model predictions was provided in Yao et al.[7]

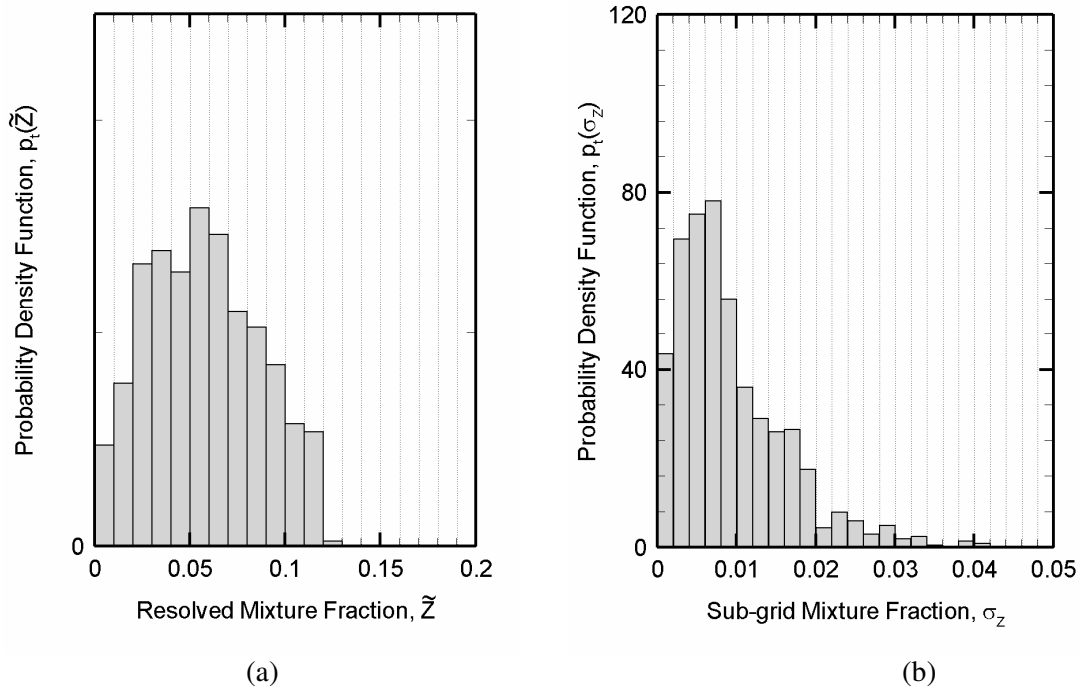


Fig. 3.17: Temporal Pdfs for Case 1; (a) resolved mixture fraction \tilde{Z} ; (b) subgrid-scale variance σ_z ; cell center is at $(x_1/D = 0.0298, x_3^+/D = 18.02)$, cell size is $0.0596D \times 0.18D$.

Chapter 4: Adiabatic Wall Heat Transfer Model

The quantitative salt-water modeling experiments have shown impressive agreement with real fire induced flow measurements as demonstrated in Chapter 3. This technique has proven to be a useful tool for high fidelity measurement of fire induced flow dynamics in a well controlled, economic way. Characteristics of the complex flow behavior from salt-water measurements show insight into the detailed flow dynamics. Generally, salt-water modeling is only able to simulate a fire scenario without consideration of the heat transfer effects. In this study, the quantitative salt-water technique is applied to establish an engineering adiabatic wall heat transfer model which will be able to predict the convective heat transfer rate from the hot ceiling layer to the ceiling surface.

4.1 Introduction

Newton's law of cooling provides the heat transfer rate to the ceiling in terms of a convective heat transfer coefficient and the temperature difference between the surface and some characteristic temperature of the fluid, usually the free-stream temperature. However, in many complex flow configurations, the fluid temperature is not well defined. A reference temperature is used to calculate the heat transfer. The convective heat transfer is expressed in Eq. (4.1),

$$\dot{q}'' = h\Delta T = h(T_{ref} - T_w) \quad (4.1)$$

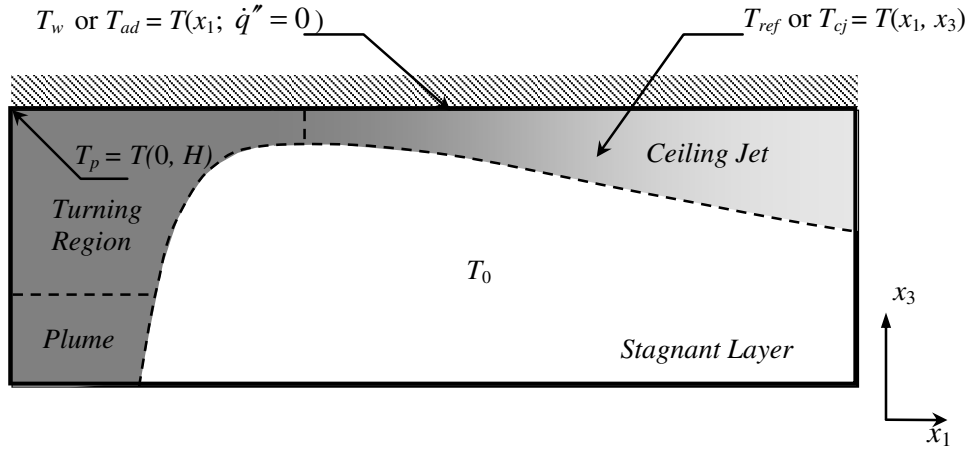


Figure 4.1: Temperature characteristics in impinging plume flow configuration

where T_w is the local wall temperature, T_{ref} is the reference temperature, as shown in Fig. 4.1. In the limiting case, the wall is perfectly insulated and the resulting surface temperature is called the adiabatic temperature, T_{ad} . It is easy to see that the reference temperature is the adiabatic wall temperature by setting $\dot{q}''_w = 0$ in Eq. (4.1). Thus Eq. (4.1) is revised as

$$\dot{q}'' = h(T_{ad} - T_w) \quad (4.2)$$

The adiabatic wall temperature is dependent on many quantities, including the mass flow rate of the plume, the temperature of the impinging plume, the ambient temperature, etc. Goldstein et al. [52] have adopted the impingement cooling/heating effectiveness to express the adiabatic wall temperature in dimensionless form based on the recovery temperature, the ambient temperature and total impinging plume temperature. In this study, the same concept has been used with modifications. The effectiveness is defined by

$$\eta = \frac{T_{ad} - T_0}{T_p - T_0} \quad (4.3)$$

where T_P is the temperature of the plume at the impinging point, T_0 is the ambient temperature (refer to Fig. 4.1). Generally, the adiabatic wall temperature T_{ad} is larger than the ambient temperature T_0 and smaller than the impinging point plume temperature T_P , which is $T_0 \leq T_{ad} \leq T_P$. Thus the effectiveness parameter varies from unity at the impinging point (where $T_{ad} = T_P$) to zero far down stream where, because of the dilution of the entrainment flow, the adiabatic wall temperature approaches the free stream temperature. Revision of Eq. (4.3) results in,

$$T_{ad} = T_0 + \eta(T_P - T_0) \quad (4.4)$$

After substitution of Eq. (4.4) into Eq. (4.2), the convective heat transfer rate can be expressed as

$$\dot{q}'' = h[(T_P - T_w) - (1 - \eta)(T_P - T_0)] \quad (4.5)$$

Eq. (4.5) clearly shows the convective heat transfer rate \dot{q}'' can be considered as two parts. The first part is the maximum possible heat transfer caused by the temperature difference between T_P and T_w and the second part is the correction to this maximum heat transfer because the reference temperature is somewhere between T_P and T_0 .

The salt-water measurements will be used to establish scaling laws for the two important quantities, the convective heat transfer coefficient h and the effectiveness η , in terms of the global parameters (e.g. x_1^* , H , Pr , Re_H), where $x_1^* = x_1 / H$ dimensionless radial location along ceiling. The Reynolds number, Re_H , is based on the characteristic velocity $U = (gH)^{1/2} (Q^*)^{1/3}$ and the ceiling height H . There are two types of salt-water modeling experiments used to establish the adiabatic wall heat transfer model, PLIF salt-water experiments and LDV salt-water

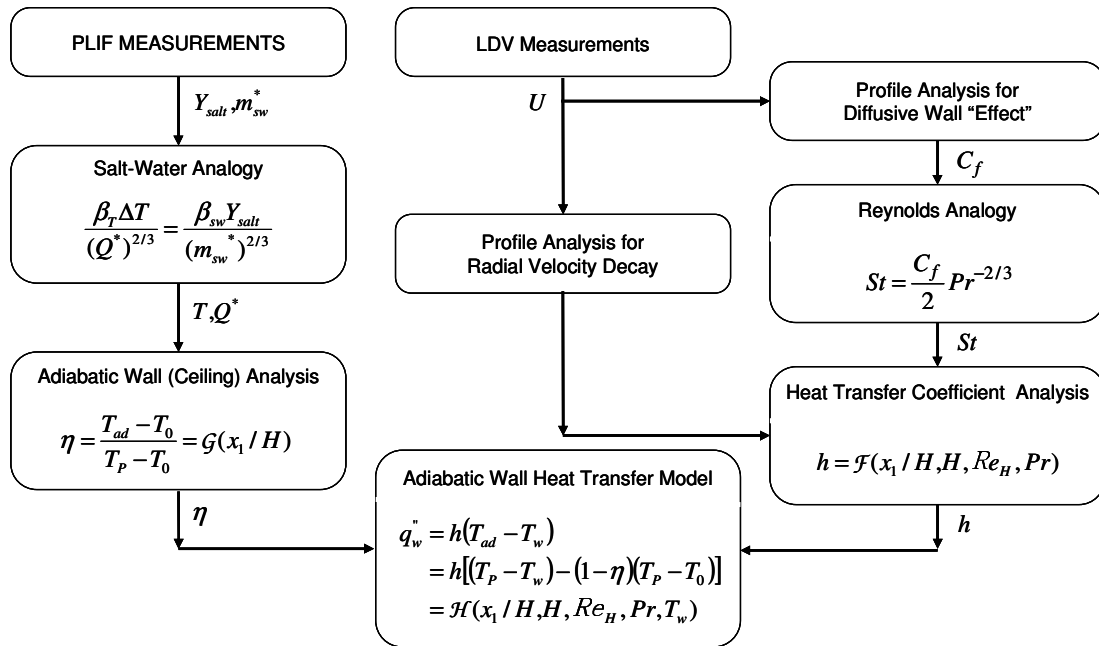


Figure 4.2: Adiabatic wall heat transfer model

experiments. The dimensionless density difference measured from the PLIF measurements is used for the scaling law of η while the detailed velocity measured from the LDV measurements is used to establish the scaling law of h . A flow chart of the adiabatic wall heat transfer model is provided in Fig. 4.2. First, PLIF salt-water experiments measure the salt mass fraction distributions in the salt-water plume. The impermeable ceiling surface in the salt-water model is analogous to an adiabatic wall boundary condition in the actual fire induced flow. Thus the measured salt-water mass fraction at the ceiling corresponds to the adiabatic surface temperature, T_{ad} . The correlation of cooling effectiveness η is derived from the converted T_{ad} and can be expressed as a function of radial position x_1^* . On the other hand, the heat transfer

coefficient used in this study comes from Reynolds analogy where the Stanton number describing wall heat flux is given as

$$St = \frac{h}{\rho c_p U} = \frac{C_f}{2} Pr^{-2/3}. \quad (4.6)$$

This quantity is related to viscous wall interactions determined by $C_f = \tau_w (\rho U^2 / 2)^{-1}$. LDV salt-water measurements provide the ability to analyze the velocity, U , and the corresponding friction coefficient, C_f . Both of these characteristics are important in the Reynolds analogy. The heat transfer coefficient h can also be expressed as functions of x_1^* , H , Re_H and Pr . Substitution of scaling laws for η and h into Eq. (4.5) results in an expression for the convective heat transfer rate, \dot{q}'' , where

$$\dot{q}'' = \mathcal{H}(x_1^*, H, Re_H, Pr, T_w). \quad (4.7)$$

Detailed analysis of the adiabatic wall heat transfer model is provided in the following sections. Comparisons between this model and fire experiments are also presented to evaluate the model quality.

4.2 Effectiveness η

A general expression for effectiveness η can be obtained from measurements of the source independent density difference. The effectiveness η in Eq. (4.3) can be rewritten in terms of the source independent dimensionless density difference, θ^* , as

$$\eta = \frac{\theta_{ad}^*(x_1^*)}{\theta_p^*}, \quad (4.8)$$

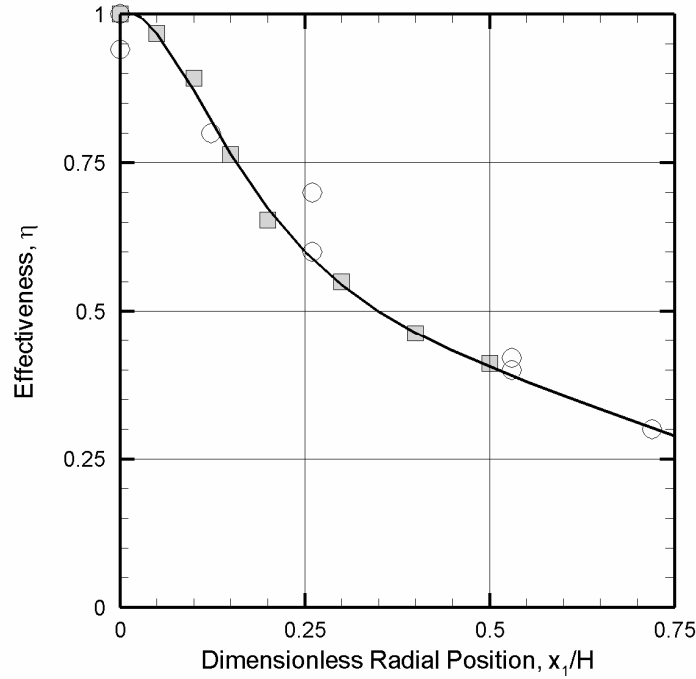


Figure 4.3: Distribution of effectiveness η along ceiling; \blacksquare salt water measurements for Case 1; \circ Veldman [16]; — Curve of Eq. (4.9)

where

$$\theta_{ad}^*(x_1^*) = \theta^* \Big|_{x_3^*=1} = \beta_T (T_{ad}(x_1^*) - T_0) (Q^*)^{-2/3},$$

$$\theta_p^* = \theta_{ad}^*(x_1^* = 0).$$

As discussed before, the impinging plume θ_p^* equals to 11.7 which is considered as the source independent density difference at the stagnation point which equals to the centerline value at $0.85H$ in the unconfined plume configuration.

The effectiveness distribution from salt-water measurement along the radial coordinate is provided in Fig. 4.3 along with measurements from actual fire data. The experimental data are reduced to a best-fit function similar in form to the equation used by Veldman et al. [16]

$$\eta = \frac{-6.67 \cdot (x_1^*)^4 + 10.69 \cdot (x_1^*)^2 + 1.01}{(x_1^*)^4 + 27.93 \cdot (x_1^*)^2 + 1}, \quad (4.9)$$

where the coefficients are determined from the regression analysis of the salt-water measurements. Figure 4.3 clearly shows that the expression in Eq. (4.9) predicts the effectiveness very well. It should be noted that the salt-water measurements are only available from $0 \leq x_1/H \leq 0.5$ as discussed in §3.2.3. However, this correlation predicts the fire data well beyond this point. Since the ceiling jet layer is considered to start at $x_1/H \geq 0.2$. It is reasonable to consider Eq. (4.9) applicable in both the impinging region and the ceiling jet region. The expression included in Eq. (4.9) is completely general for the impinging plume configuration and does not depend on fire size or ceiling height.

4.3 Convective Heat Transfer Coefficient h

Reynolds analogy is used to establish a general expression for the convective heat transfer coefficient h from salt-water model results. Based on the definition of Stanton number [53], Eq. (4.6) can be expressed in terms of Nusselt number and Reynolds number,

$$St = \frac{Nu_x}{Re_x Pr} = \frac{C_f}{2} Pr^{-2/3}, \quad (4.10)$$

where $Nu_x = \frac{hx_1}{k}$ is the local Nusselt number at radial position x_1 , $Re_x = \frac{(u_1)_{\max} x_1}{\nu}$ is the local Reynolds number based on the maximum velocity $(u_1)_{\max}$ and radial position x_1 , k is the conductive heat transfer coefficient of the ambient flow.

Rearranging Eq. (4.10) yields the local heat transfer coefficient h in terms of Re_x and Pr as

$$Nu = \frac{h}{k/x_1} = \frac{C_f}{2} Re_x Pr^{1/3}. \quad (4.11)$$

The friction factor C_f is the key quantity for establishing the scaling law for the heat transfer coefficient. The friction factor can be directly measured by a Preston probe. However the Preston probe measurement is only reliable when the test flow condition is similar to its calibration flow condition. Generally, a Preston probe is calibrated under a laminar boundary flow condition. Consequently measurement in the turbulent boundary layer is not accurate. As an alternative to direct measurement of the shear stress, the wall shear stress and the associated C_f are determined from integral analysis of the ceiling jet. The assumed velocity profiles for this analysis are determined from the salt-water experimental data. However, velocity measurement could not be obtained in the impinging region as discussed in §3.1.2. The absence of detailed velocity information limited the application of Reynolds analogy in the turning region. The scaling law of the heat transfer coefficient in the turning region is established based on impinging jet theory and Veldman's [16] experimental data.

4.3.1 Velocity Similarity Function in the Ceiling Jet

In the ceiling jet, the mean velocity \bar{u}_1 has a similarity profile. A schematic of velocity similarity profile in the ceiling jet is shown in Fig 4.4, where \bar{u}_1 is the temporal mean velocity, u_1' and u_3' are the corresponding fluctuating components of u_1 and u_3 , δ_1 is the maximum velocity position and δ_2 is the zero shear stress position,

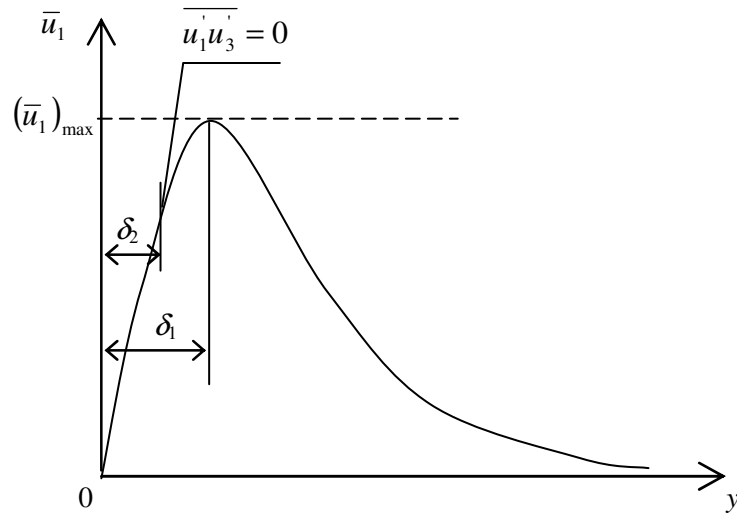


Figure 4.4: Velocity similarity profile in the ceiling jet layer

y is the distance from ceiling surface. The similarity transform variable is defined as $\chi = y/\delta_1$ and the similarity function $f(\chi)$ as $\bar{u}_1 / (\bar{u}_1)_{\max}$. Thus the maximum mean velocity, $(\bar{u}_1)_{\max}$, and its position, δ_1 , are two important quantities in the determination of the velocity similarity function. Ultimately, correlations for $(\bar{u}_1)_{\max}$ and δ_1 along the ceiling are required for calculation of C_f from integration of the momentum equation of the ceiling jet.

Source independent velocity measurements have been obtained in the salt-water model and have been shown to agree well with fire data. The source independent velocity $(\bar{u}_1)_{\max}$ is defined as

$$(\bar{u}_1^*)_{\max} = \frac{(\bar{u}_1)_{\max}}{U}, \quad (4.12)$$

where $U = (gH)^{1/2} (Q^*)^{1/3}$ is the characteristic velocity of the impinging plume. A power law correlation is used to describe the velocity profile in the boundary layer

according to wall jet theory [54, 55]. The correlation for ceiling jet velocity is expressed as

$$(\bar{u}_1^*)_{\max} = c_1 (x_1^*)^{-\alpha} \quad (4.13)$$

where $x_1^* = x_1 / H$ is the dimensionless location along the ceiling. Figure 4.5 is a replot of the data in Fig. 3.13(b) with Eq. (4.13). The constants $c_1 = 0.727$ and $\alpha = 0.878$ come out of the regression analysis. Substitution of Eq. (4.13) into Eq. (4.12) results in an expression of maximum velocity as

$$(\bar{u}_1)_{\max} = c_1 U (x_1^*)^{-\alpha} \quad (4.14)$$

The distribution of the δ_1/H along the ceiling is plotted in Fig. 4.5(b). A linear growth rate is expected for δ_1/H based on the wall jet theory. The correlation

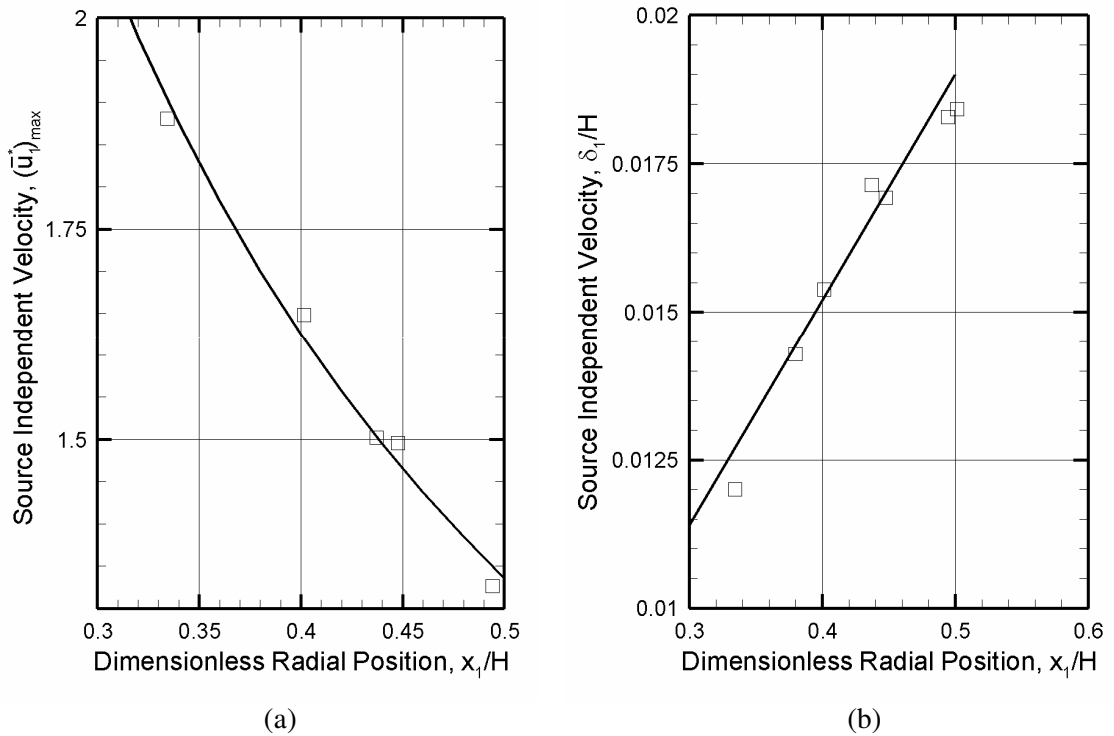


Figure 4.5: Scaling laws of distribution of source independent velocity and maximum velocity position, (a) $(\bar{u}_1^*)_{\max}$; \square salt water model; — curve of Eq. (4.13) with $c_1 = 0.727$, $\alpha = 0.878$; (b) δ_1/H ; \square salt water model; — curve of Eq. (4.15) with $c_2 = 0.038$

$$\frac{\delta_1}{H} = c_2 x_1^* \quad (4.15)$$

predicts the distribution of δ_1/H very well from the data obtained in the range $0.3 \leq x_1/H \leq 0.5$ with $c_2 = 0.038$.

An expression for the similarity profile in the boundary layer region is also required for determination of C_f from integral analysis. The similarity profile for $\bar{u}_1 / (\bar{u}_1)_{\max}$ in the boundary layer of the salt-water ceiling jet is provided in Fig. 4.6. A simple exponential function of $f(\chi)$,

$$\bar{u}_1 / (\bar{u}_1)_{\max} = f(\chi) = 1.03 \chi^{1/n} \quad (4.16)$$

proposed by Patla [56] and Schwarz et al. [57] is applied here to fit the experimental data in the boundary layer. The constant $n = 5.707$ is determined from the regression

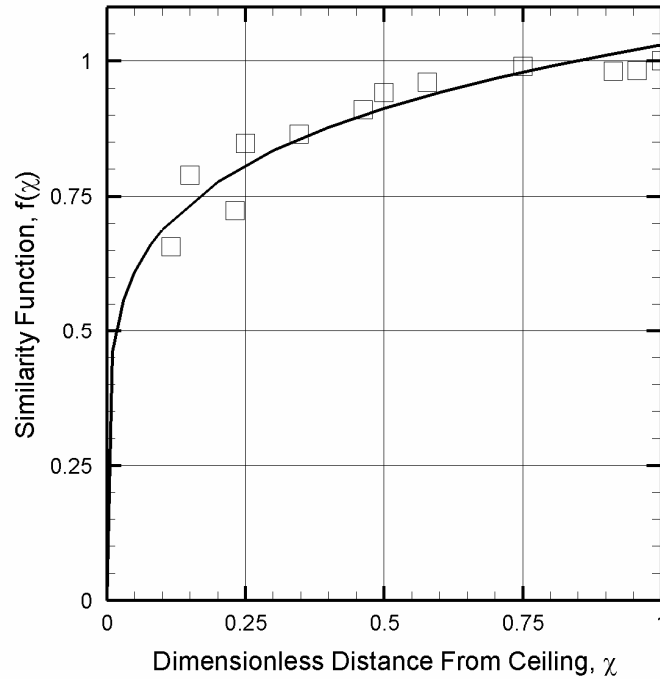


Figure 4.6: Similarity function of $f(\chi)$ in boundary layer; \square salt water model; — curve of Eq. (4.16) with $n=5.707$; - - - Motevalli's correlation [15]

analysis of the data. Equation (4.16) accurately describes the data for values of χ up to 0.75 providing a description velocity profile near the wall for the friction factor analysis.

4.3.2 Friction Coefficient C_f

Outside the turning region, the ceiling jet behaves like a wall jet. This provides the theoretical basis to analyze the friction coefficient [55]. In order to obtain the wall shear stress which is essential for C_f , integration across the entire ceiling layer is usually performed. However, since the contribution to the shear stress from the free stream to the location of zero turbulent shear stress ($y = \delta_2$) is zero, only the inner portion ($0 \leq y \leq \delta_2$) needs to be considered. Kruka et al. [55] evaluated the friction coefficient C_f based on the velocity similarity function in the wall boundary layer and determined that

$$C_f = 2c_2[\alpha\psi + (\phi - \psi)(1 - \alpha)] \quad (4.17)$$

where ϕ and ψ are integrals of the similarity function,

$$\phi = f(\chi_2) \int_0^{\chi_2} f(\xi) d\xi \quad (4.18)$$

$$\psi = \int_0^{\chi_2} f^2(\xi) d\xi. \quad (4.19)$$

The constant c_2 is the coefficient in the radial profile of δ_1 (Eq. 4.16) and α is the exponent in radial profile of the maximum velocity $(\bar{u}_1^*)_{\max}$ (Eq. 4.14). Substitution the similarity function of velocity (i.e. Eq. (4.16)) into Eq. (4.18) and Eq. (4.19) results in

$$\phi = f(\chi_2) \int_0^{\chi_2} f(\zeta) d\zeta = 0.903 * \chi_2^{1.354} \quad (4.20)$$

$$\psi = \int_0^{\chi_2} f^2(\zeta) d\zeta = 0.784 * \chi_2^{1.354} . \quad (4.21)$$

Then the friction coefficient is reduced to

$$\begin{aligned} C_f &= 2c_2 [\alpha\psi + (\phi - \psi)(1 - \alpha)] \\ &= 2 * 0.038 * [0.878 * 0.784 + (0.903 - 0.784) * (1 - 0.878)] \chi^{1.354} . \quad (4.22) \\ &= 0.053 \chi_2^{1.354} \end{aligned}$$

As shown in Fig. 4.4, χ_2 is the zero shear stress position where $\overline{u_1' u_3'} = 0$. Using simple mixing-length arguments, Lauder [58] suggested that the length scale of the zero shear stress position is smaller than that of the maximum velocity position in an axisymmetric turbulent shear flow. Tailland and Mathieu [59] quantitatively predicted the length scale of χ_2 to be about 0.55 of the length scale of χ_1 in the turbulent boundary layer. Since the salt-water plume is fully turbulent in the ceiling jet layer, Tialand and Mathieu's prediction of χ_2 is applied in this study. Replacing $\chi_2 = 0.55$ in the Eq. (4.22) yields a friction coefficient, $C_f = 0.024$. Previous impinging jet studies have assumed that C_f changes very little in the ceiling jet layer and can be assumed as a constant number [12, 60]. The similarity analysis used in this salt-water study yields a similar result. However, there is little consensus as to what this constant C_f should be. Previous friction factor data of Alpert [12], Veldman et al. [16] and You and Faeth [61] are bounded by the prediction for $C_f = 0.02$ and $C_f = 0.04$. The friction factor measured from the salt-water modeling experiments falls within the bounds suggested by Alpert's. The value of C_f determined for this analysis provides a good estimate for h as will be demonstrate in §4.3.3.

4.3.3 Convective Heat Transfer Coefficient, h

As shown in Eq. (4.11), the local heat transfer coefficient is a function of local Reynolds number, Re_x . Applying Eq. (4.14) to the definition of Re_x , the local Reynolds number Re_x can be revised in term of the characteristic Reynolds number based on the ceiling height, $Re_H = UH / \nu$, so that

$$\begin{aligned} Re_x &= c_1 \frac{Ux_1}{\nu} (x_1^*)^{-\alpha} \\ &= c_1 Re_H (x_1^*)^{1-\alpha} \end{aligned} \quad (4.23)$$

Substitution of Eq. (4.23) into Eq. (4.11) and using $Pr = 0.711$ for the air at 25 °C [62] results in a correlation of h in terms of Re_H , x_1^* and H ,

$$\begin{aligned} Nu &= \frac{h}{k/H} = \mathcal{F}(x_1^*, Re_H) \\ &= 0.00779 Re_H (x_1^*)^{-0.878} \end{aligned} \quad (4.24)$$

Equation (4.23) has been developed from the salt water modeling data in the range of $0.3 \leq x_1^* \leq 0.5$, however, it is reasonable to believe that Eq. (4.23) should be valid in the extra extent of the ceiling jet before laminarization occurs.

In the current study, the convective heat transfer coefficient in the plume turning region is determined from impinging jet theory and fire experimental data. The friction factor, C_f , can also be evaluated from the integral analysis of the similarity function of velocity in the turning region as that in the ceiling jet region. The similarity analysis in the turning region provides Nu in terms of $Re_D^{1/2}$ for a laminar jet [62], where Re_D is the characteristic Reynolds number based on the jet diameter. For a turbulent impinging jet, the exponent of Re_D is 0.8 suggested by Donaldson, et al. [63] and Han and Goldstein [64]. Since the turbulent impinging

plume configuration is similar to the turbulent impinging jet. The same scaling law used for ceiling jet is used for this impinging plume with Re_H replacing Re_D . A fourth order polynomial correlation

$$Nu = \frac{h}{k/H} = 0.711Re_H^{0.8} f_1(x_1^*, Re_H) \quad (4.25)$$

is applied to predict the heat transfer coefficient in the turning region ($0 \leq x_1^* \leq 0.2$),

where $f_1(x_1^*, Re_H)$, is expressed as

$$f_1(x_1^*, Re_H) = 0.427 + (2.77Re_H^{0.2} - 21.35)(x_1^*)^2 - (40.89Re_H^{0.2} - 266.88)(x_1^*)^4, \quad (4.26)$$

derived from the regression analysis of Veldman's experimental data [16]. This polynomial function provides a zero gradient for h at the stagnation point (local maximum) and matches the value and derivative of h at the turning region and ceiling jet interface (i.e. $x_1/H = 0.2$).

The scaling law of heat transfer coefficient h along the ceiling is then expressed as

$$\frac{h}{k/H} = \begin{cases} 0.711Re_H^{0.8} f_1(x_1^*, Re_H) & 0 \leq x_1^* \leq 0.2 \\ 0.00779Re_H f_2(x_1^*) & 0.2 \leq x_1^* \end{cases} \quad (4.27)$$

where

$$f_1(x_1^*, Re_H) = 0.427 + (2.77Re_H^{0.2} - 21.35)(x_1^*)^2 - (40.89Re_H^{0.2} - 266.88)(x_1^*)^4$$

$$f_2(x_1^*) = (x_1^*)^{-0.878}$$

$$Re_H = \frac{g^{1/2} H^{3/2} (Q^*)^{1/3}}{\nu}$$

Since Re_H is the characteristic Reynolds number based on the characteristic velocity,

$U = (gH)^{1/2} (Q^*)^{1/3}$, the heat transfer coefficient is also a function of the

dimensionless source strength Q^* . Comparisons of the dimensionless heat transfer coefficient in Stanton number between Eq. (4.27) and Veldman's measurements are provided in Fig. 4.7. Also shown in this figure are two theoretical curves obtained by Alpert [12]. It is worth mentioning that Alpert based h on a mean flow velocity in the Reynolds analogy and assumed a Gaussian velocity profile. The mean velocity is $1/\sqrt{2}$ times the maximum velocity. Therefore, in order to correlate h obtained with this study, Alpert's values of h are divided by a factor of $\sqrt{2}$.

As shown in Fig. 4.7, the prediction of h from the salt-water modeling with $C_f = 0.024$ agrees well with Veldman's measurements in both tests and lies within the area bounded by Alpert's theoretical curves for $C_f = 0.02$ and $C_f = 0.04$ providing a good estimate. In the turning region, the correlation from Eq. (4.27) splits to two

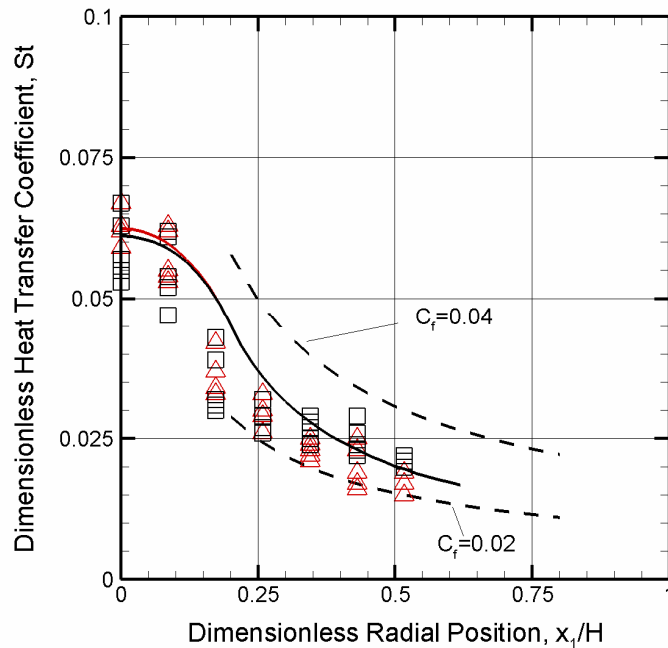


Figure 4.7: Heat transfer coefficient along ceiling; — Eq. (6.28) curve for Veldman's Test 1; — Eq. (6.28) curve for Veldman's Test 2; $C_f = 0.024$; - - - Alpert's correlation; \square Veldman's experiments Test 1, $H = 0.813$ m, $Q = 1.17$ kW; \triangle Veldman's Test 2, $H = 0.584$ m, $Q = 1.17$ kW [16]

lines according to the fire configuration. This separation is caused by the St defined in Eq. (4.10). Eq. (4.27) clearly shows the heat transfer coefficient h is proportional to Re_H in the ceiling layer while it is only proportional to $Re_H^{0.8}$ in the turning region. The Re_H effect in the St can not be avoided in the plume turning region. The difference between the current model and experimental measurements is more apparent at the end of the turning region and beginning of the ceiling jet region. The heat transfer coefficient is quite sensitive to small changes in C_f in this region and addition salt-water data in this region may improve the estimate.

4.4 Adiabatic Wall Heat Transfer Model

Substitution of Eq. (4.9) and Eq. (4.27) into Eq. (4.5) results in an adiabatic wall heat transfer model,

$$\dot{q}'' = h[(T_p - T_w) - (1 - \eta)(T_p - T_0)] \quad (4.28)$$

where

$$\eta = \frac{-6.67(x_1^*)^4 + 10.69(x_1^*)^2 + 1.01}{(x_1^*)^4 + 27.93(x_1^*)^2 + 1} \quad 0 \leq x_1^* \leq 5;$$

$$\frac{h}{k/H} = \begin{cases} 0.711Re_H^{0.8} f_1(x_1^*, Re_H) & 0 \leq x_1^* \leq 0.2 \\ 0.00779Re_H f_2(x_1^*) & 0.2 \leq x_1^* \leq 5 \end{cases};$$

$$f_1(x_1^*, Re_H) = 0.427 + (2.77Re_H^{0.2} - 21.35)(x_1^*)^2 - (40.89Re_H^{0.2} - 266.88)(x_1^*)^4;$$

$$f_2(x_1^*) = (x_1^*)^{-0.878}; \quad Re_H = \frac{g^{1/2} H^{3/2} (Q^*)^{1/3}}{\nu}; \quad x_1^* = \frac{x_1}{H}.$$

Scale should be considered when determining the radial extent for model predictions.

The model has been validated out to $x_1^* = 0.7$ using relatively small laboratory fire

configurations. These small laboratory fires are only nearly turbulent and laminarization may occur at early radial location. The radial location where laminarization occurs will depend on Re_H . However, a criterion for determining this location is not yet available. In the absence of laminarization, this model should be valid up to $x_1^* = 5$ [12]. Beyond this point, the Richardson number, Ri , is above a critical value and downstream effects, impossible to be included in this model, can alter the ceiling layer behavior.

Some guidance should be provided before applying this heat transfer model to predict the convective heat transfer rate to the ceiling. The \dot{Q} used in this model is the convective heat release rate, \dot{Q}_c . In actual fires, the energy released from the source is convected upwards, \dot{Q}_c , and radiated outward, \dot{Q}_r . Under certain conditions, the radiation heat loss from the flame can be neglected (i.e. if the flame height, H_f , is relatively small). For instance, in Veldman's experiments [16], a burner providing a compact flame was used and $\dot{Q}_c = \dot{Q}$. In most fires, flame radiation is significant and the convective energy flux is only a fraction of the total energy release. For example, it was estimated that $\dot{Q}_c \approx 0.8\dot{Q}$ in You and Faeth's experiments [17]. It should also be noted that stagnation point temperature is defined based on the ceiling height from the virtual point source, H . Neglecting the virtual origin will either overpredict T_p if $z_0 < 0$ or underpredict T_p if $z_0 > 0$.

Comparisons between the current adiabatic wall heat transfer model and You's [17] weak fire plume experiments are provided in Fig. 4.8. The experimental configurations in You's experiments are $\dot{Q} = 0.385$ kW, $H_f/H_c = 0.15$ and $\dot{Q} = 0.24$

kW, $H_f/H_c = 0.008$, respectively. The distance between the burner and ceiling is 400 mm. The ceiling temperature is nearly constant and equal to the ambient temperature during experiments. The virtual origins of these experiments are $z_0 = -17$ mm for case $\dot{Q} = 0.385$ kW and $z_0 = -24$ mm for case $\dot{Q} = 0.24$ kW based on Hasemi and Tokunaga's correlations [65]. The thermal radiation is not quantitatively measured but estimated to range from 0 to 20% of the total heat release rate. Convective heat sources are used in the model according to these estimates (i.e. $\dot{Q}_c = \dot{Q}$ and $\dot{Q}_c = 0.8\dot{Q}$). As shown in Fig. 4.8, the estimate for radiation losses significantly affects the model predictions. Figure 4.8 clearly shows the convective heat transfer rate is overestimated by neglecting the thermal radiation heat loss. The agreements between current heat transfer model and measurements is improved when using

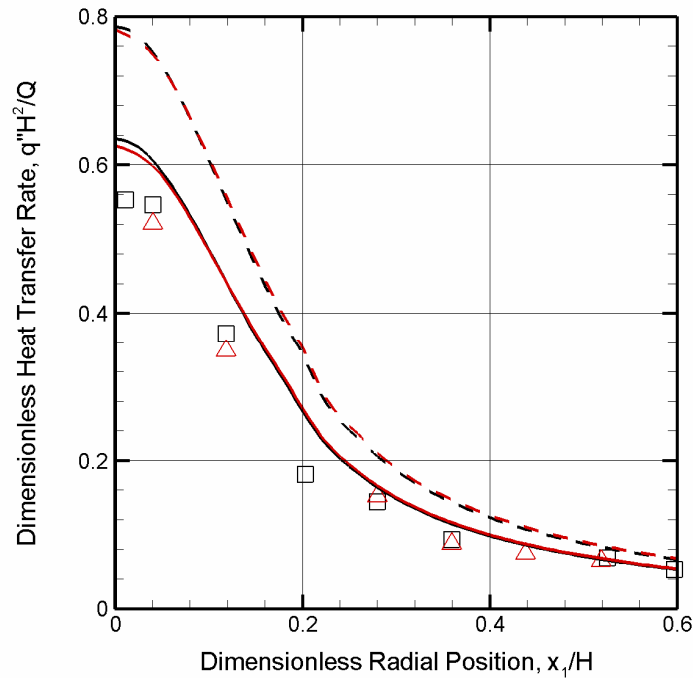


Figure 4.8: Heat transfer rate along ceiling radial position between model and You's experiments (a) You's experiments, \square $Q = 0.385$ kW, $H_f/H_c = 0.15$; \triangle $Q = 0.24$ kW, $H_f/H_c = 0.08$; — — Author's Model with $Q_c = Q$; — Author's Model with $Q_c = 0.8Q$;

$\dot{Q}_c = 0.8\dot{Q}$, especially in the turning region. The agreement in the ceiling jet region is very impressive using $\dot{Q}_c = 0.8\dot{Q}$. The difference in the turning region indicates the thermal radiation heat loss may be even larger than 20% of the total heat release rate.

The adiabatic wall heat transfer model can also be applied to predict the transient heat transfer to the ceiling. Veldman conducted transient experiments in the impinging plume configuration where fixed source strength resulted in ceiling temperature rise. Comparison of the model predictions and Veldman's experiments are provided in Fig. 4.9. The fire strength of Veldman's Test 1 is $\dot{Q} = 1.17$ kW and the distance between the burner and ceiling is 813 mm. In Veldman's measurements, the flame height of the burner is very small (i.e. $H_f \sim 6$ mm) and thermal radiation is negligible. The virtual origin of this experimental condition is $z_0 = -110$ mm, which

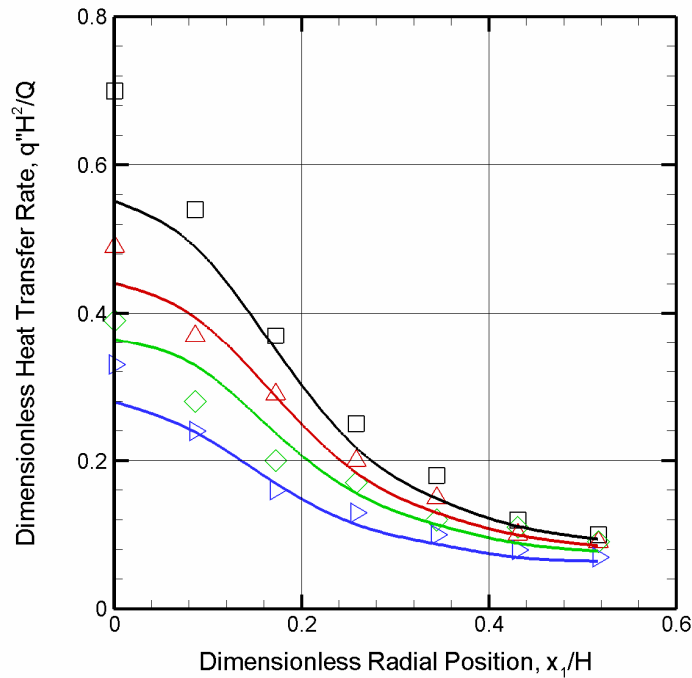


Figure 4.9: Heat transfer rate along ceiling radial position between model and Veldman's Test 1, $Q = 1.17$ kW, $H_c = 0.813$ m; \square $t = 1$ min; \triangle $t = 2$ min; \diamond $t = 3$ min; \triangleright $t = 5$ min [10]. — Author's model predictions sorted with color

was extracted from his plume centerline temperature measurements using Heskestad's method [10]. Good agreement has been achieved between the model and experiments at all locations and times, except at the stagnation point where the model underestimates the heat transfer rate. These discrepancies are caused by the inconsistency of stagnation point temperature T_P between the measurements and the model predictions although the effectiveness, η , has the same distribution. In the current model, T_P is assumed to be the value at $0.85H$ in the unconfined plume configuration which is smaller compared to Veldman's measurement. More salt-water data and fire data will improve estimation of T_P . However, good agreement in the ceiling jet region indicates that the influence of T_P is less important because of the relatively small effectiveness, η , in this region.

Figure 4.10 compares heat transfer models with You's experimental data obtained with $\dot{Q} = 0.24$ kW and $H_f/H_c = 0.008$. The convective heat source, \dot{Q}_c , is estimated by $\dot{Q}_c = 0.8\dot{Q}$. Cooper's model overpredicts the heat transfer rate in the turning region due to the overpredicted heat transfer coefficient resulting from the use of a correlation based on free impinging jet experimental data. You et al.'s correlation provides the correct magnitude of the heat transfer rate at the stagnation point. However, a constant heat transfer rate in the turning region is not in agreement with experimental data. Another limitation of You et al.'s model is that the ceiling temperature is not included in the correlation. Thus it can only be used to predict the heat transfer rate at the initial fire stage when the ceiling temperature is uniform and equals to the ambient temperature. The current heat transfer model based on the

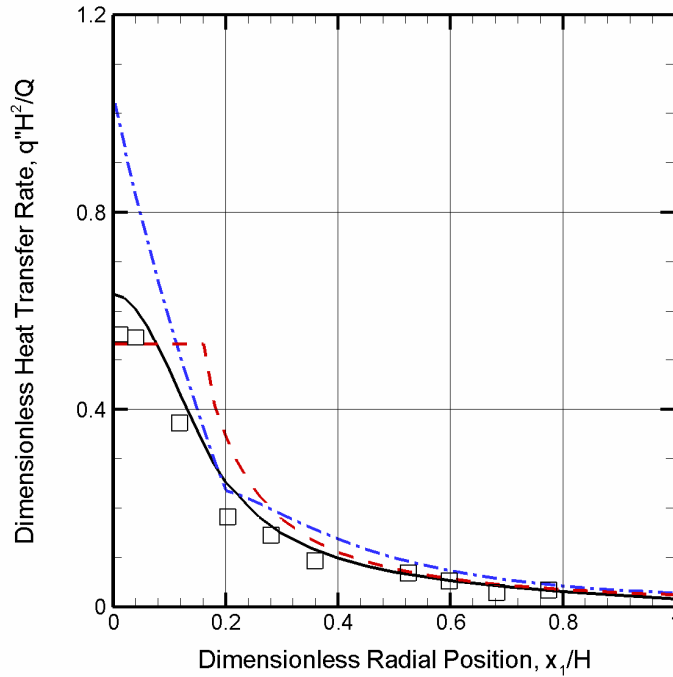


Figure 4.10: Comparison of different heat transfer model with You's experiment \square You's experiment of $Q = 0.24$ kW, $H_f/H_c = 0.08$ [17]; — — You's Correlation; — — — Cooper's model with $Q_c = 0.8Q$ [20]; — Author's model with $Q_c = 0.8Q$;

adiabatic wall concept provides the best agreement with the experimental data. It captures both the magnitude and the decay of the heat transfer rate at the ceiling.

The adiabatic wall heat transfer model in Eq. (4.28) provides a straightforward way to determine the heat transfer rate from the ceiling jet to the ceiling if the ceiling surface temperature is known. Otherwise the ceiling surface temperature can be predicted if the heat transfer rate to the ceiling is known. The equations provided in Eq. (4.28) are well-suited for engineering analysis. For example, assuming the fire strength is 100 kW in a small room fire. The ceiling height of the apartment is 3 m and the room temperature is 300 K before the fire starts. Assuming 30% radiation heat loss and neglecting the virtual origin effect, the peak heat transfer rate at the stagnation point is estimated as 1.9 kW/m². It needs to be noted that current heat

transfer model is only valid for relatively small fire where $H_f/H \ll 1$. The discrepancies between the model predictions and experiments become large when compared with the large fire experiments conducted by Veldman [16] and You [17]. You recommended a different scaling for these fires based on Raleigh number. The author recommends that the model defined in the current study be used for fires having $H_f/H < 0.15$.

Chapter 5: Conclusions

A quantitative salt-water modeling technique was established in this study using the fire/salt-water analogy, dimensionless analysis, and advanced diagnostics. With appropriate non-dimensionalization, the salt-water measurements are directly related to fire induced flows. The quantitative salt-water modeling technique was successfully applied to study the flow characteristics in canonical fire configurations, i.e. the unconfined plume and the impinging plume. Good agreement between salt-water modeling measurements, fire experiments and theoretical predictions demonstrated the ability of using this quantitative salt-water modeling technique to study fire induced flow dynamics. Mixing dynamics in different flow regions in the impinging plume configuration were analyzed through quantitative visualization and analysis of the salt-water flows. Probability density functions (Pdfs) in typical flow regions were also plotted providing insight into the local turbulent mixing behavior. Highly resolved salt-water measurements were also obtained to demonstrate the utility of this technique for development and evaluation of sub-grid scale CFD models. Finally, an adiabatic wall heat transfer model based on Newton's law of cooling and the adiabatic wall-concept was established from quantitative salt-water measurements. The salt-water modeling approach provides a new methodology for establishing engineering level heat transfer models in fires. The following sections summarize and highlight the principal aspects of this investigation and the noteworthy observations and contributions made therein.

Quantitative Salt-Water Model Technique Development

- The fire/salt-water analogy was analyzed and refined with careful dimensionless analysis. A constant coefficient $\beta_{sw} = 0.76$ corresponding to the volumetric expansion was determined in the fire/salt-water analogy analysis based on the dimensionless scale analysis. This quantity had been neglected previously.
- The quantitative salt-water modeling technique was established by implementing PLIF and LDV techniques. Guidance for the injected dye concentrations, camera settings and seeding particles is provided for successful application of the quantitative salt-water modeling technique.
- The fire/salt-water analogy and scaling theory were validated through comparisons between salt-water measurements, fire plume experiments and theoretical data. The turbulent fluctuations of the dimensionless density difference and velocity compared favorably with previous researchers' values further demonstrating the ability of using the salt-water modeling technique to study the flow dynamics of fire induced flows.
- Velocity measurements of plumes were conducted in the current study to add to the limited body of data for this quantity.

Characterization of Impinging Plume Dynamics

- Detailed salt-water measurements provided new insights and improved characterization of the flow mixing dynamics in the plume region, turning region and ceiling jet region.
- The transition point where the flow enters the turning region was established based on the salt-water measurements (i.e. $x_3^+/H = 0.70$). The salt-water flow should be allowed to reach a fully developed turbulent state before entering the turning region in order to simulate a full scale fire. The critical Gr number for

fully developed turbulent flow was determined to be 3.85×10^{10} based on the salt-water measurements. A criterion for the recommended ceiling height for small scale experiment is established based on this critical Gr .

- Flow laminarization was observed along the ceiling surface when $x_1/H > 0.5$, despite a small Ri number (i.e. $Ri = 0.54$). At this location, profound changes were shown in the trends of $\bar{\theta}_{\max}^*$, $(\bar{u}_1)_{\max}^*$ and l_T when the flow is laminarized. However, the boundary layer growth, δ_U , is not significantly affected in the region beyond $x_1/H = 0.5$ as the results of flow transitions from turbulent condition to laminar condition.
- Detailed sub-grid scale turbulent statistic information was provided from highly resolved salt-water measurements. These highly resolved salt-water measurements can serve as an experimental database for development and evaluation of the sub-grid scale model (i.e. β -Pdf) used in LES. Previous researchers have only evaluated the β -Pdf model in non-buoyant flows using a DNS method.

Engineering Heat Transfer Model Development

- An engineering level model was established from the salt-water measurements to predict the heat transfer from the impinging plume to the ceiling. This engineering model is a function of global characteristics of fire configurations (i.e. Re_H , H , r/H , T_w) providing an easy way to predict the heat transfer rate in both constant ceiling temperature and transient ceiling temperature conditions.
- Good agreement between the current model and fire experimental data in the impinging plume configuration validated the modeling methodology. This methodology can now be used to analyze and evaluate the fire and smoke transport dynamics in more complicated geometries.

Future Work:

- Although great effort has been taken to provide highly resolved salt-water measurements for development and validation of LES sub-grid models, the salt-water measurements are still spatial filtered due to the thickness of the laser sheet. A comparison between these filtered salt-water results with DNS simulation will provide a guidance of how well these salt-water measurements resolve the small flow scales.
- Flow laminarization is only qualitatively analyzed in the current study. Scale has to be considered when analyzing the flow laminarization because the position where flow laminarization occurs will change with various source strengths. The location where the laminarization occurs largely depends on the Re_H . More salt-water measurements with different source strengths and impinging plume configurations are useful to establish a general criterion for the flow laminarization location.
- The adiabatic wall heat transfer model compared favorably with fire experimental data in the ceiling jet region. However, discrepancy between the model and fire data is apparent in the turning region. Specifically, the model underestimates the heat transfer rate in the stagnation region. Further salt-water measurements with different ceiling heights and source strengths are useful to verify the prediction of T_P and refine the adiabatic wall heat transfer model. Also more careful fire experimental data are useful for model evaluation.

Appendix A: Source Based Dimensionless Analysis

A1. Source Based Dimensionless Analysis of Fire-Induced Flow

With the Boussinesq assumptions, the governing equations for the fire induced flow are listed in the following

Mass Equation:

$$\rho = \rho_0 \quad (\text{A.1})$$

Momentum Equation:

$$\rho_0 \left(\frac{\partial u_j}{\partial t} + u_i \frac{\partial u_j}{\partial x_i} \right) = - \frac{\partial (p - p_0)}{\partial x_j} + \mu \frac{\partial^2 u_j}{\partial x_i \partial x_i} + (\rho - \rho_0) f_i \quad (\text{A.2})$$

Energy Equation:

$$\rho_o c_p \left(\frac{\partial T}{\partial t} + u_i \frac{\partial T}{\partial x_i} \right) = \lambda \frac{\partial^2 T}{\partial x_i \partial x_i} + \dot{q}''' \quad (\text{A.3})$$

Smoke Mass Species Equation:

$$\rho_o \left(\frac{\partial Y_{smoke}}{\partial t_{fire}} + u_i \frac{\partial Y_{smoke}}{\partial x_i} \right) = \rho_o D \frac{\partial^2 Y_{smoke}}{\partial x_i \partial x_i} + \dot{w}_{smoke} \quad (\text{A.4})$$

Scaling parameters are defined to create non-dimensional equations. The non-dimensional equations reveal important dimensionless parameters that govern the smoke dispersion. Define dimensionless variables as follows

$$\hat{t} = \frac{t_{fire}}{\tau_o}, \quad x_i^* = \frac{x_i}{L_f}, \quad \hat{u}_j = \frac{u_j}{U_o}, \quad \hat{p} = \frac{p - p_a}{p_o}, \quad \hat{\theta} = \frac{(\rho - \rho_o) / \rho_o}{(\rho_{source} - \rho_o) / \rho_o}, \quad f_j^* = \frac{f_j}{g},$$

$$\dot{q}^* = \delta^3 [x_i^* - (x_i^*)_{source}], \quad \theta_T^* = \frac{\beta_T (T - T_o)}{(Q^*)^{2/3}}, \quad w_{smoke}^* = \frac{\dot{w}_{smoke} L_f^3}{\dot{m}_{smoke}}$$

where $f_1^* = 0$, $f_2^* = 0$, $f_3^* = -1$,. Substitution of these scales results in

Momentum Equation:

$$\frac{L_f}{U_o \tau_o} \frac{\partial \hat{u}_j}{\partial \hat{t}} + \hat{u}_i \frac{\partial \hat{u}_j}{\partial x_i^*} = -\frac{p_o}{\rho_o U_o^2} \frac{\partial \hat{p}}{\partial x_i^*} + \frac{\mu}{\rho_o U_o L_f} \frac{\partial^2 \hat{u}_j}{\partial x_i^* \partial x_i^*} + \frac{(\rho_{source} - \rho_o) g L_f}{\rho_o U_o^2} \hat{\theta} \cdot f_j^* \quad (A.5)$$

Energy Equation:

$$\frac{L_f}{U_o \tau_o} \frac{\partial \theta_T^*}{\partial \hat{t}} + \hat{u}_i \frac{\partial \theta_T^*}{\partial x_i^*} = \frac{\lambda}{\rho c_p U_o L_f} \frac{\partial^2 \theta_T^*}{\partial x_i^* \partial x_i^*} + \frac{\beta_T Q}{\rho c_p U_o (Q^*)^{2/3} L_f^3} q^* \quad (A.6)$$

Smoke Mass Species Equation:

$$\frac{L_f}{U_o \tau_o} \frac{\partial Y_{smoke}}{\partial \hat{t}} + \hat{u}_i \frac{\partial Y_{smoke}}{\partial x_i^*} = \frac{D}{U_o L_f} \frac{\partial^2 Y_{smoke}}{\partial x_i^* \partial x_i^*} + \frac{\dot{m}_{smoke}}{U_o \rho_o L_f^2} w_{smoke}^* \quad (A.7)$$

Assume the characteristic development time or transient is based on the flow time

$$\frac{L_f}{\tau_o U_o} = 1 \quad (A.8)$$

and the characteristic pressure is based on the flow pressure,

$$\frac{p_o}{\rho_o U_o^2} = 1 \quad (A.9)$$

Also recognizing that

$$\dot{m}_{smoke} = \dot{m}_{source} (Y_{smoke})_{source} = \frac{Q(Y_{smoke})_{source}}{\Delta H_c} \quad (A.10)$$

where $(Y_{smoke})_{source}$ is the smoke mass fraction generated from the fire source.

Rewriting Eq. (A.5) to Eq. (A.7) results in

$$\frac{\partial \hat{u}_j}{\partial \hat{t}} + \hat{u}_i \frac{\partial \hat{u}_j}{\partial x_i^*} = -\frac{\partial \hat{p}}{\partial x_i^*} + \frac{\nu}{U_o L_f} \frac{\partial^2 \hat{u}_j}{\partial x_i^* \partial x_i^*} + \frac{(\rho_{source} - \rho_o) g L_f}{\rho_o U_o^2} \hat{\theta} \cdot f_j^* \quad (A.11)$$

$$\frac{\partial \theta_T^*}{\partial \hat{t}} + \hat{u}_i \frac{\partial \theta_T^*}{\partial x_i^*} = \frac{\nu}{U_o L_f} \frac{\alpha}{\nu} \frac{\partial^2 \theta_T^*}{\partial x_i^* \partial x_i^*} + \beta_T \frac{Q}{\rho_o c_p (Q^*)^{2/3} U_o L_f^2} q^* \quad (A.12)$$

$$\frac{\partial Y_{smoke}}{\partial \hat{t}} + \hat{u}_i \frac{\partial Y_{smoke}}{\partial x_i^*} = \frac{D}{U_o L_f} \frac{\partial^2 Y_{smoke}}{\partial x_i^* \partial x_i^*} + \frac{Q(Y_{smoke})_{source}}{\rho_o U_o L_f^2 \Delta H_c} w_{smoke}^* \quad (A.13)$$

Considering the convective and buoyancy balance in the momentum equation (A.2),

The scale for U_o can be expressed in term of the density deficit, $|\rho_{source} - \rho_o|/\rho_o$ in

Eq. (A.14)

$$U_o \sim \left(\frac{|\rho_{source} - \rho_o|}{\rho_o} \right)^{1/2} (gL)^{1/2}. \quad (A.14)$$

An alternative scale for U_o can be developed from the source strength

$$Q \sim \dot{m}_{source} c_p (T_{source} - T_o) \quad (A.15)$$

where \dot{m}_{source} is a characteristic mass flux from the fire plume source and T_{source} is a

characteristic temperature of the fire plume source. A scale for the characteristic

mass flux can be determined by recognizing

$$\dot{m}_{source} \sim \rho_o U_o L_f^2 \sim \rho_o U_o L_f^2 \quad (A.16)$$

A new expression for the characteristic velocity scale based on the source strength is

established by substituting Eq. (A.16) into Eq. (A.15),

$$U_o \sim \left(\frac{Q}{\rho_o c_p T_o L_f^2} \right) \left(\frac{(T_{source} - T_o)}{T_o} \right)^{-1} \quad (A.17)$$

For a Boussinesq flow, the density changes are small and a Taylor series expansion

can accurately describe the density. The density can be expressed as

$$\rho = \rho_o + \left. \frac{\partial \rho}{\partial T} \right|_{p,o} (T - T_o) + o(\Delta T^2) \quad (A.18)$$

Furthermore, the fire-induced flow is assumed to behave like an ideal gas so that there is

$$\left. \frac{\partial \rho}{\partial T} \right|_{p,o} = -\rho_o \beta_T = \frac{-p_o}{RT_o^2} = \frac{-\rho_o}{T_o} \quad (\text{A.19})$$

Substitution of Eq. (A.19) into Eq. (A.18) and disregarding the high order error result in

$$\rho = \rho_o - \rho_o \frac{T - T_o}{T_o} \quad (\text{A.20})$$

Or

$$\frac{\rho - \rho_o}{\rho_o} = -\frac{T - T_o}{T_o} \quad (\text{A.21})$$

Substitution of Eq. (A.21) into Eq. (A.17) yields another expression of characteristic velocity scale expressed as,

$$U_o \sim \left(\frac{Q}{\rho_o c_p T_o L_f^2} \right) \left(-\frac{(\rho_{source} - \rho_o)}{\rho_o} \right)^{-1} \quad (\text{A.22})$$

Combining Eq. (A.22) and Eq. (A.14) results in a source based density deficit given by

$$\frac{|\rho_{source} - \rho_o|}{\rho_o} \sim (Q^*)^{2/3} \quad (\text{A.23})$$

where $Q^* = \left(\frac{Q}{\rho_o c_p T_o g^{1/2} L_f^{5/2}} \right)$. Substitution of Eq. (A.23) into Eq. (A.14) results

in a scale for U_o in terms of the source given by

$$U_o \sim (Q^*)^{1/3} (gL_f)^{1/2} \quad (\text{A.24})$$

Combing Eq. (A.24) with Eq. (A.8) and Eq. (A.9) yields a source based time scale

$$\tau_o \sim (Q^*)^{-1/3} (g/L_f)^{-1/2} \quad (\text{A.25})$$

and a source based characteristic pressure,

$$p_o \sim \rho_o g L_f (Q^*)^{2/3} \quad (\text{A.26})$$

Substitution of the source based scales from Eq. (A.23) to (A.26) into the dimensionless control equations of fire induced flow (Eq. (A.11) to (A.13)) gives

$$\frac{\partial u_j^*}{\partial t^*} + u_i^* \frac{\partial u_j^*}{\partial x_i^*} = -\frac{\partial p^*}{\partial x_i^*} + \frac{1}{(Gr_{source}^{fire})^{1/3}} \frac{\partial^2 u_j^*}{\partial x_i^* \partial x_i^*} + \theta_T^* \cdot f_j^* \quad (\text{A.27})$$

$$\frac{\partial \theta_T^*}{\partial t_{fire}^*} + u_i^* \frac{\partial \theta_T^*}{\partial x_i^*} = \frac{1}{(Gr_{source}^{fire})^{1/3} Pr} \frac{\partial^2 \theta_T^*}{\partial x_i^* \partial x_i^*} + \dot{q}^* \quad (\text{A.28})$$

$$\frac{\partial \theta_{smoke}^*}{\partial t^*} + u_i^* \frac{\partial \theta_{smoke}^*}{\partial x_i^*} = \frac{1}{(Gr_{source}^{fire})^{1/3} Sc} \frac{\partial^2 \theta_{smoke}^*}{\partial x_i^* \partial x_i^*} + w_{smoke}^* \quad (\text{A.29})$$

where

$$Gr_{source}^{fire} = \frac{g \dot{Q} L_f^2}{\rho_o c_p T_o v^3}, \quad Pr = \frac{v}{\alpha}, \quad Sc = \frac{v}{D}$$

And the scaled variables in terms of the source terms are

$$t_{fire}^* = t_{fire} (g/L_f)^{1/2} (Q^*)^{1/3}, \quad u_j^* = \frac{u_j}{(Q^*)^{1/3} (g L_f)^{1/2}}, \quad \theta_T^* = \frac{\beta_T (T - T_o)}{(Q^*)^{2/3}},$$

$$\theta_{smoke}^* = \frac{\beta_T Y_{smoke} \Delta H_c}{(Y_{smoke})_o c_p (Q^*)^{2/3}}, \quad p^* = \frac{p}{(Q^*)^{2/3} \rho_o g L_f}, \quad Q^* = \left(\frac{\beta_T \dot{Q}}{\rho_o c_p T_o g^{1/2} L_f^{5/2}} \right)$$

where $\beta_T = \frac{1}{T_o}$.

A2. Source Based Dimensionless Analysis of Salt Water Flow

With the Boussinesq assumptions, the governing equations for the salt water flow are listed as following

Mass Equation:

$$\rho = \rho_o \quad (\text{A.30})$$

Momentum Equation:

$$\rho_o \left(\frac{\partial u_j}{\partial t} + u_i \frac{\partial u_j}{\partial x_i} \right) = - \frac{\partial (p - p_o)}{\partial x_j} + \mu \frac{\partial^2 u_j}{\partial x_i \partial x_i} + (\rho - \rho_o) f_j, \quad (\text{A.31})$$

Salt Mass Species Equation:

$$\rho_o \left(\frac{\partial Y_{salt}}{\partial t} + u_i \frac{\partial Y_{salt}}{\partial x_i} \right) = \rho_o D \frac{\partial^2 Y_{salt}}{\partial x_i \partial x_i} + \dot{w}_{salt} \quad (\text{A.32})$$

where $f_1 = 0$, $f_2 = -g$, $f_3 = 0$. Define dimensionless variables as follows

$$\hat{t} = \frac{t}{\tau_o}, \quad x_j^* = \frac{x_j}{L_{sw}}, \quad \hat{u}_j = \frac{u_j}{U_o}, \quad \hat{p} = \frac{p - p_o}{p_o}, \quad w_{sw}^* = \delta^3 [x_i^* - (x_i^*)_{source}]$$

$$\hat{\theta} = \frac{(\rho - \rho_o) / \rho_o}{(\rho_{source} - \rho_o) / \rho_o}, \quad f_j^* = \frac{f_j}{g}$$

where $f_1^* = 0$, $f_2^* = 0$, $f_3^* = -1$. Substitution of these scales results in

Momentum Equation:

$$\frac{L_{sw}}{U_o \tau_o} \frac{\partial \hat{u}_j}{\partial \hat{t}} + \hat{u}_i \frac{\partial \hat{u}_j}{\partial x_i^*} = - \frac{p_o}{\rho_o U_o^2} \frac{\partial \hat{p}}{\partial x_j^*} + \frac{\nu}{U_o L_{sw}^2} \frac{\partial^2 \hat{u}_j}{\partial x_i^* \partial x_i^*} + \frac{(\rho_{source} - \rho_o) g L_{sw}}{\rho_o U_o^2} \hat{\theta} \cdot f_j^* \quad (\text{A.33})$$

Salt Mass Species Equation:

$$\frac{L_{sw}}{U_o \tau_o} \frac{\partial Y_{salt}}{\partial \hat{t}} + \hat{u}_i \frac{\partial Y_{salt}}{\partial x_i^*} = \frac{D}{U_o L_{sw}} \frac{\partial^2 Y_{salt}}{\partial x_i^* \partial x_i^*} + \frac{\dot{m}_{salt}}{\rho_o U_o L_{sw}^2} \dot{w}_{sw}^* \quad (\text{A.34})$$

Assume the characteristic development time or transient is based on the flow time

$$\frac{L_f}{\tau_o U_o} = 1 \quad (\text{A.35})$$

and the characteristic pressure is based on the flow pressure,

$$\frac{P_o}{\rho_o U_o^2} = 1 \quad (\text{A.36})$$

Equation (A.33) and (A.34) is simplified as

$$\frac{\partial \hat{u}_j}{\partial \hat{t}} + \hat{u}_i \frac{\partial \hat{u}_j}{\partial x_i^*} = -\frac{\partial \hat{p}}{\partial x_j^*} + \frac{v}{U_o L_{sw}} \frac{\partial^2 \hat{u}_j}{\partial x_i^* \partial x_i^*} + \frac{(\rho_{source} - \rho_o) g L_{sw}}{\rho U_o^2} \hat{\theta} \cdot f_j^* \quad (\text{A.37})$$

$$\frac{\partial Y_{salt}}{\partial \hat{t}} + \hat{u}_i \frac{\partial Y_{salt}}{\partial x_i^*} = \frac{D}{U_o L_{sw}} \frac{\partial^2 Y_{salt}}{\partial x_i^* \partial x_i^*} + \frac{\dot{m}_{salt}}{\rho_o U_o L_{sw}^2} \dot{w}_{sw}^* \quad (\text{A.38})$$

A source-based scale for U_o and other quantities of interest are also developed for the salt-water flow just as for the fire flow. For salt-water flows,

$$\dot{m}_{salt} \sim \rho_o (Y_{salt})_{source} U_o L_{sw}^2. \quad (\text{A.39})$$

Rearranging Eq. (A.39) results in the new velocity scale based on the mass flux strength,

$$U_o \sim \frac{\dot{m}_{salt}}{\rho_o L_{sw}^2} \frac{1}{(Y_{salt})_{source}}. \quad (\text{A.40})$$

Taylor series expansion provides the relationship between the salt water density and the salt mass fraction changes. The express is

$$\rho = \rho_o + \left. \frac{\partial \rho}{\partial Y} \right|_o (Y_{salt}) + \mathcal{O}(Y_{salt}^2) \quad (\text{A.41})$$

Similar to the fire case, a density coefficient, β_{sw} , is defined as

$$\beta_{sw} = \left. \frac{1}{\rho_o} \frac{\partial \rho}{\partial Y} \right|_o. \quad (\text{A.42})$$

Substitution Eq. (A.42) into Eq. (A.41) and disregarding the high order error results in

$$\rho = \rho_o + \rho_o \beta_{sw} Y_{salt} \quad (A.43)$$

Thus the injected salt mass fraction, $(Y_{salt})_{source}$, is

$$(Y_{salt})_{source} = \frac{1}{\beta_{sw}} \frac{\rho_{source} - \rho_o}{\rho_o} \quad (A.44)$$

For the salt-water flow, an empirical expression for the density of salt-water as a function of the salt mass fraction has been established as [28]

$$\rho = \rho_o + 0.76 \rho_o Y_{salt} \quad (A.45)$$

which provides $\beta_{sw}=0.76$. Substitution of Eq. (A.44) into Eq. (A.40) results in

$$U_o \sim \left(\frac{\dot{m}_{salt}}{\rho_o L_{sw}^2} \right) \left(\frac{1}{\beta_{sw}} \right)^{-1} \left(\frac{\rho_{source} - \rho_o}{\rho_o} \right)^{-1} \quad (A.46)$$

Combining Eq. (A.46) and Eq. (A.14) results in a source based density deficit given by

$$\frac{\rho_{source} - \rho_o}{\rho_o} \sim (\dot{m}_{sw}^*)^{2/3} \quad (A.47)$$

where $\dot{m}_{sw}^* = \frac{\beta_{sw} \dot{m}_{salt}}{\rho_o g^{1/2} L_{sw}^{5/2}}$. Substitution of Eq. (A.47) into Eq. (A.14) results in a scale

for U_o in terms of the source given by

$$U_o \sim (\dot{m}_{sw}^*)^{1/3} (gL_{sw})^{1/2} \quad (A.48)$$

Similar to the fire induced flow, the a source base time scale is established as

$$\tau_o \sim (\dot{m}_{sw}^*)^{-1/3} (g/L_f)^{-1/2} \quad (A.49)$$

and a source based pressure scale is,

$$p_o \sim \rho_o g L_f (m_{sw}^*)^{2/3} \quad (\text{A.50})$$

Substitution of the source based scales from Eq. (A.47) to (A.50) into the dimensionless control equations of salt water flow (Eq. (A.37) to (A.38)) gives

$$\frac{\partial u_j^*}{\partial t^*} + u_i^* \frac{\partial u_j^*}{\partial x_i^*} = -\frac{\partial p^*}{\partial x_i^*} + \frac{1}{(Gr_{source}^{sw})^{1/3}} \frac{\partial^2 u_j^*}{\partial x_i^* \partial x_i^*} + \theta_{sw}^* \cdot f_j^*, \quad (\text{A.51})$$

$$\frac{\partial \theta_{sw}^*}{\partial \hat{t}^*} + u_i^* \frac{\partial \theta_{sw}^*}{\partial x_i^*} = \frac{1}{(Gr_{source}^{sw})^{1/3} Sc} \frac{\partial^2 \theta_{sw}^*}{\partial x_i^* \partial x_i^*} + \dot{w}_{sw}^* \quad (\text{A.52})$$

where

$$Gr_{source}^{sw} = \frac{\beta_{sw} \dot{m}_{salt} g L_{sw}^2}{\rho_o \nu^3}, \quad Sc = \nu / D$$

And the scaled variables in terms of the source terms are

$$t_{sw}^* = \frac{t_{sw}}{(\dot{m}_{sw}^*)^{-1/3} (g / L_{sw})^{-1/2}}, \quad u_j^* = \frac{u_j}{(g L_{sw})^{1/2} (\dot{m}_{sw}^*)^{1/3}}, \quad \theta_{sw}^* = \frac{\beta_{sw} Y_{salt}}{(\dot{m}_{sw}^*)^{2/3}},$$

$$p^* = \frac{p}{(m_{sw}^*)^{2/3} \rho_o g L_{sw}}, \quad \dot{m}_{sw}^* = \frac{\beta_{sw} \dot{m}_{salt}}{\rho_o g^{1/2} L_{sw}^{5/2}}$$

where $\beta_{sw} = 0.76$.

Appendix B: Laser Sheet Intensity Correction

Since the light sheet produced from the Argon/Ion laser has Gaussian intensity profile, the light emitted by the excited dye is not only a function of the dye concentration, but also a function of the intensity of the incident laser sheet, as shown in Eq. (B-1)

$$GL_{BN}[x_1, x_3] = a_0 I_c[x_1, x_3] C_{dye}[x_1, x_3], \quad (B.1)$$

where $GL_{BN}[x_1, x_3]$ corresponds to a processed image corrected for background noise as described in §2.3.2, a_0 is a constant coefficient, $I_c[x_1, x_3]$ is a distribution corresponding to the laser sheet intensity having a maximum value of one, $C_{dye}[x_1, x_3]$ is distribution corresponding to the mass concentration of the dye. The normalized grey level, GL , can be expressed as

$$GL[x_1, x_3] = \frac{GL_{BN}[x_1, x_3]}{I_c[x_1, x_3]} = a_0 C_{dye}[x_1, x_3], \quad (B.2)$$

In this study, the laser sheet passes through a uniform concentration field to serve as the calibration image which is used to correct the light intensity distribution. The expression of the constant coefficient, a_0 , is given by

$$a_0 \sim \frac{(GL)_{cal}}{(C_{dye})_{cal}}, \quad (B.3)$$

where $(GL)_{cal}$ is the normalized fluorescent light intensity of the calibration image, $(C_{dye})_{cal}$ is the dye concentration of the uniform concentration field in the calibration image.

Generally, a series of 500 instant images of a uniform concentration field are averaged to provide a quantitative measurement of the light intensity distribution. The measured instantaneous flow field images are normalized by the calibration image to correct the concentration field data for the laser sheet intensity distribution effect. In order to reduce the experiments uncertainty, three calibration images have been measured in this research with three different dye concentrations. The constant a_0 used in this study is coming from the linear curve fit from these three measurements.

Appendix C: LES Mixing Model

Computational fluid dynamics is becoming increasingly popular for analyzing fire dynamics and designing fire protection systems. The accuracy of CFD predictions of fire phenomena ranging from combustion reactions to smoke dispersion depends largely on the fidelity of the turbulent mixing models in these codes. The large scale of fires often makes it difficult to resolve the flow details. These flow details are estimated using sub-grid models.

A high fidelity mixing model is essential for accurate prediction of fire behavior, because the combustion in fires is governed primarily by the turbulent fuel-air mixing process. A classical approach in combustion modeling is to describe non-premixed flames in terms of a mixing-controlled, mixture-fraction-based, equilibrium-chemistry model [66-71]

$$\bar{q} = -\left(\frac{Y_F^\infty}{1-Z_{st}}\right)\left(\frac{1}{2}\bar{\rho}\tilde{\chi}\right)\tilde{p}(Z_{st})\Delta H_f \quad (\text{C.1})$$

where \bar{q} is the mean volumetric heat release rate; Y_F^∞ the fuel mass fraction in the fuel supply stream; Z_{st} the stoichiometric value of mixture fraction Z ; $\bar{\rho}$ is the mean mass density; $\tilde{\chi}$ the mean scalar dissipation rate; $\tilde{p}(Z)$ the probability density function for fluctuations in Z ; $\tilde{p}(Z_{st})$ its stoichiometric value; and ΔH_f the heat of combustion per unit mass of fuel.

In Eq. (C.1), $\tilde{\chi}$ gives a measure of the mean rate of fuel-air mixing and $\tilde{p}(Z_{st})$ gives a measure of the probability achieving a stoichiometric fuel/air mixing corresponding to the flame location. A simple closure expression for $\tilde{\chi}$ is [72]

$$\tilde{\chi} = 2D_t |\nabla \tilde{Z}|^2 \quad (\text{C.2})$$

where \tilde{Z} is the mean mixture fraction; and D_t a turbulent mass diffusivity (taken proportional to the turbulent viscosity). Furthermore, $\tilde{p}(Z_{st})$ in Eq. (C.1) may be obtained from a presumed Beta-probability density function (β -Pdf) model where the shape of $\tilde{p}(Z)$ is prescribed as [18-22]

$$\tilde{p}(Z) = \frac{Z^{a-1}(1-Z)^{b-1}}{\left(\int_0^1 Z^{a-1}(1-Z)^{b-1} dZ \right)} \quad (\text{C.3})$$

and where a and b are model coefficients that are parameterized in terms of the mean value \tilde{Z} and the Z -standard deviation σ_Z , defined as

$$a = \tilde{Z} \left\{ \frac{\tilde{Z}(1-\tilde{Z})}{(\sigma_Z)^2} - 1 \right\}; \quad b = (1-\tilde{Z}) \left\{ \frac{\tilde{Z}(1-\tilde{Z})}{(\sigma_Z)^2} - 1 \right\}$$

In a large-eddy simulation (LES) framework, \tilde{Z} is the LES grid-resolved mixture fraction; $\tilde{p}(Z)$ represents the statistical subgrid-scale variations of \tilde{Z} at a given location and time; and σ_Z is the standard deviation of these subgrid-scale fluctuations. σ_Z may be obtained from an algebraic model expression [72] given by

$$(\sigma_Z)^2 = C_Z \Delta^2 |\nabla \tilde{Z}|^2 \quad (\text{C.4})$$

C_Z is a model coefficient that may be expressed in terms of the Smagorinsky constant; and Δ is the LES filter size usually taken as the local grid size. The salt-water experiment provides spatially and temporally resolved information on turbulent mixing and is used in the following as a benchmark configuration to evaluate the (β -Pdf) model in Eq. (C.3) and Eq. (C.4).

Bibliography

1. Belyer, C.L., *Fire Plumes and Ceiling Jets*. Fire Safety Journal, 1986. **11**: p. 53-57.
2. Shabbire, A., George, W.K., *Experiments On a Round Turbulent Buoyant Plume*. J. Fluid Mech., 1994. **275**: p. 1-32.
3. Jankiewicz, S.P., *Prediction Smoke Detector Response Using A Quantitative Salt-water Modeling Technique*, in *Fire Protection Engineering Department*. 2003, University of Maryland: College Park.
4. Steckler, K., Baum, H., and Quintiere, J., *Salt-water Modeling of Fire Induced Flows in Multi-compartment Enclosures*. Twenty-first Symposium (International) on Combustion, 1986: p. 143-149.
5. Kelly, A.A., *Examination of Smoke Movement in a Two-Story Compartment Using Salt Water and Computational Fluid Dynamics Modeling*, in *Fire Protection Engineering Department*. 2001, University of Maryland: College Park.
6. Clement, J.M., and Fleischman, C.M., *Experimental Verification of the Fire Dynamics Simulator Hydrodynamic Model*. Fire Safety Science - Proceedings of the Seven International Symposium, 2002: p. 839-851.
7. Yao, X., Ma, T., Marshall, A.W. and Trouve, A. *Mixing and Turbulent Transport in Unconfined and Impinging Plumes*. in *10th International Fire Science and Engineering Conference -InterFlam*. 2004. Edinburgh, Scotland.
8. Morton, B.R., Taylor, G.I. and Turner, J.S., *Turbulent Gravitational Correction From Maintained and Instantaneous Sources*. Proc. R. Soc. Lond. A, 1956. **234**(1-23).
9. Zukoski, E.E., Kubota, T. and Cetegen, B., *Entrainment in Fire Plumes*. Fire Safety Journal, 1980/1981. **3**: p. 107-121.
10. Heskestad, G., *Virtual Origins of Fire Plumes*. Fire Safety Journal, 1983. **5**: p. 109-114.
11. Yokoi, S., *Upward Convection Current From a Burning Wooden House. the Use of Models in Fire Research*. Publication No. 786. National Academy of Science, 1961.
12. Alpert, R.L., *Turbulent Ceiling-Jet Induced by Large-Scale Fires*. Combustion Science and Technology, 1971. **11**: p. 197-213.

13. McCaffrey, B.J., *Purely Buoyant diffusion Flames: Some Experimental Results*. Center For Fire Research, 1979.
14. Zukoski, Z.Z., *Combustion Fundamentals of Fire*. 1995: Academic Press Ltd.
15. Motevalli, V., and Mark, C., *Characterizing the Unconfined Ceiling Jet Under Steady-State Conditions: A Reassessment*. Fire Safety Science - Proceedings of the Third International Symposium, 1991: p. 301-312.
16. Veldman, C.C., Kubota, T., and Zukoski, E.E., *An Experimental Investigation Of The Heat Transfer From A Buoyant Gas Plume to A Horizontal Ceiling - Part I. Unobstructed Ceiling*. National Institute of Standards and Technology Report NBS-GCR-77-97, 1975.
17. You, H.Z., and Faeth, G.M., *An Investigation of Fire Impingement On a Horizontal Ceiling*. National Institute of Standards and Technology Report NBS-GCR-81-304, 1981.
18. Cooper, L.Y., *Heat Transfer From a Buoyant Plume to an Unconfined Ceiling*. Journal of Heat Transfer, 1982(104): p. 446-451.
19. Cooper, L.Y., *Fire-Plume-Generated Ceiling Jet Characteristics And convective Heat Transfer To Ceiling And Wall Surfaces In a Two-Layer fire Environment: Uniform Temperature Fire Environment: Uniform Temperature Ceiling and Walls*. Fire Science & Technology, 1993. **13**: p. 1-17.
20. Cooper, L.Y., and Woodhouse, A., *The Buoyant Plume-Driven Adiabatic Ceiling Temperature Revised*. Journal of Heat Transfer, 1986. **108**: p. 822-826.
21. Poreh, M., Tsuei, Y.G., and Cermak, J.E., *Investigation of A Turbulent Radia Wall Jet*. ASME Journal of Applied Mechanics, June 1967: p. 457-463.
22. Goldstein, R.J., Sobolik, K. A., Seol, W. S., *Effect of Entrainment on the Heat Transfer to a Heated Circular Air Jet Impinging on a Flat Surface*. Transactions of the ASME, 1990. **112**: p. 608-611.
23. Sangras, R., and Faeth, G.M., *Buoyant Turbulent Jets and Plumes: III. Round turbulent Nonbuoyant Starting Jets and Puffs and Buoyant Starting Plumes and Thermals*. Report No. GDL/GMF-99-03, 1999.
24. Walker, D.A., *A Fluorescence Technique for Measurement of Concentration in Mixing Liquids*. Journal of Physics E: Sci. Instrum., 1987. **20**: p. 217-224.
25. Yao, X., and Marshall, A.W., *Quantitative Salt-water Modeling of Fire Induced Flow*. Fire Safety Journal, submitted, 2005.

26. Yao, X., and Marshall, A.W. *Characterizing of Ceiling Jet Dynamics With Salt-water Modeling*. in *Fire Safety Science - Proceedings of the Eighth International Symposium, IAFSS*. 2005. Beijing, China.
27. Quintiere, J.G., *Scaling Applications in Fire Research*. *Fire Safety Journal*, 1989. **15**: p. 3-29.
28. Wolf, A.V., Brown, M.G. and Prentiss, P.G., *Concentrative Properties of Aqueous Solutions: Conversion Tables*, in *Hand book of Chemistry and Physics, 60th Edition*. 1979-1980. p. D-261-262.
29. Heskestad, G., *Physical Modeling of Fire*. *Fire and Flammability*, 1975. **6**: p. 253-273.
30. Williams, F.A., *Scaling Mass Fires*. *Fire Res. Abstracts and Rev.*, 1969. **11**: p. 1-22.
31. Webster, D.R., Roberts, P.J.W., and Ra'ad, L., *Simultaneous DPTV/PLIF Measurements of Turbulent Jet*. *Experiments in Fluids*, 2001. **30**: p. 65-72.
32. Arcoumanis, C., McGuirk, J.J. and Palma, J.M.L.M., *On The Use Of Fluorescent Dyes For Concentration Measurements in Water Flows*. *Experiments in Fluids*, 1990. **10**: p. 177-180.
33. Houcine, I., Vivier, H., Plasari, E., David, R. and Villermaux, J., *Planar Laser Induced Fluorescence Technique For Measurements of Concentration Fields in Continuous Stirred Tank Reactors*. *Experiments in Fluids*, 1996. **22**: p. 95-102.
34. Guilbault, G.C., *Practical Fluorescence*. 1973: New York: Marcel Dekker.
35. Walker, D.A., *A Fluorescence Technique for Measurement of Concentration in Mixing Liquids*. *Journal of Physics E: Sci Instrum*, 1987. **20**: p. 217-224.
36. *Model 6860 Surepoint Laser Probe & Model 6810 Power Supply Preliminary Draft*, TSI, 1992
37. Durst, F., Melling, A. and Whitelaw, J.H., *Principles And Practice Of Laser-Doppler Anemometry*, ed. Second. 1981, New York: Academic Press. 97-134.
38. List, E.J., *Turbulent Jets and Plumes*. *Ann. Rev. Fluid Mech.*, 1982. **14**: p. 180-212.
39. Dai, Z.T., L.K., and Faeth, G. M., *Structure of Round, Fully Developed, Buoyant Turbulent Plumes*. *Journal of Heat Transfer*, 1994. **116**: p. 409-417.
40. Crowe, C., Sommerfeld, M., and Tsuji, Y., *Multiphase Flows with Droplets and Particles*. 1998, Boca Raton: CRC Press.

41. *Relationship between Salt Solution and Sugar Concentration (Brix) and refractive index at 20°C*, http://www.topac.com/Salinity_brix.html, Topac, 2006.
42. McDougall, T.J., *On the Elimination of Refractive-index Variations in Turbulent Density Stratified Liquid Flows*. J. Fluid Mech., 1979. **93**: p. 83.
43. Barrett, T.K., and Van Atta, C. W., *Experiments On the Inhibition of Mixing in Stably Stratified Decaying Turbulence Using Laser Doppler Anemometry and Laser-Induced Fluorescence*. Phys. Rev. Lett., 1991. **62**: p. 749.
44. Taylor, J.R., *Introduction to Error Analysis: The study of Uncertainties in Physical Measurements*, ed. n. Edition. 1982, Mill Valley: Oxford University Press.
45. Lee, J., and Lee, S.J., *Stagnation Region Heat Transfer Of a Turbulent Axisymmetric Jet Impingement*. Experimental Heat Transfer, 1999. **12**: p. 137-156.
46. Behia, M., Parneix, S. and Durbin, P.A., *Prediction of Heat Transfer In An Axisymmetric Turbulent Jet Impinging On a Flat Plate*. International Journal of Heat Mass Transfer, 1997. **41**: p. 1845-1855.
47. Bejan, A., *Convection Heat Transfer*. 1984, New York: Wiley.
48. Jimenez, J., Linan, A., and Higuera, F. J., *A Priori Testing of Subgrid Models for Chemically Reacting Non-premixed Turbulent Shear Flows*. J. Fluid Mech., 1997. **349**: p. 149-171.
49. Wall, C., Boersma, B.J., and Moin, P., *An Evaluation of the Assumed Beta Probability Density Function Subgrid-Scale Model for Large Eddy Simulation Of Nonpremixed, turbulent Combustion With Heat Release*. Phys. Fluids, 2000. **12**: p. 2522-2529.
50. DesJardin, P.E., and Frankel, S.H., *Large Eddy Simulation Of A Nonpremixed Reacting Jet: Application And Assessment Of Subgrid-scale Combustion Model*. Phys. Fluids, 1998. **10**: p. 2298-2314.
51. Papanicolaou, P.N., and List, E.J., *Large-scale Structure in the Far Field of Bouyant Jets*. J. Fluid Mech., 1989. **209**: p. 151-190.
52. Goldstein, R.J., Sobolik, K. A., and Seol, W. S., *Effect of Entrainment on the Heat Transfer to a Heated Circular Air Jet Impinging on a Flat Surface*. Transactions of the ASME, 1990. **112**: p. 608-611.
53. Incropera, F.P., and Dewitt, D.P., *Fundamentals of Heat And Mass Transfer*, ed. S. Edition. 1985, New York: John wiley & Sons.

54. Glauert, M.B., *J. of Fluid Mechanics*. 1956. **1**: p. 625-643.
55. Kruka, V., and Eskinazi, S., *The Wall-Jet in a Moving Stream*. *J. Fluid Mech.*, 1964. **20**: p. 555-579.
56. Patel, R.P., *Self Preserving Two-Dimensional Turbulent Jets and Wall Jets In a Moving Stream*. 1962, McGill University.
57. Schwarz, W.H., and Cosart, W.P., *The two-dimensional turbulent wall-jet*. *J. Fluid Mech.*, 1961. **10**: p. 481.
58. Laufer, B.E., *The Prandtl-Kolmogorov Model of Turbulence With The Inclusion of Second-order Terms*. *J. Basic Eng.*, 1969. **91**: p. 855-856.
59. Tailland, A., and Mathieu, J., *Jet Parietal*. *Journal de Mecanique*, 1967. **6**: p. 103-131.
60. Phares, D.J., Smedley, G.T., and Flagan, R.C., *The Wall Shear Stress Produced By the Normal Impingement of A Jet On A Flat Surface*. *J. Fluid Mech.*, 2000. **418**: p. 351-375.
61. You, H.Z., and Faeth, G.M., National Institute of Standards and Technology Report NBS-GCR-79-188, 1978.
62. Kays, W.M., and Crawford, M.E., *Convective Heat and Mass Transfer*, ed. Second. 1980: McGraw-Hill Book Company.
63. Donaldson, C.D., Sendeker, R.S., and Margolis, D.P., *A Study Of Free Jet Impingement. Part 2. Free Jet Turbulent Structure and Impingement Heat Transfer*. *J. Fluid Mech.*, 1971. **45**: p. 477-512.
64. Han, B., and Goldstein, R.J., *Jet-Impingement Heat Transfer in Gas Turbine Systems*. *Annals New York Academic Of Sciences*, 2001: p. 147-161.
65. *SFPE Handbook of Fire Protection Engineering*, ed. Second. 1995: National Fire Protection Association. 2-14.
66. Peter, N., *Local Quenching Due to Flame Stretch and Non-premixed Turbulent Combustion*. *Combust. Sci. Technol.*, 1983. **30**: p. 1-17.
67. Willams, F.A., *Combustion Theory*, Second Edition. 1985: Benjamin/Cummings.
68. Moss, J.B., *Turbulent Diffusion Flames in Combustion Fundamentals of Fire* (ed. G. Cox). 1995, Academic Press. p. 221-272.
69. Novozhilov, V., *Computational Fluid Dynamics Modeling of Compartment Fires*. *Prog. Energy Combust. Sci.*, 2001. **27**: p. 611-666.

70. Poinso, T., and Veynante, D., *Theoretical and Numerical Combustion*. 2001: Edwards.
71. Veynante, D., and Vervisch, L., *Turbulent Combustion Modeling*. Prog. Energy Combust. Sci., 2002. **28**: p. 193-266.
72. Pierce, C.D., and Moin, P., *A Dynamic Model for Subgrid-scale variance and Dissipation rate of a Conserved Scalar*. Phys. Fluids, 1998. **10**: p. 3041-3044.